**Title**
Stinging Sensations: Activation Mechanisms of the Wasabi Receptor, TRPA1



**Author**
Lin King, John V.

**Publication Date**
2020

Peer reviewed|Thesis/dissertation

Stinging Sensations: Activation Mechanisms of the Wasabi Receptor, TRPA1

by
John Lin King

DISSERTATION
Submitted in partial satisfaction of the requirements for degree of
DOCTOR OF PHILOSOPHY

in

Neuroscience

in the

GRADUATE DIVISION
of the
UNIVERSITY OF CALIFORNIA, SAN FRANCISCO

Approved:

DocuSigned by:
Lily Jan
394456D87457494...

Lily Jan
Chair

DocuSigned by:
David Julius
DocuSigned by:
Yifan Cheng
DocuSigned by:
Roger Nicoll
44EF5DD68BD1430...

David Julius
Yifan Cheng
Roger Nicoll

Committee Members

**Acknowledgements**

*For Hung—your life has given us life.*

Labmates, I am grateful to each of you for your adventurous, collaborative spirit through the years. In particular, to Josh Emrick, for your enthusiasm, know-how, and can-do attitude; to, Melinda Diver and Wendy Yue, for your tenacious experimentalism and incisive intellect; to Candie Paulsen, for encouraging me to embrace uncertainty; and to Duncan Leitch and Nick Bellono, for your spirited, rigorous approach to inquiry, to which I aspire.

Collaborators—Kati Medzihradszky, Mark Kelly, Volker Herzig, Glenn King, Dan Cohn, and Jianhua Zhao—I recognize you for your utter competence and generosity of time and spirit.

Jeannie, storied lab manager, thank-you for your tireless support and infectious good sense.

Mentors, the genesis of each experiment in this thesis followed directly from your diverse insights, encouragements, and guidance. Lily Jan, thank-you for your thorough and discerning support–you knew exactly which experiments I needed to carry out, a year in advance of my realizing I needed to do so. Roger Nicoll, thank-you for teaching me the inestimable value of a clear-cut, straightforward experiment. Yifan Cheng, thank-you for meeting each experiment with optimism and creativity. And Wei-Jen Tang, thank-you for instilling in me your principled approach to life and science.

Family and Friends, one and all, too many to name here, I acknowledge your love and support throughout the years; without this foundation none of the experiments described here would have been able to be carried out. To my mother, Deidre Shea King, your wisdom, compassion, and intellect inspire me each day.

Finally, David Julius. The highest compliment I think I can give to you is that the only difficult thing about working in your laboratory has been the science—as it should be. Your humility and grace will be guideposts for me throughout my career. Thank-you for pushing me to do hard, necessary experiments. Thank-you for training me in the pursuit of science as joyful and fulfilling.

John Lin King

San Francisco, September 2020

## Contributions

This dissertation reproduces the content of two published manuscripts; their citations and author contributions:

**Chapter 2:**

> Lin King JV, Emrick JJ, Kelly, MJS, Herzig, V, King, GF, Medzihradszky, KF, and Julius D. (2019). A cell-penetrating scorpion toxin enables mode-specific modulation of TRPA1 and pain. *Cell* **178:** 1392-1374

J.V.L.K. and D.J. conceived and designed the project; J.V.L.K. carried out all experiments and analyzed results with collaborative contributions and guidance on behavioral (J.J.E.), NMR (M.J.S.K.), and mass spectrometry (K.F.M.) studies. V.H. and G.F.K. contributed the invertebrate venom library and *U. manicatus* venom. J.V.L.K. and D.J. wrote the paper, with input from all authors.

**Chapter 3:**

> Zhao J*, Lin King JV*, Paulsen CE, Cheng Y, and Julius D. (2020). Irritant-evoked activation and calcium modulation of the TRPA1 receptor. *Nature*. doi.org/10.1038/s41586-020-2480-9

*Denotes equal contribution

J.Z. designed and executed biochemical and cryo-EM experiments, with early collaborative contribution and guidance on TRPA1 expression and purification from C.E.P. J.V.L.K. designed and carried out physiology experiments. J.Z., J.V.L.K, Y.C., and D.J. conceived the project, interpreted the results, and wrote the manuscript.

*"I'm sorry, but I just don't understand anything in biology unless I know what it looks like."*

—Don C. Wiley

**Stinging Sensations: Activation Mechanisms of the Wasabi Receptor, TRPA1**

By John V. Lin King

## Abstract

TRPA1 - also known as the 'wasabi receptor' - is activated by pungent natural products from mustard and allium plants and is responsible for the sinus clearing or eye stinging pain that one experiences when eating horse radish or chopping an onion. More importantly, TRPA1 is a receptor for an astoundingly broad class of volatile environmental irritants and endogenous pro-algesic agents that elicit or exacerbate tissue damage, pain, and neurogenic inflammation. Many of these irritants are chemically reactive electrophiles that activate TRPA1 through a fascinating mechanism involving covalent modification of the channel's cytoplasmic N-terminus, a phenomenon that is not well understood at the biochemical or structural level. TRPA1 also functions as a 'receptor-operated' channel that is activated downstream of phospholipase C signaling pathways, such as those involved in the transduction of pruritic signals. Together, these actions make TRPA1 a major contributor to a broad range of chemo-nociceptive actions include pain and itch.

In this work we have exploited natural product pharmacology, functional recording, and structural methods to understand how TRPA1 is activated by a range of stimuli (reactive and non-reactive, direct and indirect). Collectively, these data draw a detailed mechanistic picture of how this important chemo-nociceptive ion channel detects physiological stimuli, transduces this information into neuronal excitation, and is regulated by cellular events. In light of TRPA1's well recognized role in acute and persistent pain and itch, our findings are of both investigational and therapeutic import. Beyond TRPA1, they are of general relevance to illuminating the gating mechanisms other sensory TRP channels, several of which are also regulated downstream of metabotropic receptors and/or by cellular calcium.

## Table of Contents

## List of Figures

### Chapter 2



### Chapter 3

## List of Tables

### Chapter 2



### Chapter 3

# Chapter 1

# Introduction

## Introduction

### *TRPA1, the Wasabi Receptor*

Piquant natural products (*e.g.,* mustard oil from wasabi), environmental pollutants (*e.g.,* acrolein in exhaust and tear gasses), and endogenous inflammatory mediators (*e.g.,* prostaglandin metabolites, products of tissue injury) produce their familiar stinging sensation through direct activation of a cognate ionotropic receptor TRPA1 (Bautista et al., 2006; Jordt et al., 2004). Indirectly, TRPA1 also serves a 'receptor-operated' channel downstream of metabotropic, phospholipase-C coupled receptors for other classes of algo- and pruritogens (Bandell et al., 2004; Bautista et al., 2006; Jordt et al., 2004). Thus, embedded in the membrane of peripheral afferent sensory neurons, TRPA1 serves an acute protective function as a chemical nociceptor. However, prolonged TRPA1 activation is intimately linked to the establishment and maintenance of chronic pain and inflammation. Understanding, therefore, the molecular mechanisms of TPRA1 activation represents an investigational goal with clear physiological and therapeutic significance (Basbaum et al., 2009; Bautista et al., 2005).

The unifying feature of chemical irritants directly targeting TRPA1, widely disparate in origin and structure, is their electrophilicity Indeed, all activate TRPA1 by a unique mechanism involving covalent modification of nucleophilic residues on the receptor's cytoplasmic face (Bahia et al., 2016; Hinman et al., 2006; Macpherson et al., 2007). Cryo-EM structures of TRPA1 localized these modification sites to an intricately folded intracellular domain termed the 'allosteric nexus', reflecting the idea that it constitutes a key regulatory site for stimulus integration and channel gating(Paulsen et al., 2015; Suo et al., 2020). Despite nearly twenty years of intense investigation, the molecular mechanisms—those principles of the structures and dynamics—that govern direct and indirect TRPA1 activation remain poorly understood.

***Chapter 2***

For example: we wondered, do non-electrophilic TRPA1 activators exist in our environment or endogenously, and if so, do they work through distinct mechanisms to elicit different biophysical or physiologic responses? In chapter 2 we ask if venomous animals produce defensive toxins that target TRPA1(Bohlen and Julius, 2012; Lin King et al., 2019). Several spider toxins have been identified that activate the capsaicin receptor, TRPV1, but algogenic animal toxins targeting TRPA1 have not been described, despite its similarly prominent role in nociception and pain (Bohlen et al., 2010; Siemens et al., 2006). Through blind screening of an invertebrate venom library, we have discovered a potent peptide toxin from the Australian Black Rock scorpion that binds directly and selectively to TRPA1 and stabilizes the channel in its open state. We found that this toxin (which we term Wasabi Receptor Toxin or WaTx) targets the same cytoplasmic allosteric nexus covalently modified by electrophiles. Indeed, through structural, biochemical, and biophysical approaches, we have shown WaTx is a novel cell-penetrating peptide that crosses the plasma membrane to access this key regulatory site.

Collectively, these results provide a striking example of convergent evolution, whereby distantly related life forms (plants and animals) have developed defensive strategies that target the same mammalian receptor at a common regulatory site through completely distinct chemical / pharmacological strategies. These findings confirm the notion that the allosteric nexus is a key control point for TRPA1 gating and thus a compelling target for drug design. Moreover, as a peptide with a known physiologic target, WaTx represents a new tool for studying the enigmatic process of membrane penetration (associated primarily with the HIV transcriptional activator, Tat) and engineering peptides for transmembrane cargo delivery (Guidotti et al., 2017).

In probing the mechanism of WaTx-activation of TRPA1, we encountered a second striking set of findings: at the biophysical level, WaTx enhances TRPA1 function by stabilizing the channel in its open state and thus acts as a gating modifier, rather than a true agonist. Moreover, this toxin-stabilized open state has a substantially lower permeability to calcium ions compared to the electrophile-activated state, which at the physiologic level results in diminished release of inflammatory peptides from toxin-activated sensory neurons. Consequently, WaTx elicits acute pain and pain hypersensitivity, but without accompanying neurogenic inflammation that is characteristic of wasabi-evoked pain. Not only do these findings provide proof-of-principle that mode-specific modulation of TRP channel gating is possible (which is relevant to drug development goals), but also suggests a pharmacological strategy for isolating and probing central mechanisms of pain sensitization by eliminating the peripheral component (Basbaum et al., 2009; Osteen et al., 2016).

***Chapter 3***

The discovery of WaTx and subsequent mapping of its receptor site to the allosteric nexus underscores how this region is a critical control point for TRPA1 gating. Structures of this channel alone and in complex with covalently attached electrophiles occupy a single 'closed' conformation, unable to pass ions (Paulsen et al., 2015; Suo et al., 2020). How, then, does the allosteric directly integrate structurally and functionally diverse ligands and translate the energy of ligand binding into conformational changes that gate the channel? To address this question, in chapter 3 we combine cryo-EM and electrophysiology to show how this channel recognizes structurally diverse electrophiles, and how their covalent attachment promotes channel gating (Zhao et al, 2020). First, we visualize covalent attachment of a reactive electrophile to a highly nucleophilic cysteine within a key allosteric regulatory site of the channel and show how this

attachment promotes a profound conformational transition within this region, exposing a second cysteine residue for covalent modification. This two-step mechanism stabilizes the domain in a configuration that promotes opening of the channel's cytoplasmic gate. We further show that a bulky electrophile can bypass the need for a second modification event, explaining how the channel can accommodate a broad range of structurally diverse electrophilic agonists. Second, we show that in addition to opening the canonical gate at the cytoplasmic end of the ion permeation pathway, electrophile modification also widens the selectivity filter at the extracellular end of the pathway to enhance calcium permeability, which we know is important for channel regulation and release of pro-inflammatory neuropeptides from TRPA1-expressing nociceptors. We offer a structural explanation for this effect, and for how these two control points are functionally coupled to effect dynamic ion selectivity. Finally, we also leverage these approaches to elucidate how TRPA1 function is controlled by calcium or PLC signaling to effect indirect activation of chemo-nociceptive channel (Bautista et al., 2013). Our structural and electrophysiological analyses identify a calcium binding pocket that is remarkably conserved across TRP channel subtypes and which accounts for all aspects of calcium-dependent TRPA1 regulation, including potentiation, desensitization, and activation by PLC-coupled receptors. These results resolve longstanding questions about the locus of calcium action and which PLC-derived second messenger(s) is most important for activating TRPA1 as a receptor-operated channel.Taken together, theses studies elucidate the molecular mechanism by which TPA1 serves as a high-sensitivity, low-threshold detector for electrophilic irritants as well as a receptor-operated channel; they draft a detailed blueprint for future efforts to control this channel for technical, biological, and therapeutic investigations.

**References**

Bahia, P.K., Parks, T.A., Stanford, K.R., Mitchell, D.A., Varma, S., Stevens, S.M., Jr., and Taylor-Clark, T.E. (2016). The exceptionally high reactivity of Cys 621 is critical for electrophilic activation of the sensory nerve ion channel TRPA1. The Journal of general physiology *147*, 451-465.

Bandell, M., Story, G.M., Hwang, S.W., Viswanath, V., Eid, S.R., Petrus, M.J., Earley, T.J., and Patapoutian, A. (2004). Noxious cold ion channel TRPA1 is activated by pungent compounds and bradykinin. Neuron *41*, 849-857.

Basbaum, A.I., Bautista, D.M., Scherrer, G., and Julius, D. (2009). Cellular and molecular mechanisms of pain. Cell *139*, 267-284.

Bautista, D.M., Jordt, S.E., Nikai, T., Tsuruda, P.R., Read, A.J., Poblete, J., Yamoah, E.N., Basbaum, A.I., and Julius, D. (2006). TRPA1 mediates the inflammatory actions of environmental irritants and proalgesic agents. Cell *124*, 1269-1282.

Bautista, D.M., Movahed, P., Hinman, A., Axelsson, H.E., Sterner, O., Hogestatt, E.D., Julius, D., Jordt, S.E., and Zygmunt, P.M. (2005). Pungent products from garlic activate the sensory ion channel TRPA1. Proceedings of the National Academy of Sciences of the United States of America *102*, 12248-12252.

Bautista, D.M., Pellegrino, M., and Tsunozaki, M. (2013). TRPA1: A gatekeeper for inflammation. Annual review of physiology *75*, 181-200.

Bohlen, C.J., and Julius, D. (2012). Receptor-targeting mechanisms of pain-causing toxins: How ow? Toxicon : official journal of the International Society on Toxinology *60*, 254-264.

Bohlen, C.J., Priel, A., Zhou, S., King, D., Siemens, J., and Julius, D. (2010). A bivalent tarantula toxin activates the capsaicin receptor, TRPV1, by targeting the outer pore domain. Cell *141*, 834-845.

Guidotti, G., Brambilla, L., and Rossi, D. (2017). Cell-Penetrating Peptides: From Basic Research to Clinics. Trends in Pharmacological Sciences *38*, 406-424.

Hinman, A., Chuang, H.H., Bautista, D.M., and Julius, D. (2006). TRP channel activation by reversible covalent modification. Proceedings of the National Academy of Sciences of the United States of America *103*, 19564-19568.

Jordt, S.E., Bautista, D.M., Chuang, H.H., McKemy, D.D., Zygmunt, P.M., Hogestatt, E.D., Meng, I.D., and Julius, D. (2004). Mustard oils and cannabinoids excite sensory nerve fibres through the TRP channel ANKTM1. Nature *427*, 260-265.

Lin King, J.V., Emrick, J.J., Kelly, M.J.S., Herzig, V., King, G.F., Medzihradszky, K.F., and Julius, D. (2019). A Cell-Penetrating Scorpion Toxin Enables Mode-Specific Modulation of TRPA1 and Pain. Cell *178*, 1362-1374.e1316.

Macpherson, L.J., Dubin, A.E., Evans, M.J., Marr, F., Schultz, P.G., Cravatt, B.F., and Patapoutian, A. (2007). Noxious compounds activate TRPA1 ion channels through covalent modification of cysteines. Nature *445*, 541-545.

Osteen, J.D., Herzig, V., Gilchrist, J., Emrick, J.J., Zhang, C., Wang, X., Castro, J., Garcia-Caraballo, S., Grundy, L., Rychkov, G.Y.*, et al.* (2016). Selective spider toxins reveal a role for the Nav1.1 channel in mechanical pain. Nature *534*, 494-499.

Paulsen, C.E., Armache, J.P., Gao, Y., Cheng, Y., and Julius, D. (2015). Structure of the TRPA1 ion channel suggests regulatory mechanisms. Nature *520*, 511-517.

Siemens, J., Zhou, S., Piskorowski, R., Nikai, T., Lumpkin, E.A., Basbaum, A.I., King, D., and Julius, D. (2006). Spider toxins activate the capsaicin receptor to produce inflammatory pain. Nature *444*, 208-212.

Suo, Y., Wang, Z., Zubcevic, L., Hsu, A.L., He, Q., Borgnia, M.J., Ji, R.R., and Lee, S.Y. (2020). Structural Insights into Electrophile Irritant Sensing by the Human TRPA1 Channel. Neuron *105*, 882-894.e885.

Zhao J, Lin King JV, Paulsen CE, Cheng Y, and Julius D. (2020). Irritant-evoked activation and calcium modulation of the TRPA1 receptor. *Nature*. doi.org/10.1038/s41586-020-2480-9

# Chapter 2

## A cell-penetrating scorpion toxin enables mode-specific modulation of TRPA1 and pain

**Summary**

TRPA1 is a chemosensory ion channel that functions as a sentinel for structurally diverse electrophilic irritants. Channel activation occurs through an unusual mechanism involving covalent modification of cysteine residues clustered within an amino-terminal cytoplasmic domain. Here we describe a peptidergic scorpion toxin (WaTx) that activates TRPA1 by penetrating the plasma membrane to access the same intracellular site modified by reactive electrophiles. WaTx stabilizes TRPA1 in a biophysically distinct active state characterized by prolonged channel openings and low $Ca^{2+}$ permeability. Consequently, WaTx elicits acute pain and pain hypersensitivity, but fails to trigger efferent release of neuropeptides and neurogenic inflammation typically produced by noxious electrophiles. These findings provide a striking example of convergent evolution whereby chemically disparate animal- and plant-derived irritants target the same key allosteric regulatory site to differentially modulate channel activity. WaTx is a unique pharmacological probe for dissecting TRPA1 function and its contribution to acute and persistent pain.

## Introduction

The TRPA1 ion channel (also known as the wasabi receptor) is expressed by primary afferent sensory neurons, where its activation by piquant natural products from mustard and allium plants elicits the sinus clearing or eye stinging pain one experiences when eating wasabi or chopping an onion (Bandell et al., 2004; Jordt et al., 2004). This reflects TRPA1's role as a chemosensory receptor for a broad class of volatile environmental irritants and endogenous inflammatory agents that directly activate the channel to produce acute and persistent pain. TRPA1 also functions as a 'receptor-operated' channel that is activated downstream of phospholipase C-coupled receptors that detect pruritic and pro-inflammatory agents (Bandell et al., 2004; Bautista et al., 2006). Thus, TRPA1 is considered a promising therapeutic target for treating chronic pain, itch and neurogenic inflammatory syndromes that are initiated or exacerbated by nociceptor activation (Andersson et al., 2008; Bautista et al., 2013; Julius, 2013).

Most TRPA1 agonists, including plant-derived irritants, environmental toxicants, and endogenous products of oxidative stress, are chemically reactive electrophiles (*e.g.* isothiocyanates, thiosulfinates and α, β-unsaturated aldehydes) that work through a unique mechanism involving covalent modification of specific cysteine residues located within the channel's cytoplasmic amino terminus (Bahia et al., 2016; Hinman et al., 2006; Macpherson et al., 2007). A recent cryo-EM structure of TRPA1 localized these modification sites to an intricately folded intracellular domain termed the 'allosteric nexus.' This reflects the idea that this locus constitutes a key regulatory site for stimulus integration that is poised to propagate ligand-evoked conformational changes to the channel's gate (Bahia et al., 2016; Palovcak et al., 2015; Paulsen et al., 2015).

Natural, non-electrophilic TRPA1 agonists have been identified, such as Δ9-tetrahydrocannabinol (THC) and menthol. However, these compounds are of low potency, efficacy, and specificity,

limiting their usefulness as probes for understanding non-covalent mechanisms of TRPA1 activation (Jordt et al., 2004; Karashima et al., 2007). We therefore wondered whether other non-chemically reactive TRPA1 ligands exist and, if so, do their mechanisms of action elicit distinct biophysical, physiologic, and behavioral responses. Identifying such pharmacophores and their mechanisms of action is essential to fully understanding and manipulating TRPA1 function under normal (acute) and pathophysiological (chronic) pain states. Indeed, a critical goal in developing novel analgesics is to modulate the activity of key receptors or channels in the context of chronic pain while sparing their core protective functions – a challenge that has beset development of drugs targeting the heat / capsaicin receptor, TRPV1 (Basbaum et al., 2009; Moran, 2018).

To begin to address this important issue in regard to TRPA1, we turned to animal venoms as evolutionarily honed chemical 'libraries' that contain pain-inducing defensive agents (Bohlen et al., 2011; Bohlen and Julius, 2012; Hille, 2001; Osteen et al., 2016; Siemens et al., 2006; Zhang et al., 2017). While hundreds of peptide toxins are known to target voltage-gated ion channels, few have been identified that act on TRP channels, and these all activate the capsaicin receptor, TRPV1 (Bohlen et al., 2010; Hille, 2001; Kalia et al., 2015; King and Hardy, 2013; Siemens et al., 2006). Despite the similarly prominent role of TRPA1 in nociception and pain, algogenic toxins targeting this member of the TRP channel family have not been described.

Here we identify a potent and selective peptide scorpion toxin that modulates TRPA1 by crossing the plasma membrane and binding to the same allosteric nexus that is covalently modified by electrophilic irritants. In doing so, the toxin stabilizes a unique channel state characterized prolonged open times and low divalent cation permeability, which we exploit to elucidate the contribution of intrinsic TRPA1 calcium permeability to efferent nociceptor function, neurogenic inflammation, and pain hypersensitivity.

## Results

### *Black Rock scorpions produce a TRPA1-activating toxin*

We used ratiometric calcium ($Ca^{2+}$) imaging of rat TRPA1-expressing HEK293T (HEK) cells to screen through a large invertebrate venom library in search of direct channel activators. Because TRPA1 is activated by manipulations that increase intracellular free $Ca^{2+}$ (Jordt et al., 2004; Wang et al., 2008), high throughput screening of crude venoms (which contain a multitude of proteases, lipases, and other hydrolytic activities) can be plagued by false positives (Bohlen and Julius, 2012). We therefore began our search by first depleting venoms of high molecular weight cell-lytic components, and by instituting a counter-screen in which intracellular $Ca^{2+}$ stores were depleted prior to venom addition (Jordt et al., 2004; Osteen et al., 2016; Zhang et al., 2017). In this way, we zeroed in on venom from the Australian Black Rock scorpion (*Urodacus manicatus*, (Thorell, 1876)) as containing a robust TRPA1 activator (Figure 2.1A,B; 2.7A-C). Reversed phase HPLC yielded a single active peptide whose primary amino acid sequence was determined by manual interpretation of high resolution, high mass accuracy collision-induced dissociation mass spectra (Figure 2.1C; 7D, E, G; Table 2.1). The deduced pattern of cysteine residues suggested a 1-4, 2-3 arrangement of disulfide bonds (Figure 2.1C) (Quintero-Hernandez et al., 2013; Tytgat et al., 1999). Indeed, a cognate synthetic peptide with this same arrangement fully recapitulated activity of the native species and was used for all further experiments (Figure 2.7F).

We first asked if this peptide, which we call Wasabi Receptor Toxin (WaTx), constitutes a potent, direct, and selective TRPA1 ligand. Application of WaTx to human TRPA1-transfected HEK cells produced characteristic outwardly rectifying membrane currents that reversed rapidly upon toxin washout when compared with those evoked by the covalent electrophilic agonist, mustard oil (allyl isothiocyanate, AITC) ($\tau_{off}$ = 4.6 ± 1.2 vs. 27 ± 5 seconds for WaTx and AITC, respectively; $p <$

0.05, unpaired two-tailed Student's *t*-test). Toxin-evoked responses were blocked by the TRPA1-selective channel inhibitor, A 967079 (Figure 2.1D-F) (Chen et al., 2011), and did not require extracellular or intracellular $Ca^{2+}$, indicative of direct toxin action on the channel (Figure 2.1D). Furthermore, recordings were carried out in nominally $Ca^{2+}$-free bath solution when intracellular $Ca^{2+}$ was chelated with EGTA, demonstrating that these responses do not require extracellular or intracellular $Ca^{2+}$. These observations are consistent with direct action of the toxin on TRPA1 (Figure 2.1D). WaTx was both potent ($EC_{50}$ = 15, 95% CI 13-18 nM) and selective since application of a saturating dose (5μM) of toxin to trigeminal sensory neurons from wild-type mice excited only the cohort sensitive to a selective dose of AITC (50μM). Furthermore, WaTx had no effect on neurons from TRPA1-deficient animals (Figure 2.1G, H; 2.7H-L). To further test toxin specificity, we asked whether WaTx elicited effects on other heterologously expressed sensory TRP channels or representative members of classical voltage-gated potassium channel subfamilies (Shaker, Shal, Shab, and Shaw). We observed neither inhibition nor enhancement of channel activity when toxin was applied alone (at concentrations saturating for TRPA1) or in combination with a relevant stimulus (Figure 2.7C, M, N).

***Membrane penetration is required for WaTx action***

In contrast to classic TRPA1 agonists, WaTx is a relatively large macromolecule that lacks any obvious electrophilic character. We therefore initiated a series of patch clamp recording experiments to probe its mechanism and site of action. At the outset, we were surprised to observe WaTx-evoked responses in the on-cell patch configuration, prior to rupturing the membrane to achieve whole-cell access (Figure 2.8A). This suggested that WaTx mediates its effect either by generating a cytoplasmic second messenger, or by crossing the membrane to access TRPA1 channels under the patch pipette (Horn, 1991; Lipscombe et al., 1989; Sakmann and Neher, 2009).

To distinguish between these possibilities, we asked whether the toxin elicited responses when applied to membranes excised from the cell in an outside-out or inside-out configuration. Remarkably, activity was observed in either configuration, consistent with a membrane penetrating mechanism of WaTx action (Figure 2.2A, B; 2.8B, C). To test this idea directly, we established a FRET-based assay to quantify translocation of fluorescently tagged WaTx into liposomes loaded with an acceptor fluorophore coupled to IgG. This reductionist, cell-free system allowed us to quantitatively and kinetically assess peptide movement across a lipid bilayer. Indeed, toxin readily crossed the liposome bilayer with a rate-constant linearly related to concentration, reaching equilibrium within minutes (Figure 2.2D, E).

WaTx bears little sequence homology to other known peptides, although its disulfide bonding pattern is reminiscent of a small family of κ-KTx scorpion toxins that form cysteine-stabilized helical hairpins (Cs α/α), or spider and crab toxins that form a cysteine-stabilized antiparallel β-sheet (Cs β/β) (Quintero-Hernandez et al., 2013; Silva et al., 2000; Srinivasan et al., 2002) (Figure 2.1C). Moreover, WaTx bears no obvious sequence similarity to classical cell penetrating peptides (CPPs), such as HIV Tat or *Drosophila* penetratin (Derossi et al., 1994; Frankel and Pabo, 1988; Joliot et al., 1991; Kauffman et al., 2015; Vives et al., 1997). To identify WaTx features that might enable membrane penetration, we determined its atomic structure using solution NMR (Figure 2.8H-K; Table 2.2). We found the toxin adopts a rigid and compact helical hairpin fold stabilized by two disulfide bonds (Figure 2.2C; 2.8K), consistent with its resemblance to κ-KTx scorpion toxins. A patch or preponderance of basic residues has previously been associated with cell-penetrating properties of peptides (Guidotti et al., 2017; Kauffman et al., 2015). In this regard, a notable tertiary structural feature of WaTx is the formation of a basic patch at the open end of the hairpin, where amino- and carboxy-termini meet. Here, the amino-terminal helix exhibits an

unusually dense (4.5σ) dipole moment (Felder et al., 2007). Together, these features may constitute the cell penetrating motif (Figure 2.2F).

To test this hypothesis, we evaluated toxins bearing alanine substitution at four residues (K7, Q4, Q5, and R32) within this basic patch for their ability to activate TRPA1 in cell-attached versus excised inside-out configurations. Of these, only K7A displayed a reduced ability to activate channels in cell-attached mode, even though it was fully functional when applied to excised patches (Figure 2.2G; 2.8D-I). Consistent with these data, we observed ~25% reduction in the rate at which this mutant was able to load liposomes (Figure 2.2E), suggesting that this basic residue is important for facilitating membrane penetration. Altogether, these results support a direct mechanism of peptide penetration *via* passive diffusion (Bechara and Sagan, 2013; Guidotti et al., 2017; Kauffman et al., 2015) and establish that cell penetration and channel activation are distinct biophysical properties of the toxin.

***WaTx targets the intracellular allosteric nexus of TRPA1***

The ability of WaTx to penetrate the membrane does not *a priori* limit its site of action to an intracellular domain, and we therefore set out to identify its site of action using physiological and biochemical assays. TRPA1 orthologues show significant phylogenetic variation (Cordero-Morales et al., 2011; Gracheva et al., 2010; Kang et al., 2010; Kindt et al., 2007; Prober et al., 2008), and we indeed found that mammalian TRPA1 orthologues are activated by WaTx, whereas channels from more distantly related species (such as snakes, fish, flies and worms) are insensitive (Figure 2.3A; 2.9A, B). We leveraged this differential profile to initiate an unbiased, chimeric receptor approach to identify a region of TRPA1 that specifies toxin sensitivity, using human and rat snake TRPA1 (hTRPA1 and rsTRPA1, respectively) as the donor-recipient pair (Figure 2.3A; 2.9B, C, K). Transfer of the C-terminal TRP domain from rat snake to human TRPA1 produced a

channel that was insensitive to WaTx but robustly activated by AITC, implicating this domain as a key element in specifying toxin sensitivity (Figure 2.9C). However, the inverse chimera (rsTRPA1 harboring the human TRP domain) remained toxin insensitive, indicating that this region is necessary, but insufficient to confer WaTx sensitivity (Figure 2.9D). In the three-dimensional structure of TRPA1, the TRP domain engages in extensive interactions with the N-terminal, cysteine-rich linker domain, an interaction that forms the core of the 'allosteric nexus' that is critical for activation by electrophilic agonists. Indeed, we found that transfer of the cysteine-rich linker region from the human to rat snake channel was sufficient to confer toxin sensitivity (Figure 2.9D). Within the cysteine-rich linker, conversion of three amino acids of the human channel (hTPRA1 P622A, M634L, and T646P) to cognate rat snake residues abrogated toxin sensitivity (Figure 2.3B, C; 2.9E-G). Of the converse changes, only the first (rsTRPA1 A627P) was sufficient to confer toxin sensitivity to the rat snake channel, demonstrating that a proline in this position is a key determinant of WaTx species selectivity (Figure 2.3C, D and G; 2.9H, J).

To ask whether the allosteric nexus forms a binding site for the toxin, we established a biolayer interferometry-based assay in which immobilized, biotinylated WaTx was used to capture crude membranes containing TRPA1. In this way we measured WaTx:TRPA1 interaction directly. Robust binding was observed with membranes prepared from hTRPA1- but not rsTRPA1-transfected HEK293 cells (Figure 2.3E, F; 2.9I). Importantly, membranes containing the rsTRPA1 gain-of-function mutant (A627P) did display binding, while those containing the hTPRA1 loss-of-function mutant (P622A) did not, consistent with their electrophysiological profiles (Figure 2.3A-F; 2.9I). From these data, we determined an off-rate constant for WaTx binding to hTRPA1 ($k_{off}$ = 4.28 ± 0.39 × $10^{-4}$ $min^{-1}$) and a conservative estimate of a dissociation constant ($k_{on}$ = 8.80 × $10^{9}$

$\pm$ 0.59 $\times$ $10^9$ $mol^{-1}$ $min^{-1}$; $K_D$ = 0.33 $\pm$ 0.55 pM) (Figure 2.3E). Taken together, these results demonstrate that WaTx binds directly and tightly to TRPA1, likely involving interactions with an integrated complex formed between the N-terminal cysteine-rich linker and C-terminal TRP domains. We propose that this binding site is located at subunit interfaces where the three-dimensional structure shows that these regions are in close apposition and form a potential binding pocket in which the toxin could nestle (Figure 2.3G, H) (Paulsen et al., 2015). In either case, our results show that WaTx acts at the structurally integrated allosteric nexus that also transduces electrophile reactivity to the channel gate.

***WaTx stabilizes a unique channel open state***

If electrophiles and WaTx converge on a single TRPA1 domain to activate the channel, do they work through similar or distinct biophysical mechanisms? Neither agent altered the voltage-dependence of channel activation, although close inspection revealed dramatically different kinetics of toxin- versus electrophile-evoked tail currents, suggesting distinct mechanisms of action (Figure 2.10A-C). Indeed, each agent also had strikingly different effects on single channel behavior. AITC elicited a large increase in open probability characterized by brief ($\leq$ 5 msec) transitions between open and closed states (Figure 2.4A, B; 2.10D). Moreover, AITC application dramatically shortened the average latency to first channel opening, consistent with behavior of a true agonist that directly promotes channel opening (Figure 2.4C; 2.10E). On the other hand, WaTx produced openings that were markedly longer ($\leq$ 20 msec.), and with an average latency to first opening that was indistinguishable from that of basal, spontaneous events (Figure 2.4A-C; 2.10E). Thus, in contrast to AITC, WaTx behaves as a gating modifier that stabilizes, rather than directly promotes the open state.

The differential effects of electrophile and toxin on gating can be further illustrated by the finding that WaTx reversibly modifies constitutively active channels. We demonstrated this by first eliciting channel openings by brief application of the irreversible electrophilic agonist, iodoacetamide (IAM) (Hinman et al., 2006). Following IAM washout, exposure to WaTx reversibly shifted the distribution of open state dwell times rightward ($\tau_{dwell}$ = 1.5 ± < 0.01 and 2.8 ± 0.6 msec. for IAM and WaTx, respectively; $p < 0.0001$, unpaired two-tailed Student's *t*-test) (Figure 2.4D, E). These results reinforce the notion that WaTx specifically modulates the TRPA1 open state and demonstrate that the actions of electrophiles and WaTx are functionally distinct and not mutually exclusive.

While these ligands produce kinetically distinguishable open states, do these states also differ with respect to ion conductance or permeability (Chung et al., 2008; Tominaga et al., 1998)? To address this question, we determined ion permeability sequences of hTRPA1 during spontaneous, AITC- or WaTx-evoked openings. These measurements were carried out with excised membrane patches from hTRPA1-transfected HEK cells to afford complete control over 'extracellular' and 'intracellular' cations, in particular $Ca^{2+}$ (Bobkov et al., 2011; Wang et al., 2008). In excellent agreement with previous reports, TRPA1 displayed notable (~ 8 fold) selectivity for divalent over monovalent cations; was impermeant to the large organic cation NMDG; and, when stimulated with AITC, produced a small but significant increase in divalent cation selectivity (Figure 2.4F, 2.10F, G) (Bobkov et al., 2011; Karashima et al., 2010; Nagata et al., 2005; Story et al., 2003). Surprisingly, however, WaTx largely abolished the channel's preference for divalent over monovalent cations (Figure 2.4F; 2.10F, G), suggesting that it produces a unique open configuration of the ion conduction pathway. In contrast to these differential effects on ion selectivity, neither ligand altered $Ca^{2+}$ conductance, and $Na^{+}$ conductance was potentiated when

$Ca^{2+}$ was present at the channel's cytoplasmic face (Figure 2.4F, 2.10G), as previously described (Wang et al., 2008). These findings, including differential effects of electrophiles versus WaTx on open state kinetics and cation permeability, were also observed with mouse TRPA1 (Figure 2.10H-J). Taken together, our results demonstrate that spontaneous, electrophile- and toxin-evoked open states are kinetically and functionally distinct.

***WaTx produces pain hypersensitivity without inflammation***

AITC and other electrophiles excite TRPA1-positive, peptidergic nociceptors to elicit acute pain and neurogenic inflammation that is accompanied by hypersensitivity to thermal and mechanical stimuli (Basbaum et al., 2009; Bautista et al., 2006; Bautista et al., 2013). In light of the observed biophysical differences between WaTx- and electrophile-mediated TRPA1 activation, we asked whether these agents elicit the same spectrum of algogenic responses.

Like AITC, WaTx injection into the mouse hindpaw produced vigorous, dose-dependent nocifensive (pain-related) behavior that engaged central nociceptive neuronal pathways, as evidenced by induction of c-Fos immunoreactivity in superficial laminae of the spinal cord dorsal horn (Figure 2.5A-C; 2.11A-C). These responses were not observed in TRPA1-deficient mice, demonstrating toxin specificity *in vivo* (Figure 2.5A-C; 2.11B, C).

Intraplantar AITC injection elicited characteristic paw swelling and increased vascular permeability, responses that underlie neurogenic inflammation resulting from TRPA1-evoked vesicular release of pro-inflammatory neuropeptides (Substance P and CGRP). Surprisingly, while WaTx evoked acute pain behavior, it failed to produce these key signatures of neurogenic inflammation (Figure 2.5F, G; 2.11D). Consistent with this differential physiologic response, AITC promoted robust CGRP release from cultured rat trigeminal neurons, while WaTx did not

(Figure 2.5H). This release occurred in the presence of voltage-gated $Ca^{2+}$ channel inhibitors, but not when TRPA1 was blocked or intracellular $Ca^{2+}$ chelated, demonstrating its dependence on $Ca^{2+}$ entry through TRPA1 *per se* (Figure 11K). Thus, we conclude that WaTx fails to promote CGRP release (and thus neurogenic inflammation) because it reduces $Ca^{2+}$ permeability of activated TRPA1 channels compared to electrophiles. Indeed, WaTx was able to promote CGRP release from cultured sensory neurons when the driving force for $Ca^{2+}$entry was increased by raising extracellular $Ca^{2+}$ levels 10-fold (Figure 2.5H). Taken together, these results demonstrate that high intrinsic $Ca^{2+}$ permeability is critical to the role that TRPA1 normally plays in post-injury neurogenic inflammatory responses that ideally promote recovery, but which can also become pathological.

Despite this robust and unexpected difference in local edema, both AITC and WaTx produced substantial and long-lasting hypersensitivity to thermal and mechanical stimuli (Figure 2.5D, E; 2.11E). Presumably, in the absence of peripheral inflammation, the toxin drives pain hypersensitivity primarily through a centrally-mediated mechanism. Because most TRPA1-positive sensory neurons also express the capsaicin receptor, TRPV1, we could ablate synaptic connections between TRPA1-expressing nerve fibers and the spinal cord by injecting capsaicin into the intrathecal (spinal) canal. While this manipulation ablates the central terminals of these neurons, their peripheral terminals are preserved and still capable of releasing inflammatory peptides (Figure 2.11G) (Cavanaugh et al., 2009; Emrick et al., 2018). Indeed, in such animals, injection of AITC into the paw produced swelling, but not acute nocifensive behavior (Figure 2.11H-J). Furthermore, these animals developed mechanical hypersensitivity (albeit with a delayed onset) that is likely produced when TRPV1/TRPA1-negative sensory fibers are activated by peripheral inflammation (Figure 5E). When capsaicin-ablated animals were treated with WaTx,

they also lacked acute nocifensive behavior, but failed to exhibit any signs of mechanical hypersensitivity (Figure 2.5E), consistent with a predominantly central mechanism of toxin-evoked sensitization. Thus, WaTx pharmacologically isolates the central component of TRPA1-mediated pain hypersensitivity, reflecting its ability to elicit mode-specific channel gating.

## Discussion

TRP channels are complex polymodal signal detectors that are capable of integrating information from physical and/or chemical stimuli to modulate cell excitability in the face of changing environmental or physiological conditions (Clapham, 2003; Latorre et al., 2009; Venkatachalam and Montell, 2007). In the context of the primary afferent nociceptor, this concept has great significance for understanding how tissue injury and inflammation produce pain hypersensitivity (Bautista et al., 2013; Julius, 2013). The capsaicin receptor, TRPV1, has served as a model for delineating biophysical and structural underpinnings of polymodality, reflecting the channel's rich pharmacology and the availability of numerous structurally and functionally distinct activators (heat, extracellular protons, bioactive lipids, pungent vanilloids, and peptide toxins) with which to probe these mechanisms (Basbaum et al., 2009; Julius, 2013). TRPA1 also plays a key role in nociception and inflammatory pain, but a comparative dearth of pharmacological tools has limited our understanding of the physiological and biophysical complexity of this channel, and thus potential strategies for controlling its function (Nilius et al., 2011). The identification of WaTx as a chemically and mechanistically novel TRPA1 activator helps to fill this gap. Indeed, we have exploited this toxin to identify a previously unrecognized open state of the channel that elicits distinct physiological and behavioral outcomes, providing proof-of-principle that the allosteric nexus of TRPA1 can be pharmacologically targeted to tune channel activity in a manner more subtle than previously appreciated, which may have therapeutic value.

### *Scorpions produce a TRP channel toxin*

*Scorpiones* represent the most ancient extant source of arachnid venoms. These creatures are best known for deploying α and β–type toxins that target voltage-gated sodium and potassium channels for offense and defense (Bosmans and Tytgat, 2007; Kalia et al., 2015; Quintero-Hernandez et al.,

2013), but have not previously been appreciated to deploy TRP channel toxins. Our analysis of WaTx species selectivity (Figure 2.9A) suggests that the Black Rock scorpion has evolved this toxin for the defensive purpose of deterring mammalian predators, rather than subduing invertebrate prey. WaTx belongs to a small, enigmatic family of orphan scorpion toxins (κ-KTx), whose name derives from the finding that one such toxin (Hefutoxin, κ-KTx1.1) functions as a low affinity blocker of cloned *Shaker* type potassium channels. However, *bona fide* physiological targets and mechanisms of action for this or other κ-KTx family members remain unknown (Quintero-Hernandez et al., 2013; Srinivasan et al., 2002). Our findings now pinpoint a high affinity physiologic target for one such compact, cysteine-stabilized helical-hairpin toxin. This broadens our view of the potential pharmacological properties and applications for members of this toxin family, which share a common fold but little sequence similarity.

***WaTx is a novel cell-penetrating peptide***

Peptide toxins are generally assumed to bind to extracellular domains of their protein targets, which in many cases likely involves partial penetration of the toxin into the membrane and formation of stabilizing interactions with lipids in the outer leaflet of the bilayer (Gao et al., 2016; Hille, 2001; Jung et al., 2005; Lee and MacKinnon, 2004; Mihailescu et al., 2014). WaTx takes this process to the extreme by fully translocating across the bilayer to access a cytoplasmic binding site on TRPA1. Mechanism underlying membrane translocation by polycationic peptides remain debated (Bechara and Sagan, 2013; Guidotti et al., 2017; Kauffman et al., 2015). Specifically, much attention has been paid to the question of whether such peptides translocate passively or are taken up by energy-dependent cellular processes (*e.g.*, endocytosis). Our experiments with excised membrane patches and liposomes support a passive penetration mechanism for WaTx, which

likely constitutes the rate-limiting step for target engagement and channel activation (Figures 1G; 2D, E; and 3E).

Many CPPs, such as the HIV transactivator (Tat) or a fly Antennapedia homeoprotein-derived peptide (penetratin), lack well defined tertiary structure, but possess features that have been implicated in their cell penetrating properties, including overall hydrophobic or amphipathic character and/or the presence of cationic patches (Guidotti et al., 2017; Heitz et al., 2009; Joliot and Prochiantz, 2004). WaTx adopts a highly ordered and stable tertiary fold that forms a basic patch and dipole element that we implicate in cell penetration, providing a new model for studying the properties of passively translocating CPPs. While Maurocalcin, another highly structured scorpion toxin of the inhibitor-cysteine-knot type, also accumulates in cells to target the ER-localized ryanodine receptor, its penetration mechanism remains poorly understood and may involve both energy-dependent and independent processes (Quintero-Hernandez et al., 2013). In any case, our findings raise the intriguing possibility that other members of the κ-KTx family (or other highly structured peptide toxins) are adept at cell penetration and represent new pharmacological probes for identifying and manipulating intracellular sites on receptors, channels, or other targets.

***The 'allosteric nexus' controls TRPA1 gating***

WaTx and wasabi provide a striking example of convergent evolution wherein structurally dissimilar animal- and plant-derived irritants target the same domain to modulate TRPA1. In the case of WaTx, this evolutionary pathway reflects the 'solution' of two challenges: recognizing a key control point on TRPA1 and crossing the plasma to interact with this site. Furthermore, our results show that TRPA1's allosteric nexus can function as a polymodal detector of diverse physiologic stimuli, including covalent and non-covalent ligands. This stands in contrast to

TRPV1, where plant-derived vanilloids bind to a pocket deep within the bilayer, whereas spider toxins bind to the extracellular domain of the channel, likely reflecting the importance of these distinct regions for detecting physiologically relevant TRPV1 modulators, such as bioactive lipids and extracellular protons, respectively (Bohlen et al., 2010; Siemens et al., 2006)

While electrophiles and WaTx converge on a common site, they act through distinct mechanisms: covalent modification by electrophiles increases the probability of channel opening, whereas non-covalent WaTx binding stabilizes the open state and prolongs open time, reminiscent of the differential actions of benzodiazepines and barbiturates on $GABA_A$ receptors, which target non-overlapping sites on the same channel subunit to enhance open probability or mean open time, respectively—properties that underlie the distinct clinical utilities of these allosteric modulators (Nicoll et al., 1975; Twyman et al., 1989). In this same vein, understanding the precise structural basis of WaTx and electrophile action may provide important insights into the function of the allosteric nexus and how this region of TRPA1 can be pharmacologically exploited to produce physiologically (and perhaps therapeutically) distinct outcomes.

### *TRPA1* $Ca^{2+}$ *permeability, peptide release, and pain*

One notable characteristic of WaTx-evoked responses is the substantially reduced permeability of TRPA1 to $Ca^{2+}$ ions. This observation suggests that the toxin and electrophiles stabilize distinct conformations of the gate and/or selectivity filter. Indeed, similar observations have been made for TRPV1 when comparing heat- and capsaicin-evoked currents (Chung et al., 2008; Tominaga et al., 1998), possibly reflecting the conformationally dynamic nature of the outer pore domain and associated selectivity filter (Bohlen et al., 2010; Cao et al., 2013; Gao et al., 2016; Liao et al., 2013). Our finding that TRPA1 also exhibits profound changes in ion selectivity suggests that these domains may likewise be conformationally dynamic and participate in both ion selectivity

and channel gating. In the case of TRPV1, the ability to visualize these conformational changes was greatly facilitated by the discovery of DkTx and other gating modifier spider toxins (Bohlen et al., 2010; Cao et al., 2013; Gao et al., 2016; Liao et al., 2013) WaTx may similarly help stabilize key conformational states for future structural studies that reveal TRPA1 gating and permeation mechanisms, and how the 'allosteric nexus' controls these key channel functions.

While many TRP channels, such as TRPV1 and TRPA1, pass both mono- and divalent cations (and exhibit unusually high permeability for the latter), the relative contribution of these ionic species to physiological responses has been difficult to parse. Here we have been able to exploit the differential effects of AITC and WaTx to show that $Ca^{2+}$ entry through this channel *per se* is both necessary and sufficient to initiate neurogenic inflammation by promoting release of pro-inflammatory peptides from activated peripheral nociceptor terminals. In contrast, bulk cation current flow through TRPA1 in response to either agent is sufficient to depolarize the neuron and transmit information to the spinal cord to evoke acute and persistent pain (Figure 2.6). This differential activity has enabled us to unmask the central component of TRPA1-evoked pain hypersensitivity without the confounding contributions from peripheral inflammation, making WaTx a unique tool for future mechanistic studies of central neural pathways contributing to chronic pain. Moreover, further insights into the structural basis of WaTx action may suggest strategies for targeting the allosteric nexus to diminish the inflammatory component of TRPA1-mediated pain while preserving its acute protective role in chemo-nociception.

## Methods

### *Molecular biology and cell culture*

We used Full-length wild-type human TRPA1 and Texas rat snake TRPA1 (*Elaphe obsoleta lindheimeri*; GenBank ID: GU562966) subcloned into the mammalian/oocyte expression vector pMO for all experiments (Cordero-Morales et al., 2011; Gracheva et al., 2010). We designed TRPA1 chimaeras such that the junction points consisted of amino acid sequences conserved between the two orthologs (Figure 2.10K). Genscript (Nanjing, Jiangsu, CN) produced and verified all TRPA1 chimaeras and point mutants.

We cultured HEK (ATCC) cells at 37 °C, 5% $CO_2$ in DMEM Complete (DMEM-C; Dulbecco's modified Eagle's medium containing 10% (v/v) heat-inactivated calf serum, 100 U $ml^{-1}$ Penicillin G and 0.1 mg $ml^{-1}$ Streptomycin). For heterologous expression of ion channels, we transfected cells with 0.25-1 μg of plasmid DNA combined with 3x (w/w) Lipofectamine 2000 (Thermo-Fisher) for 4-8 hrs. in Opti-MEM (Thermo Fisher) before plating onto coverslips with (for excised patch experiments and $Ca^{2+}$-imaging experiments) or without (for all other experiments) 0.01% poly-L-Lysine (poly-L, MW 70-150,000, MilliporeSigma).

For analysis of WaTx effects in sensory neurons, we harvested trigeminal ganglia from early postnatal (P0-4) Sprague-Dawley rat or C57BL/6J mouse pups, digested them in Collagenase (1 mg $ml^{-1}$) followed by Trypsin (0.25% w/v) at 37 °C for 15 min. each. We then mechanically triturated digested ganglia in DMEM-C, then plated neurons onto coverslips coated with poly-L and 10 μg $ml^{-1}$ mouse laminin (PLL). Neurons were cultured for > 12 hrs. before use, under identical culture conditions to HEK cells.

***Animal husbandry***

Mice and rats were housed them at a density of 2-5 individuals/cage and 12 hr. light/dark cycle had *ad libitum* access to food and water. We conducted all animal care and behavioral experimentation in accordance with UCSF Institutional Animal Care Committee guidelines, the National Institutes of Health Guide of Care and Use of Laboratory Animals, and the recommendation of the International Association for the Study of Pain. In this study, adult (12-28 week-old) C57BL/6J mice (Jackson Laboratories) constituted the "wild-type" group and homozygous TRPA1 knockout mice on a C57BL/6J background constituted the "$TRPA1^{-/-}$" group. (Bautista et al., 2006)

***Venom library screening***

We prepared and screened ~100 invertebrate venoms, as described previously (Osteen et al., 2016). Briefly, we filtered *U. manicatus* venom with a 50 kDa MWCO filter (MilliporeSigma) to remove high molecular weight cell-lytic components (Zhang et al., 2017) and to buffer-exchange into Ringer's solution containing, in mM, 140 NaCl, 10 HEPES, 5 KCl, 2 $MgCl_2$, 2 $CaCl_2$, and 10 Glucose; pH 7.4 with NaOH; 290-300 mOsm $kg^{-1}$. We then performed ratiometric $Ca^{2+}$-imaging (described below) of HEK293T (HEK) cells stably expressing TRPA1 or TRPM8 (McNamara et al., 2007).

***WaTx Cloning***

We purified WaTx from approximately 1 mg of crude *U. manicatus* venom via reverse-phase HPLC on an analytical monomeric Grace Vydac $C_{18}$ column (300Å pore; I.D × L, 4.6 × 250 mm; No. 238EV54) where $H_2O$ with 0.1% TFA (v/v) constituted the stationary phase (solvent A) and 95% acetonitrile, 0.1% TFA (v/v) the mobile phase (solvent B) (Figure 2.7D). We first reconstituted the venom in 5% solvent B then separated its constituents with a linear gradient (0.8

ml $min^{-1}$) of 5-40% solvent B. We collected the resultant fractions, evaporated organic solvent under vacuum, and flash froze them in $LN_2$. We next lyophilized, sealed, and stored fractions at -80 °C until use. Of fractionated venom components, a single fraction recapitulated the crude venom's TRPA1-activating activity (Figure 2.7F). We mixed this fraction1:1 (v/v) with 5 mg $ml^{-1}$ α-cyano-4-hydroxycinnamic acid (CHCA) matrix before spotting the solution onto a target for mass spectrometry (MS) analysis. We collected externally calibrated (ProteoMass Kit, MilliporeSigma) spectra over a range of 1000-5000 *m/z* on an Axima Performace MALDI-ToF/ToF mass spectrometer (Shimadzu) in reflectron mode. These spectra displayed a single species of $[M+H]^+$ 3854.5 (Figure 2.7E).

To determine this peptide's sequence *de novo*, we purified ~50 pmol from 5 mg venom as above, then reduced and alkylated the resulting material with 500-fold molar excess TCEP at 37 °C for 30 min. followed by 500-fold molar excess Iodoacetamide (IAM) at RT for 30 min. in 25 mM $NH_4HCO_3$. We then analyzed linear, partially cysteine carbamidomethylated ($C^{AM}$) toxin via nanospray sample introduction into an LTQ-Orbitrap Velos tandem mass spectrometer (Thermo Scientific). We acquired ion trap collision-induced dissociation (CID) and beam-type higher-energy C-trap dissociation (HCD) spectra from *m/z* 1007.9475 ($4^+$), which represents the toxin featuring three $C^{AM}$. We then measured fragments from both activation methods were measure with high resolution in the Orbitrap. Manual interpretation of the resulting CID and HCD spectra yielded a complete mature peptide sequence (Figure 2.7G; Table 1) of calculated oxidized $[M+H]^+$ 3853.7, in reasonable agreement with our MALDI-ToF analysis. We confirmed the identity the WaTx's N-terminal dipeptide by carrying out a tBLASTn search against an extant *U. manicatus* venom gland transcriptome (SRX288428) (Sunagar et al., 2013), which also yielded candidate signal and pro-peptide sequences (Figure 2.7g). We inferred WaTx's disulfide bonding pattern

based on homology considerations with κ-KTx family of peptide toxins (Figure 2.1C) (Srinivasan et al., 2002). Based on this phylogeny, WaTx may also be referred to as κ-KTx 6.1 (Tytgat et al., 1999) and/or τ-Scorpionitoxin-Um1a (King et al., 2008).

We purchased synthetic WaTx and WaTx mutants from AnaSpec (Fremont, CA) or LifeTein (Somerset, NJ). These companies produced mature, folded, and by chemical synthesis with directed disulfide bond formation between C9-C27 and C13-C23 at 5 mg scale to > 90% purity, as assessed by HPLC. Because of the low abundance of (~10 pmol $mg^{-1}$ venom) of toxin in venom and limited availability of scorpions for milking, we used synthetic WaTx in all further experiments. For all assays, we resuspended and aliquoted synthetic WaTx in $H_2O$ upon delivery. We immediately flash froze these aliquots in $LN_2$; then lyophilized, sealed, and stored them at -80 °C until use. We confirmed the proper folding of WaTx and mutants using CD spectroscopy; these data were collected over a 1 mm pathlength across 190-250 nm on an Aviv CD Spectrometer 215 using 10 μM WaTx in PBS, pH 7.4, then processed in CDToolX (Miles and Wallace, 2018).

***$Ca^{2+}$ imaging***

Prior to imaging, we loaded adhered cells with indicator solution (Ringer's solution containing 0.1 mg $ml^{-1}$ Fura-2 AM dye and 0.02% (w/v) Pluronic F-127 for 30 min. at room temperature (RT) in the dark. We then excited cells using either a Lamda LS (Sutter) (Figure 2.1B; 2.7C, F, and K; 2.9A) or DG-4 illuminator (Sutter) (Figure 1A; 7H-K; 9F, H). We collected fluorescent emissions with an ORCA-ER camera and controller (Hamamatsu), and digitized and analyzed the data with MetaFluor (Molecular Devices). To quantify the data, we calculated the ratio of 340 to 380 nm fluorescence after background subtraction. Experiments were carried out either with cells adhered to a glass slide coated with poly-L and isolated in silicon wells (O.D. x Depth, 2.5 x 2.0 mm) Figure 2.1B; 2.7C, F, and K; 2.9A); or to a coverslip coated with poly-L (HEK) or PLL (neurons)

in order to make pharmacological manipulations under laminar flow using a pressure-driven micro-perfusion system (SmartSquirt, Automate Scientific) (Figure 2.1A; 2.7H-K; 2.9F, H).

***Electrophysiology***

We fashioned capillary glass pipettes from borosilicate glass with filament (O.D × I.D, 1.10 × 0.86 mm, Sutter Instruments) and fire-polished them a resistance of 2-5mΩ for whole-cell or 6-12mΩ for excised-patch patch-clamp recordings. We then made electrophysiological measurements at RT using an Axopatch 200B amplifier (Axon Instruments) and digitized the data with a Digidata 1550B (Axon Instruments). We executed voltage protocols and monitored resulting currents on-line with pClamp10 (Molecular Devices), which we analyzed off-line in pClamp and Prism (GraphPad). We carried out all electrophysiological recordings and pharmacological manipulations under laminar flow using a pressure-driven micro-perfusion system (SmartSquirt, Automate Scientific).

We performed whole-cell recordings in a bath solution of nominally $Ca^{2+}$-free Ringer's solution, sampling data at 10 kHz and filtering it at 1 kHz. For TRP channels, we used an internal solution containing, in mM, 140 $CsMeSO_4$, 10 HEPES, 1 $MgCl_2$, and 1 EGTA; pH 7.2 with CsOH; 300-310 mOsm $kg^{-1}$ with sucrose. For $K_v$ channels, we replaced $CsMeSO_4$ with equimolar $KMeSO_4$, pH 7.2 with KOH in the pipette. Unless otherwise stated, I-V curves were generated from whole-cell patch clamp recordings in response to 500 msec. steps from -80 to 80 mV in 10 mV increments. Tail-current measurements (Figure 1C, and 10A, B) were made at -120 mV following 500 ms steps from -80 to 80 mV in 10mV increments or 70 to 145mV in 15mV increments in whole-cell patch-clamp mode. Data were leak-subtracted on-line (P/4), normalized to the currents obtained at 70 mV, then fit by non-linear regression to the Boltzmann equation to determine $V_{1/2}$.

We carried out cell-attached and excised-patch recordings in symmetrical solutions of, in mM, 150 NaCl, 10 HEPES, 2 EGTA, 1 $MgCl_2$, 1 $IP_6$, 6 NaOH; pH 7.3 with NaOH; 300-310 mOsm $kg^{-1}$; sampling at 20 KHz and filtering at 2 kHz. For monovalent cation selectivity experiments (Figure 4F; 11D, E), the bath solution contained in mM, 150 NaCl, 10 HEPES, 2 EGTA, 1 $IP_6$, 6 NaOH at pH 7.3 with NaOH and 300-310 mOsm $kg^{-1}$. The pipette solution was identical except we replaced $Na^+$ with equimolar $K^+$, $Cs^+$, $Li^+$, or $NMDG^+$ and set to pH 7.3 with, as appropriate, KOH, CsOH, or Trizma. For divalent cation selectivity experiments, the bath solution contained, in mM: 75 $CaCl_2$ or $MgCl_2$, 10 HEPES, pH 7.3 with Trizma; 300-310 mOsm $kg^{-1}$. The pipette solution contained in mM: 150 NaCl, 10 HEPES, 2 EGTA, 1 $IP_6$, 6 NaOH; pH 7.3 with NaOH; 300-310 mOsm $kg^{-1}$. We determined the reversal potential as the minimum of the standard deviation of the average trace resultant from at least 10 sweeps of a 500 ms. ramp from -100 to 80 mV under a given pharmacological condition (Bobkov et al., 2011) (Figure 2.10F, G). We then calculated relative permeability ratios using this value to solve the Goldman-Hodgkin-Katz equation (Hille, 2001).

***FRET-based liposome loading***

After drying soybean polar lipids (Avanti) under argon and dessicating them for 1 hr. under vacuum, we resuspended lipids in liposome buffer containing (in mM) 150 NaCl and 10 HEPES pH 7.4 followed by bath sonication for 10 min. We doped fluorophore AlexaFluor568-IgG (donkey anti-goat, Thermo-Fisher, No A11057.) was to this mixture to a final concentration of 2 μg $ml^{-1}$. We next fashioned large unilamellar vesicles (LUVs, ~100 nm mean diameter) by extrusion through a 0.2 μm filter. To remove unincorporated acceptor fluorophore, we pelleted LUVs at 100,000 x *g* for 40 min. at 4°C. We then resuspended liposomes in liposome buffer to a concentration of 2 mg $ml^{-1}$ with 1000-fold molar excess Trypan Blue dye to quench extra-

liposomal excitatory fluorescence. We serially diluted N-terminal conjugated green fluorescent WaTx (AlexaFluor488-K-WaTx or WaTx K7A, LifeTein) into 96-well plates containing liposomes for Förester resonance energy transfer (FRET) analysis. We then collected FRET emission every min. for 30 min. at 23 °C using an excitation wavelength of 480 nm and emission wavelength of 570 nm on a Synergy H4 plate reader (BioTek). After subtracting background excitation fluorescence from donor and acceptor fluorophore-only conditions, we fit the data fitting with a one-phase association exponential function in Prism to derive the FRET curves and kinetic parameters of loading shown (Figure 2.2D, E).

***WaTx structure determination***

We suspended WaTx at 300 μM in 0.38 mm thin walled glass tubes rated 600 MHz (O.D. × Length, 5 × 1778 mm; Wilmad LabGlass, No. 535-PP-7) in unbuffered 10 or 100 % (v/v) $D_2O$, pH < 4.0. We collected [$^1$H, $^1$H]-COSY, TOCSY, and NOESY spectra, and natural abundance [$^{13}$C, $^1$H]-HSQC spectra at ambient temperature on an 800 MHz NMR spectrometer (Bruker Avance I 800) using a Z-gradient 5mm TXI Cryoprobe at 298 K, then processed the data in TopSpin (Bruker). We referenced proton chemical shifts to an external DSS standard and $^{13}$C shifts indirectly from this value. We then manually assigned resonances and generated restraints in CCPN Analysis (Vranken et al., 2005) (Figure 2.9J, K; Table 2.2). DANGLE (Cheung et al., 2010) predicted additional dihedral restraints from the NOESY and HSQC assignments. We calculated structures with ARIA (Rieping et al., 2007) and evaluated their quality with PSVS (Bhattacharya et al., 2007). In the final iteration, we solved 200 structures then refined 50, selected based on total energy, in explicit water (Table 2.2). We deposited these models (All-atom RMSD = 0.332) and underlying NMR data to the PDB and BMRB with accession codes 6OFA and 30597, respectively.

***Biolayer Interferometry***

We transfected HEK cells for 14 hrs. in DMEM-C with 3 μg of indicated constructs mixed with 3x (w/w) Lipofectamine 2000 (Thermo-Fisher). We washed cells once with PBS, then harvested them with buffer containing (in mM) 320 sucrose, 50 tris-Cl pH 7.5, 1 EDTA, 1 $IP_{6,}$ 6 NaOH, and 1x Protease Inhibitor Cocktail (Roche). After isolating live cells floated by centrifugation at 750 x *g* for 10 min at 4°C we pelleted them by centrifugation at 100,000 x *g* for 45 min at 4°C. We mechanically homogenized this pellet in harvest buffer (minus sucrose) to generate crude membranes (Maricq et al., 1991), then diluted these fragments to 0.5 mg $ml^{-1}$ protein content as determined by Bradford assay (Bradford, 1976). We used 100-1000 μg crude membranes for analysis by biolayer interferometry on an OctetRed 394 instrument (Pall/ForteBio) using N-terminal biotinylated toxin (Biotin-GSGS-WaTx, LifeTein) coupled to streptavidin sensors (Pall/ForteBio) as a probe. Sensorgrams from mock-transfected membranes measured non-specific binding, which we then subtracted on-line. We determined the kinetic parameters for WaTx:hTRPA1 binding directly ($k_{off}$) or by estimation ($k_{on}$ and $K_D$) assuming a concentration of 1 pM TRPA1 binding sites. We made this estimate by controlling the total live cell input to the assay (~$2.0 \times 10^6$) and assuming a lowest-affinity binding scenario where (1) WaTx binds 1:1 to TRPA1 monomers and (2) each cell expresses the maximum number of TRPA1 channels—approximately 1000, equivalent to 4000 receptor sites. This second assumption was made based on our electrophysiological studies of receptor, *cf.* Figure 2.1D; 2.10I).

***Animal Behavior***

For all experiments, treatment consisted of 20 μL 0.9% (w/v) saline (vehicle), WaTx dissolved in vehicle, or 0.75% (v/v) AITC in mineral oil injected intraplantar to the hindpaw. After treatment,

we scored nocifensive behavior (biting and/or licking of the injected paw) for 20 min. immediately following injection. We quantified thermal hypersensitivity as the latency to first nocifensive response (flinch, bite, and/or lick) of the injected paw on a 48 °C hotplate, and mechanical allodynia by applying von Frey hairs (0.008 - 4.0 g) applied to the treated paw and scoring the responses using the Up-Down method (Chaplan et al., 1994). To assess neurogenic inflammation, we quantified local edema as an increase in paw thickness, measured by digital calipers (VWR), and as an increase vascular permeability, measured by Evan's Blue Dye (EBD) extravasation at one hr. post-algesic injection. We injected EBD (0.5% (w/v) in PBS) retro-orbitally (20 mg $kg^{-1}$) prior to the experiment; following caliper measurements we euthanized the mice and extracted EBD from the paw as described previously (Zhang et al., 2017), then quantified EBD extravasation via 620 nm absorption on a spectrophotometer. Finally, we carried out intrathecal capsaicin ablations as described previously (Cavanaugh et al., 2009; Emrick et al., 2018; Osteen et al., 2016), and confirmed ablation by hotplate test at 50 °C (Figure 2.11E). We collected and scored all behavioral data such that the experimenter was blind to either the mouse genotype, treatment received, or both.

***Immunohistochemistry***

We anesthetized adult mice with pentobarbital then perfused them transcardially with PBS followed by 10% neutral buffered formalin (NBF). We dissected, postfixed in 10% NBF at 4 °C overnight (O/N), then cryoprotected spinal cords in PBS with 30% (w/v) sucrose O/N at 4 °C. Before sectioning, we embedded tissue samples in OCT compound (VWR) at −20 °C. We then thaw-captured 20 µm spinal cord sections prepared from segments L4/L5 with a Leica CM3050 S cryostat onto glass slides. We blocked slides containing sections of spinal cord for 1 hr. at RT in PBS plus 0.1% (v/v) Triton X-100 (PBST) with 10% normal goat serum (NGS). Then we rinsed

slides once with PBST containing 2.5% NGS and incubated them O/N with rabbit anti-Fos (1:2,000; Biosensis, No. R-1751-25) in PBST with 2.5% NGS at 4 °C. Following incubation, we washed slides thrice in PBS, rinsed once with PBST, then incubated them in secondary antibody (1:1,000; goat anti-rabbit AlexaFluor488-IgG, Thermo-Fisher, No. A11034) for 2 hrs. in PBST at RT in the dark. Following incubation, we washed slides thrice with PBS then mounted them in ProLong Gold antifade reagent with DAPI (Thermo-Fisher) under a coverslip. We acquired epifluorescent images with a Leica DMRB microscope mounted with an Infinity 3-3UR Monochrome CCD digital camera using Infinity Analyze software. Following capture, we analyzed and false-colored (grayscale) micrographs in ImageJ. We counted cFos-positive cells blind to genotype and treatment.

***Enzyme-linked Immunosorbent Assay (ELISA)***

Enzyme-linked immunosorbent assays detected CGRP release from 1 DIV primary rat trigeminal neurons (harvested on P0-P1), cultured as described above. To prepare cultures, we applied either indicated treatments (Figure 2.5I) for 5 min. at RT. We pooled supernatants from three replicate coverslips into a single well of a 96-well plate containing a monoclonal anti-human CGRP antibody (rat cross-reactivity: 120%; Bertin Bioreagents, No. A08481) and incubated them overnight at 4 °C, then developed them per the manufacturer's instructions (Bertin Bioreagents, No. A05481). Briefly, we first added acetylcholinesterase coupled to an anti-CGRP antibody (No. A04481), then monitored cleavage of dithio-bis-nitrobenzoic acid (DTNB) via increased TNB fluorescence at 414nm on a Synergy H4 plate reader (BioTek) every min. for 30 min. We determined the amount (pg $ml^{-1}$) of CGRP release (by comparison to a standard curve derived from purified CGRP (Bertin Bioreagents, No. A05481), and normalized all data to the amount of CGRP released by AITC treatment.

### *Quantification and Statistical Analysis*

Herein we summarized data using the mean ± SEM unless otherwise noted. We carried out statistical testing in Prism (GraphPad) using either a two-tailed student's *t* test, or One- or Two-Way ANOVA with a *post-hoc* Holm-Sidak correction for multiple comparisons, as indicated in the figure legends. *A priori*, we set $\alpha = 0.05$ and represent statistical significance as: * $P < 0.05$, ** $P < 0.01$, *** $P < 0.001$, and **** $P < 0.0001$. Parametric significance tests assuming equal variance and a normal distribution of data means are justified given the experimental design, and are the standard tests for similar experiments. We selected sample sizes for all experiments on the basis of our laboratory and others' experience with similar assays, and in consideration of reagent availability and technical feasibility. We made no predetermination of sample size and thus carried out a minimum of independent experiments required for statistical significance and reproducibility.

### *Data Availability*

The WaTx peptide sequence has been deposited to UniProt with accession code C0HLG4. Atomic coordinates for the solution structural ensemble of WaTx and underlying NMR chemical shifts and peaks have been deposited to the PDB and BMRB with accession codes 6OFA and 30597, respectively.

## Figures

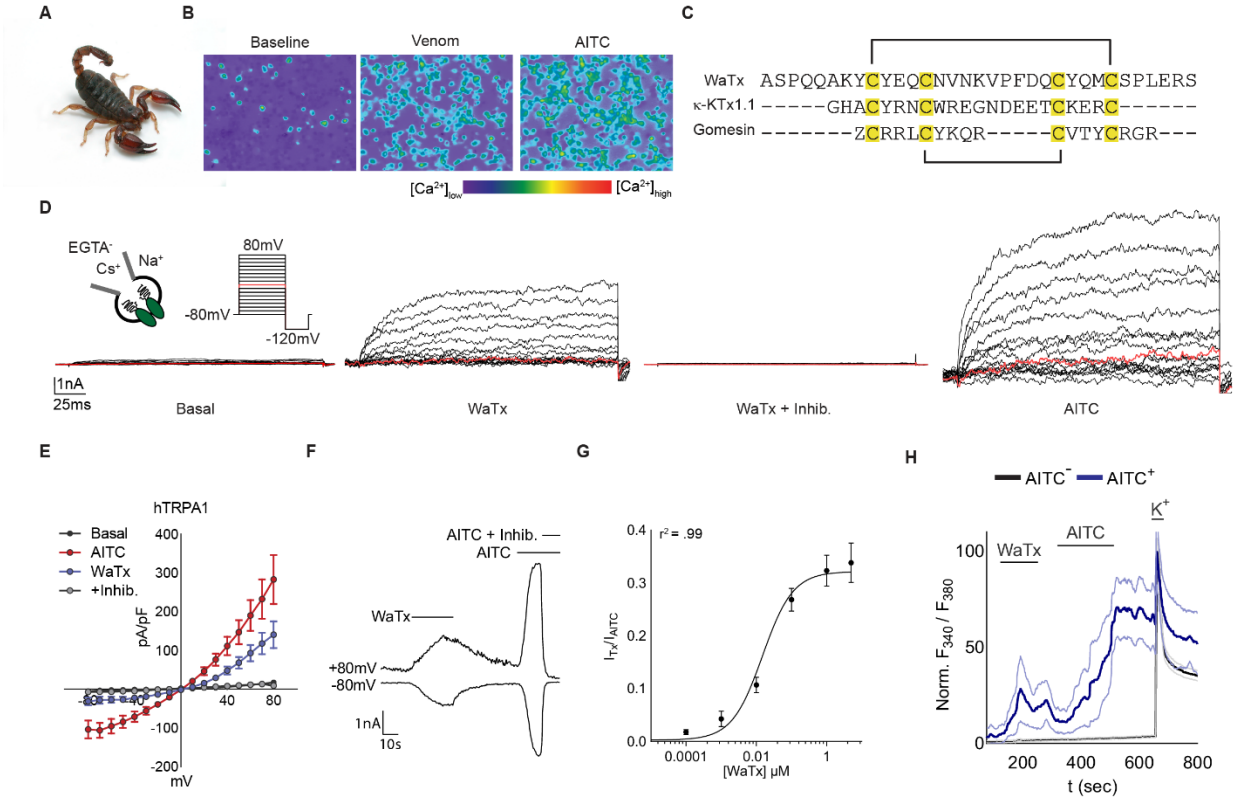


***Figure 2.1 WaTx, a TRPA1-targeting peptide toxin from scorpion***

**(A)** Australian Black Rock scorpion, *U. manicatus* (Museums Victoria, Creative Commons)

**(B)** $Ca^{2+}$ responses in rat TRPA1-expressing HEK cells exposed to scorpion venom (~0.1 mg $ml^{-1}$), followed by AITC (333 µM).

**(C)** WaTx sequence, disulfide bonding configuration (black brackets), and manual alignment to example arachnid toxins with a 1-4, 2-3 disulfide bonding pattern, κ-KTx1.1, Hefutoxin (Srinivasan et al., 2002) and Gomesin (Silva et al., 2000). "Z" denotes pyroglutamate.

**(D)** Representative whole-cell recordings and**,** (E) derived current-voltage relationships for human (h) TRPA1 currents in HEK cells. WaTx (1 µM), WaTx + inhibitor (10 µM, A 967079), AITC (100 µM); *n* = 5 cells.

**(F)** Time-course of hTRPA1 responses in HEK cells. WaTx (250 nM), AITC (500 µM), and AITC + inhibitor (10 µM, A 967079); representative of *n* = 3 - 10 cells/treatment.

**(G)** WaTx dose-response relationship in HEK cells. Data fit by non-linear regression; *n* = 3-26 cells/dose.

**(H)** WaTx (5 µM) and AITC (50µM) responses in cultured postnatal mouse trigeminal neurons. Representing *n* = 3-10 experiments.

All summary data, mean ± SEM. See also Figures 2.7, and 2.10; and Table 2.1

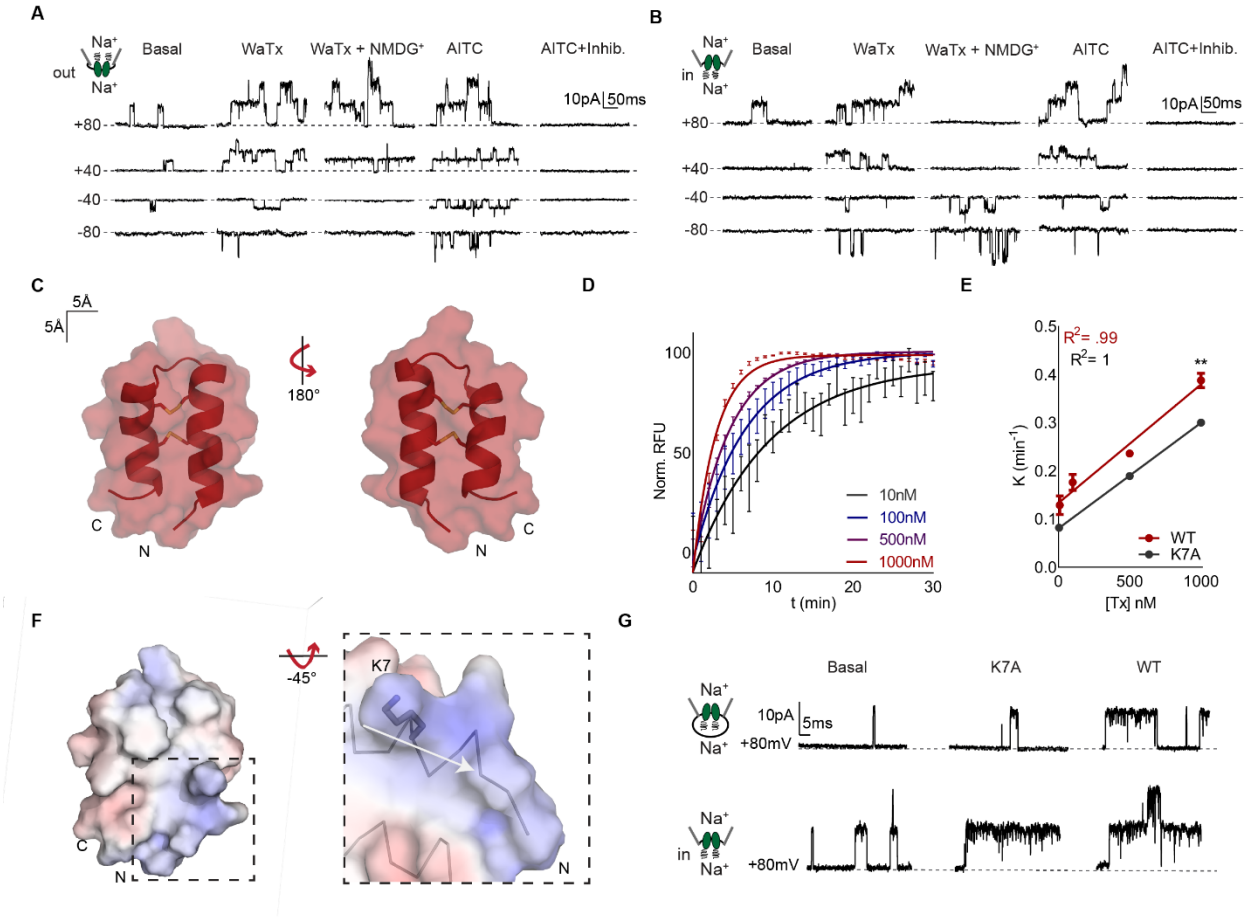


***Figure 2.2 WaTx is a cell penetrating peptide***

**(A)** Excised HEK cell patch recordings of TRPA1 single channels in outside-out ($n$ = 10) or (B) inside-out, ($n$ = 14) configuration in response to bath application of WaTx (100 nM), NMDG (150 mM), AITC (50 μM), and inhibitor (10 μM, A 967079**)**. The orientation of the patch was confirmed by replacement of $Na^+$ with the impermeant cation, $NMDG^+$ and the identity of the single channels by application of the selective TRPA1 antagonist, A 967079 (Chen et al., 2011).

**(C)** Surface and cartoon representation of the closest-to-average (Kabsch RMSD = 0.355; mean Kabsch RMSD = 0.691) WaTx conformer (one of fifty) with disulfide bonds shown, determined by solution NMR spectroscopy. PDB ID: 6OFA.

**(D, E)** Kinetics and dose-dependence of toxin loading into soybean polar liposomes. Data fit by **(D)**, nonlinear regression, one-phase exponential association and **(E)**, linear regression. Unpaired, two-tailed Student's $t$-test, $n$ = 6-8 wells/dose.

**(F)** WaTx electrostatic surface (Baker et al., 2001) contoured at ± 5 kT/$e^-$. Inset: WaTx N-terminus with dipole moment vector drawn in white (220 Debye, 1.65 Debye/atom (Felder et al., 2007)).

**(G)** Single-channel recordings of WT and K7A WaTx in (top) cell-attached and (bottom) inside-out HEK cell patch configuration; $n$ = 5 inside-out and 12 cell-attached patches.

All summary data, mean ± SEM. See also Figure 2.8 and Table 2.2

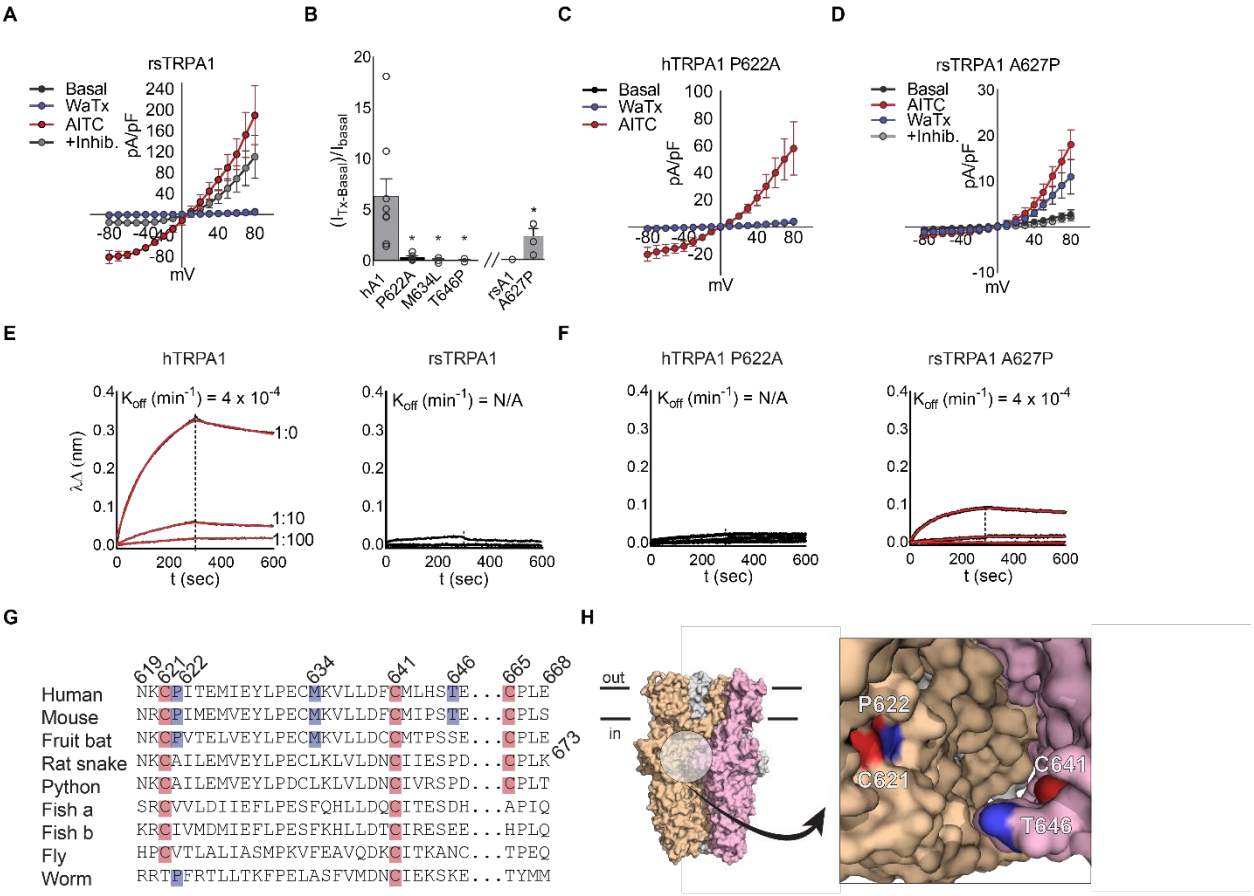


***Figure 2.3 WaTx interacts directly with TRPA1's allosteric nexus***

**(A)** Rat snake (rs) TRPA1 current-voltage relationships in transfected HEK cells. WaTx (100 nM), AITC (500 µM), AITC + inhibitor (50 µM, HC 030031); *n* = 4 cells. Note: inhibitor A 967079 is ineffective against rsTRPA1 while the selective TRPA1 inhibitor HC 030031 is effective (Banzawa et al., 2014; McNamara et al., 2007).

**(B)** WaTx-evoked whole cell currents for loss-of-function hTRPA1 mutants and gain-of-function rsTRPA1 mutant. WaTx treatments: 1 µM to hTRPA1 and 5 µM to rsTRPA1 constructs. One-Way ANOVA with *post-hoc* Holm-Sidak correction for multiple comparisons (hTRPA1 constructs) and unpaired two-tailed Student's *t*-test (rsTRPA1 constructs.). Recordings from transfected HEK cells; *n* = 3-9 cells/construct.

**(C, D)** Current-voltage relationships for hTRPA1 P622 mutants, which dictate species selectivity of TRPA1. Recordings from transfected HEK cells; *n* = 4-5 cells/treatment.

**(E, F)** Biolayer-interferometry derived sensorgrams depicting association of crude HEK cell membranes expressing TRPA1 to WaTx-coated sensors. Non-specific binding to mock-transfected membranes was subtracted, and resultant curves fit by nonlinear regression to a one-phase exponential association and dissociation model; Data are representative of *n* = 3-6 independent experiments/construct.

**(G)** Multiple-sequence alignment of TRPA1 orthologs and **(H)** proposed WaTx binding pocket mapped to the cryo-EM structure of human TRPA1 (PDB ID: 3J9P). Electrophile-reactive cysteines highlighted red; residues implicated in WaTx binding, blue.

All summary data, mean ± SEM. See also Figure 2.9.

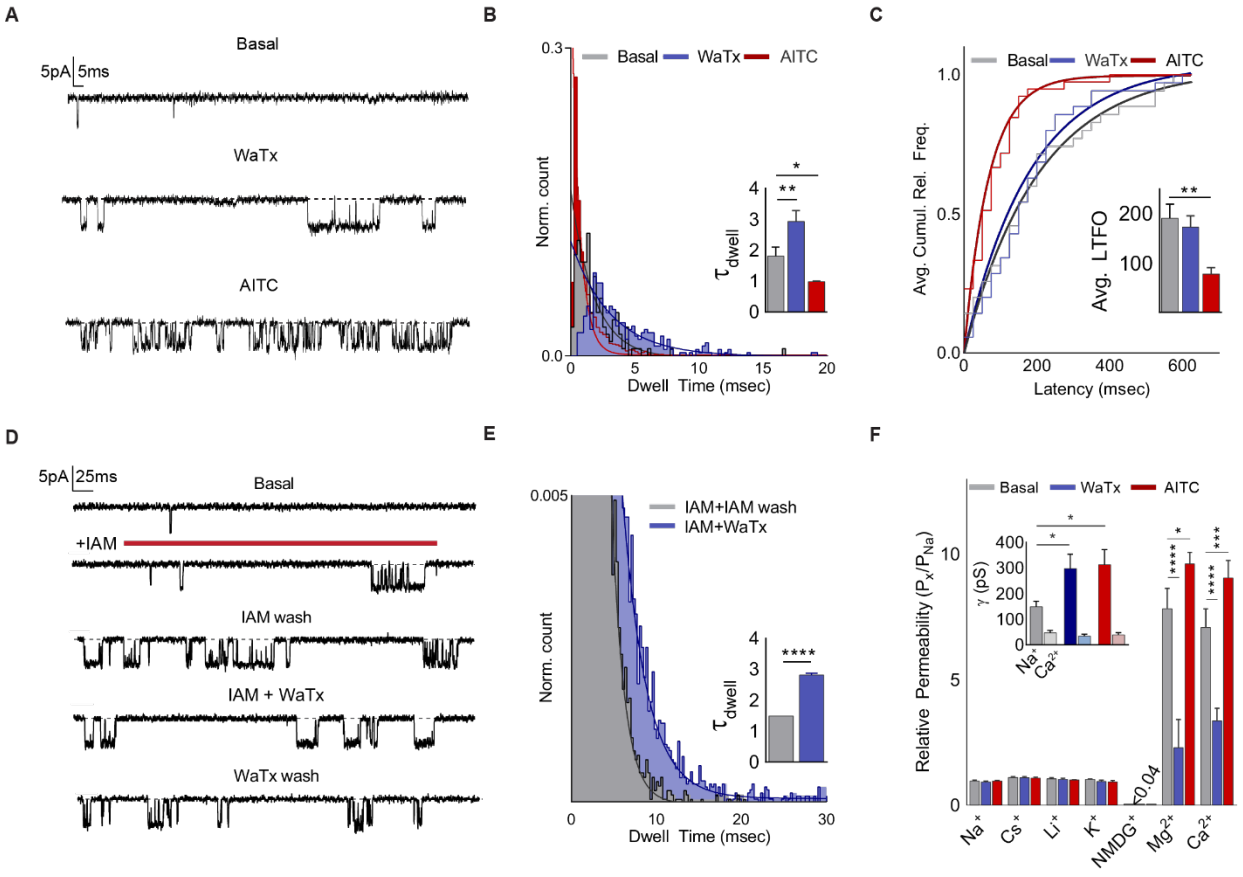


***Figure 2.4 WaTx is a mode-specific gating modifier***

**(A-C)** Inside-out HEK cell patch recordings ($V_h$ = -40 mV) of spontaneous, WaTx (100 nM) or AITC (10 μM)-evoked TRPA1 openings, quantified with respect to (B)**,** dwell time (*n* = 6-8 patches/treatment) and (C) latency to first opening (*n* = 13-14 patches/treatment). One-Way ANOVA with *post-hoc* Holm-Sidak correction for multiple comparisons.

**(D)** Inside-out HEK cell patch recordings ($V_h$ = -40 mV) showing WaTx (1 μM) effect on a single, irreversibly activated (Iodoacetamide, 100 μM) TRPA1 channel (*n* = 9-11 patches/treatment), quantified with respect to (E) dwell time. Unpaired two-tailed Student's *t*-test.

**(F)** TRPA1 ionic selectivity and conductance for spontaneous, WaTx (100 nM)- or AITC (50 μM)-evoked openings (*n* = 3-7 HEK cell patches/condition). Two-way ANOVA with *post-hoc* Holm-Sidak correction.

All summary data, mean ± SEM. See also Figure 2.10.

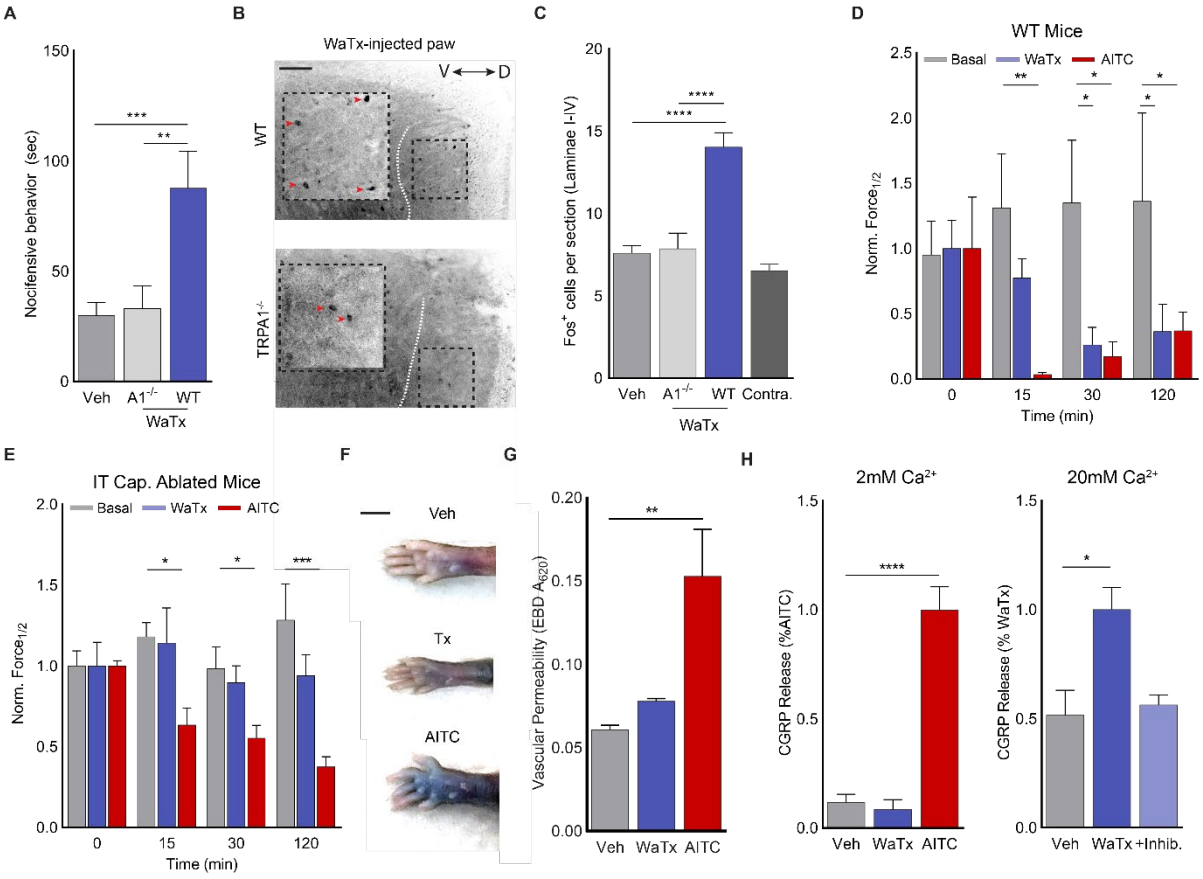


***Figure 2.5 WaTx elicits TRPA1-dependent non-inflammatory pain***

**(A)** WaTx-evoked nocifensive behavior in mice. One-way ANOVA with *post-hoc* Holm-Sidak correction for multiple comparisons; $n$ = 12-20 mice/group.

**(B, C)** Induction of cFOS expression in the superficial laminae of the mouse spinal cord (dorsal to the dotted white line) after WaTx injection. Orientation of spinal cord along the dorsoventral axis indicated with bidirectional arrow. Inverted grayscale image with scale bar = 100 µm. One-way ANOVA with *post-hoc* Holm-Sidak correction for multiple comparisons; $n$ = 22-39 sections/group.

**(D, E)** Timecourse and magnitude of mechanical allodynia onset in **(D)** wild-type ($n$ = 8 animals/treatment) and **(E)** intrathecally capsaicin ablated mice ($n$ = 6-8 mice/treatment) in response to vehicle, WaTx (100nM), or AITC injection (0.75% v/v in mineral oil). One-way ANOVA with *post-hoc* Holm-Sidak correction for multiple comparisons.

**(F)** Paw edema and **(G)** vascular permeability in mice after WaTx (100nM) or AITC (0.75% v/v in mineral oil) injection. One-way ANOVA with *post-hoc* Holm-Sidak correction for multiple comparisons; $n$ = 4 mice/treatment. Scale bar: 5 mm.

**(H)** Measurements of CGRP release cultured neonatal rat trigeminal neurons under physiological (2mM) and high (20mM) extracellular $Ca^{2+}$ conditions. Treatments: vehicle (PBS, pH 7.4), WaTx (10 µM), AITC (100 µM), and inhibitor A 967079 (10µM). One-Way ANOVA with *post-hoc* Holm-Sidak correction for multiple comparisons; $n$ = 6-12 treatments/condition.

All summary data, mean ± SEM. See also Figure 2.11.

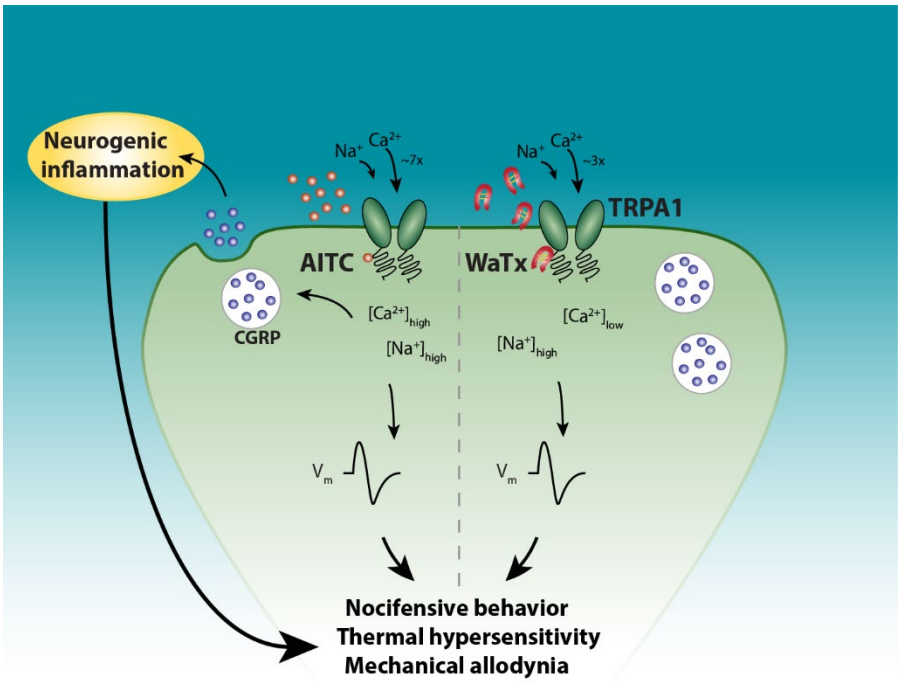


***Figure 2.6 WaTx versus electrophile action at a sensory nerve terminal***

Electrophilic irritants such as AITC act as membrane-permeable, covalent agonists for TRPA1, producing channel activation and neuronal depolarization; and, in turn, acute pain and subsequent hypersensitivities to noxious and innocuous stimuli. Concomitantly, electrophile activation produces robust $Ca^{2+}$ entry, leading to $Ca^{2+}$-mediated release of CGRP from dense-core vesicles and consequent neurogenic inflammation. In contract, WaTx acts as a cell-penetrating, non-covalent gating modifier, producing prolonged spontaneous TRPA1 openings and, consequently, neuronal depolarization and subsequent hypersensitivities. However, WaTx also decreases the relative $Ca^{2+}$-permeability of TRPA1, forestalling sufficient $Ca^{2+}$-entry to produce measurable CGRP release and neurogenic inflammation.

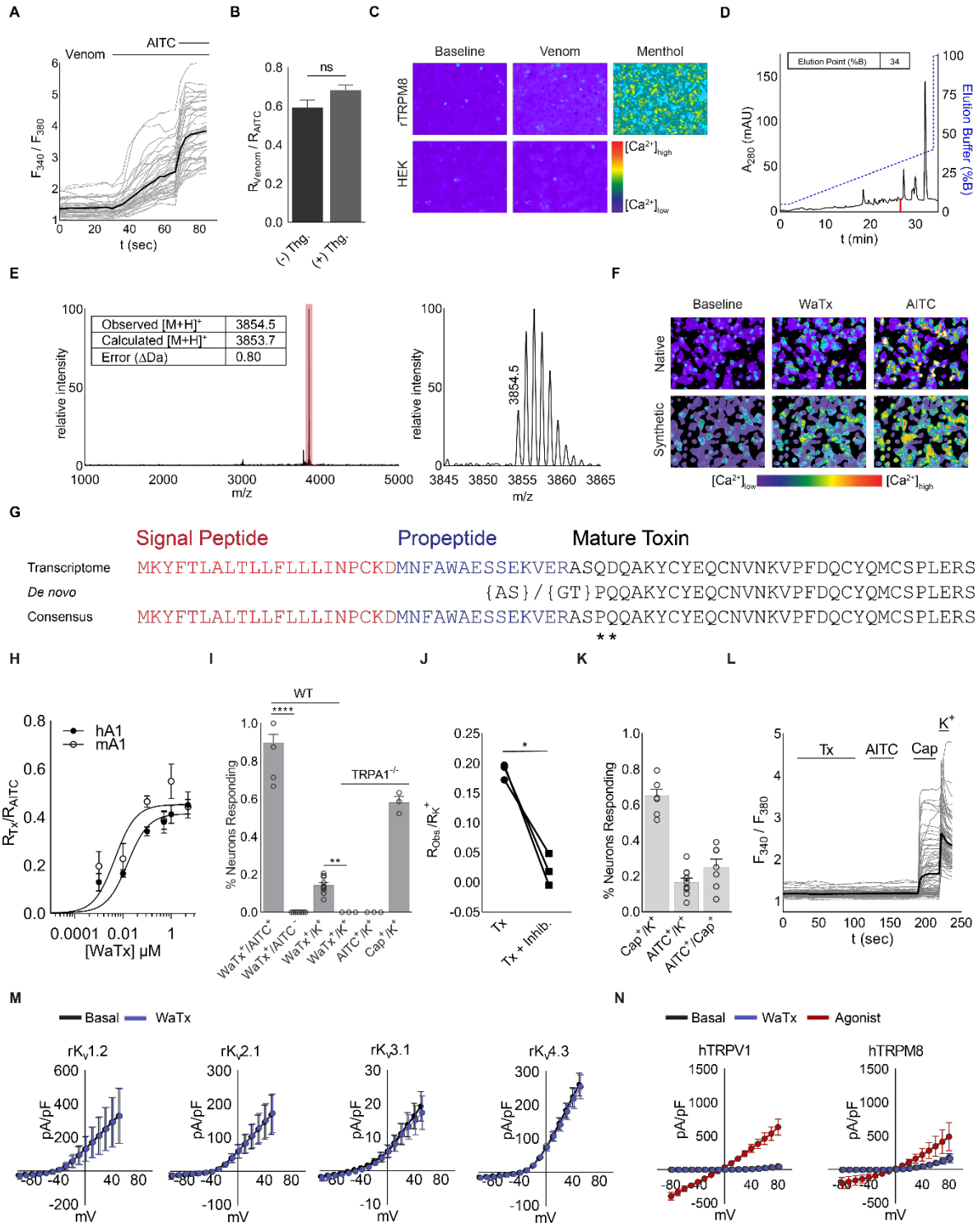


***Figure 2.7 Cloning a selective TRPA1-activating toxin from scorpion venom***

**(A, B)** $Ca^{2+}$-imaging of crude *U. manicatus* venom (~0.1 mg $ml^{-1}$) followed by AITC (333µM) applied to rat TRPA1-expressing HEK cells with and without thapsigargin pretreatment to deplete intracellular $Ca^{2+}$ stores (2 µM, 20 min). Unpaired two-tailed Student's *t*-test. Representing $n = 2$ independent experiments of $n > 50$ cells each.

**(C)** *U. manicatus* venom activity (~0.1 mg $ml^{-1}$) does not activate rat TRPM8- or un-transfected HEK cells. TRPM8 channels revealed by menthol application (333 μM); Representing $n$ = 2 independent experiments of $n$ > 50 cells each.

**(D)** Reverse-phase HPLC chromatogram of ~1 mg *U. manicatus* venom. TRPA1-activating fraction highlighted red.

**(E)** MALDI-ToF MS analysis of the abundant species (left panel, highlighted red) its mono-isotopic mass (right panel, $[M+H]^+$) in the TRPA1-activating fraction. *Inset*: comparison to the WaTx mass determined by *de novo* sequencing of this species (Table 1)

**(F)** Comparison between native (250 nM) and synthetic WaTx (5 μM) activity in HEK cells transfected with human TRPA1.

**(G)** Disambiguation of the N-terminal dipeptide and identification of putative signal- and pro-peptides in a *U. manicatus* venom gland transcriptome (SRX288428) (Sunagar et al., 2013).

**(H)** $Ca^{2+}$-imaging of WaTx dose-response relationship for mouse ($EC_{50}$, 6; 95 % CI 3 - 7 nM) and human (EC50, 16; 95% CI 10 - 24 nM) TRPA1. Data fit by non-linear regression; $n$ > 2 independent experiments of > 50 HEK cells each.

**(I)** Specificity of WaTx (5 μM)-evoked $Ca^{2+}$ transients to the AITC (50 μM)-responsive population of cultured mouse trigeminal sensory neurons. One-way ANOVA with *post-hoc* Holm-Sidak correction for multiple comparisons; $n$ = 10 independent experiments of $n$ > 30 cells each.

**(J)** Inhibition of WaTx (5 μM)-evoked $Ca^{2+}$ influx into cultured mouse trigeminal neurons by the selective TRPA1 inhibitior, A 967079 (10 μM). Paired, two-tailed Student's $t$-test, $n$ = 3.

**(K)** Normal proportions of wild-type cultured mouse trigeminal neurons in response to TRP agonists (1 μM Capsaicin and 50 μM AITC) (Bautista et al., 2006; Caterina et al., 2000; Jordt et al., 2004); $n$=7-11 independent experiments.

**(L)** Absence of WaTx (5 μM) and AITC (50 μM)-evoked $Ca^{2+}$ transients in $TRPA1^{-/-}$ mouse trigeminal neuron cultures. Capsaicin-dose: 5 μM. Representative of $n$ = 3 independent experiments of > 50 cells each.

**(M)** Current-voltage relationships under basal and WaTx-treated conditions for rat $K_v$ channels ($n$=4-6 cells/construct, 1 μM WaTx), and (M) TRP channels ($n$ = 5-6 cells/treatment, 100 nM WaTx; 1 μM Capsaicin or 500 μM Menthol).

All summary data, mean ± SEM.

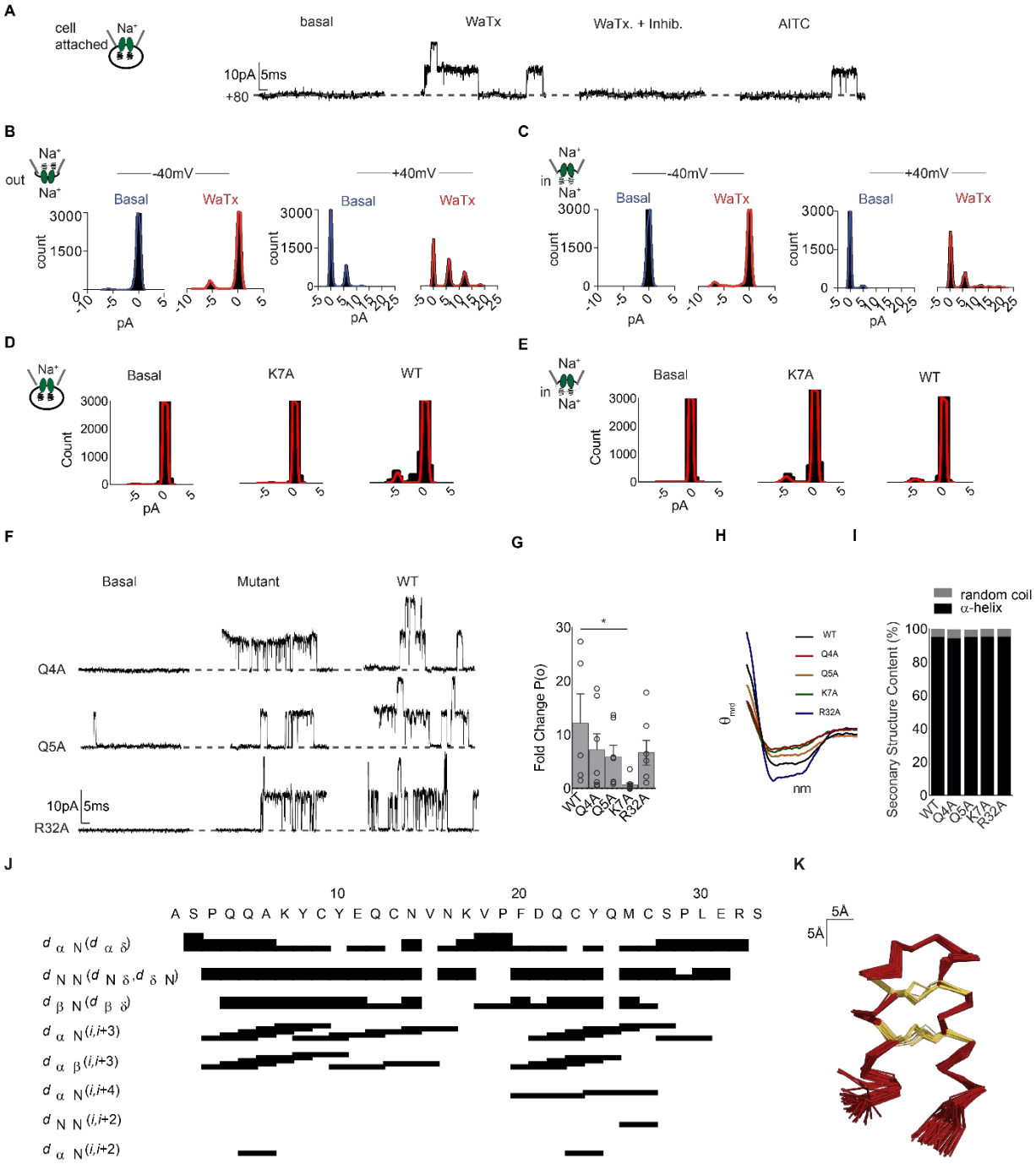


***Figure 2.8 Wild Type and mutant WaTx biophysical properties***

**(A)** Observation of WaTx-evoked TRPA1-activity in cell-attached mode. Treatments: WaTx (100 nM), WaTx + inhibitor (A 967079, 10 μM), and AITC (50 μM). Data represent *n* = 15 HEK cell patches.

**(B, C)** All-points histograms of WaTx-evoked TRPA1 openings in (B)**,** inside-out and (C) outside-out patches from HEK cells. Data fit by nonlinear regression to a sum of multiple gaussians and represent *n* = 10 outside-out and 14 inside-out HEK cell patches.

**(D, E)** All-points histograms comparing the activation of TRPA1 by K7A and WaTx in **(D)** cell-attached and **(E)** inside-out mode; $V_h$ = -80mV. Data fit by nonlinear regression to a sum of multiple gaussians and represent *n* = 5 inside-out and 12 cell-attached HEK cell patches.

**(F)** Cell-attached recordings at 80 mV comparing activity of WaTx mutants to WaTx. Data represent *n* = 5-7 patches/mutant. **(G)** Fold-change in open probability produced by WaTx mutants applied in cell-attached mode. One-Way ANOVA with *post-hoc* Holm-Sidak correction for multiple comparisons; *n* = 5-11 HEK cell patches/mutant.

**(H)** Circular dichroism spectra for WaTx constructs and **(I)** quantification of their secondary structure content; data represent the average of *n* = 3 independent experiments.

**(J)** Chart of NOESY assignments used to generate restraints for WaTx structure calculations.

**(K)** Superimposed 50 best WaTx structures that were selected for water-refinement from 200 calculated structures on the criteria of having the lowest total energy. All-atom RMSD = 0.332.

All summary data, mean ± SEM

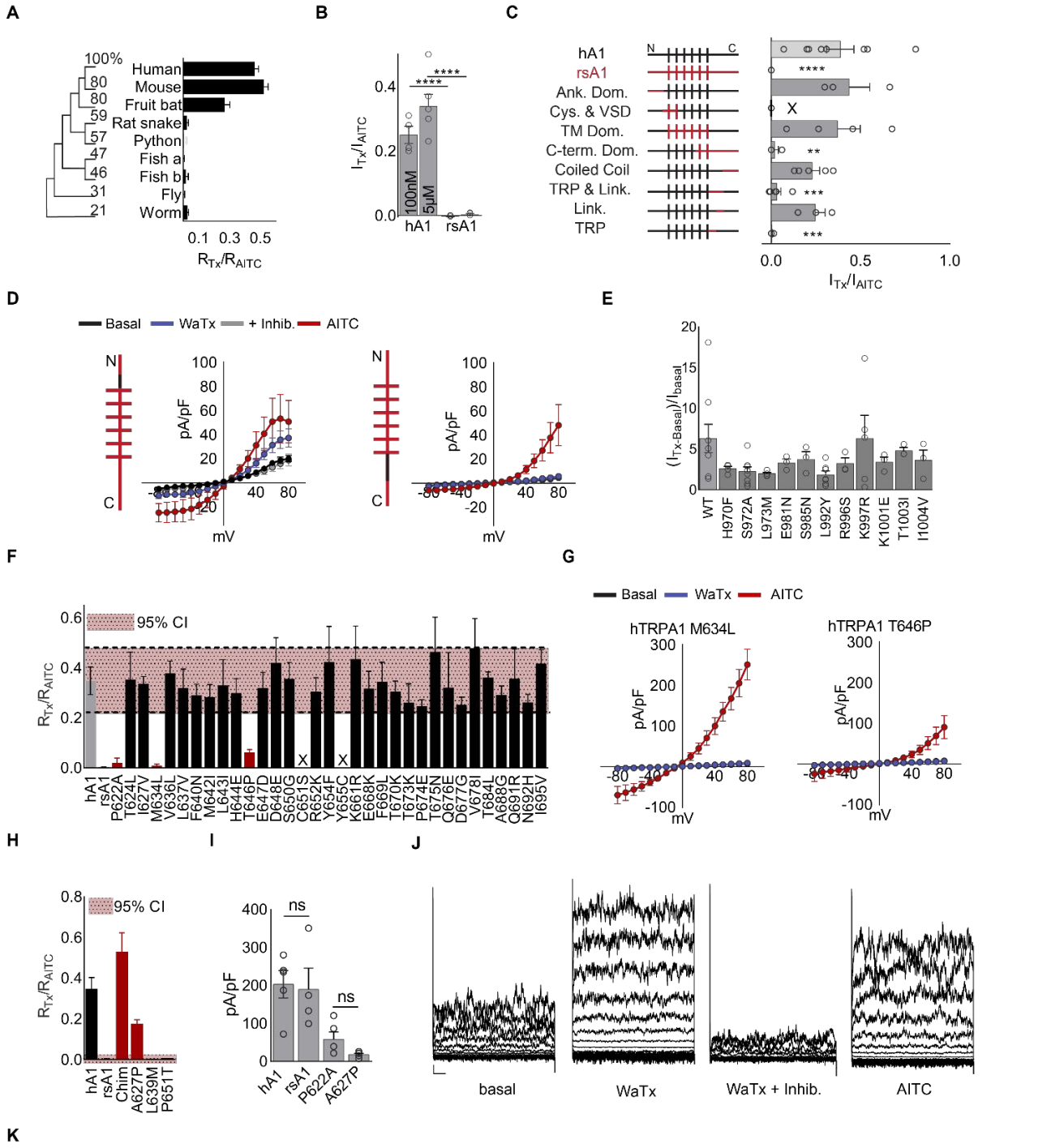
A
100%
80
80
59
57
47
46
31
21
Human
Mouse
Fruit bat
Rat snake
Python
Fish a
Fish b
Fly
Worm
0.1 0.3 0.5
RTx/RAITC
B
ITx/IAITC
0.4
0.2
0.0
****
****
100nM
5μM
hA1
rsA1
C
hA1
rsA1
Ank. Dom.
Cys. & VSD
TM Dom.
C-term. Dom.
Coiled Coil
TRP & Link.
Link.
TRP
N
C
****
X
**
***
***
0.0
0.5
1.0
ITx/IAITC
D
Basal
WaTx
+ Inhib.
AITC
N
C
100
80
60
40
20
pA/pF
40
80
-20
mV
E
20
15
10
5
0
(ITx-Basal)/Ibasal
WT
H970F
S972A
L973M
E981N
S985N
L992Y
R996S
K997R
K1001E
T1003I
I1004V
F
95% CI
0.6
0.4
0.2
0.0
RTx/RAITC
hA1
rsA1
P622A
T624L
I627V
M634L
V636L
L637V
F640N
M642I
L643I
H644E
T646P
E647D
D648E
S650G
C651S
R652K
Y654F
Y655C
K661R
E668K
F669L
T670K
T673K
P674E
T675N
Q676E
D677G
V678I
T684L
A688G
Q691R
N692H
I695V
G
Basal
WaTx
AITC
hTRPA1 M634L
hTRPA1 T646P
300
200
100
pA/pF
-80
-40
40
80
-100
mV
H
95% CI
0.8
0.6
0.4
0.2
0.0
RTx/RAITC
hA1
rsA1
Chim
A627P
L639M
P651T
I
400
300
200
100
0
pA/pF
ns
ns
hA1
rsA1
P622A
A627P
J
basal
WaTx
WaTx + Inhib.
AITC
K
hA1 ¹MKR...LE¹¹¹⁹P
rsA1 ¹MKR...KC¹¹¹³A
Ankyrin ¹MKR...IL⁶⁰⁷H⁶⁰³KRW...LE¹¹¹⁹P
Cys. Link.& VSD ¹MKR...NK⁶²¹C...⁶²⁷AIL...FE⁸⁵⁴N⁸⁵⁰CGI...LE¹¹¹⁹P
TM Dom. ¹MKR...LL⁶⁹⁹N ⁷⁰⁶HPV...IA⁹⁶⁵E⁹⁶⁷VQK...LE¹¹¹⁹P
C-term. Dom. ¹MKR...FE⁸⁵⁵N ⁸⁵⁵YIG...KC¹¹¹³A
Coiled Coil ¹MKR...SL¹⁰⁴¹E ¹⁰⁴⁰LEV...KC¹¹¹³A
TRP & Link. ¹MKR...VQ⁹⁶⁹K⁹⁶⁹FAA...DT¹⁰³⁷T¹⁰⁴⁰LEM...LE¹¹¹⁹P
Link. ¹MKR...KP¹⁰¹¹R¹⁰¹¹YCG...DT¹⁰³⁷T¹⁰⁴⁰LEM...LE¹¹¹⁹P
TRP ¹MKR...DI⁹⁶⁵A⁹⁶⁵EVQ...SI¹⁰⁰³V¹⁰⁵VYP...LE¹¹¹⁹P
TRP ¹MKR...DI⁹⁶⁴A⁹⁶⁶DVQ...DK¹⁰³⁹S¹⁰³⁸LEL...KC¹¹¹³A
Cys. Link ¹MKR...SS⁶²³I⁶¹⁹NKC...EL⁶⁹⁸L⁷⁰⁵SHP...KC¹¹¹³A

***Figure 2.9 Molecular basis for species-selective action of WaTx on TRPA1***

**(A)** Percent identity and phylogeny of TRPA1 orthologs and their response to WaTx, assessed by $Ca^{2+}$-imaging. Treatments: WaTx (5 μM) and AITC (333 μM); *n* = 3 independent experiments of *n* > 50 HEK cells/ortholog/experiment.

**(B)** Rat Snake (rs) TRPA1 is WaTx-insensitive. Whole-cell patch clamp recordings of human (h) and rat snake TRPA1 in response to indicated WaTx treatments. One-Way ANOVA with *post-hoc* Holm-Sidak correction for multiple comparisons; *n*= 4-12 HEK cells/condition.

**(C)** Human-rat snake TRPA1 chimaeras; with comparison of their responses to WaTx (1 μM) and AITC (500 μM) in whole-cell patch clamp experiments. One-Way ANOVA with *post-hoc* Holm-Sidak correction for multiple comparisons; *n* = 3-8 HEK cells/chimaera. Non-functional chimaera denoted, "X."

**(D)** Current-voltage relationships for gain-of function cysteine-rich linker "Cys. Link" (left panel) and loss-of-function "TRP" (right panel) chimaeras. Treatments: WaTx (5 μM), WaTx + inhibitor (HC 030031, 100 μM), and AITC (100 μM), *n* = 4-6 HEK cells/condition.

**(E)** Whole-cell patch-clamp analysis of TRP domain substitutions between human and rat snake TRPA1; *n* = 3-9 HEK cells/construct.

**(F)** Average $Ca^{2+}$-imaging response of positions in the cysteine-rich linker ("Cys. Link.") domain different between hTRPA1 and rsTRPA1. Mutants non-responsive to AITC marked, "X"; hTRPA1 mutants whose activity fell below the 95% CI for the mean of WT hTRPA1 were taken forward for patch-clamp analysis. *N* > 3 independent experiments of >50 HEK cells/experiment/construct.

**(G)** Current-voltage relationships for two hTRPA1 mutants insensitive to WaTx (treatments: 1 μM WaTx, 100 μM AITC) *n* = 3 HEK cells/construct.

**(H)** $Ca^{2+}$-imaging of rsTRPA1 gain-of-function chimaeras and point-mutants. Constructs whose activities exceeded the 95% CI for WT rsTRPA1 were taken forward for further analysis; *n* > *3* independent experiments of *n* > 50 HEK cells/experiment/construct.

**(I)** Whole-cell patch-clamp analysis of expression levels between TRPA1 constructs tested for WaTx binding by BLI, as revealed by a saturating dose of AITC (100 μM). One-Way ANOVA with *post-hoc* Holm-Sidak correction for multiple comparisons, *n* = 4-5 HEK cells/construct.

**(J)** Representative whole-cell recordings of rsTRAP1 A627P in response to WaTx (5 μM), WaTx + Inhibitor (100μM, HC 030031), and AITC (100 μM); data represent *n* = 5 HEK cells. Scale bar: x, 50 msec.; y, 50 pA.

**(K)** Sequences of TRPA1 chimaeras

All summary data, mean ± SEM.

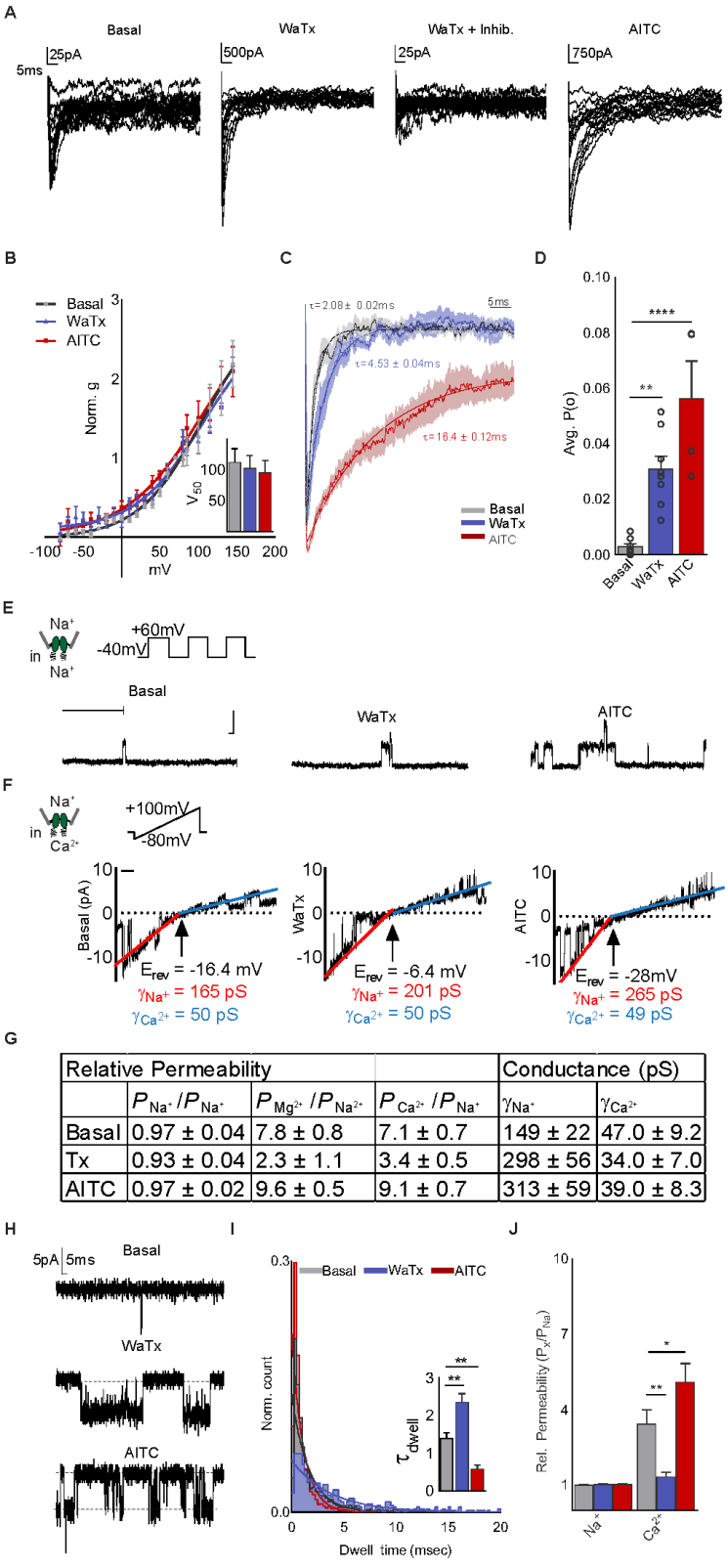


| Relative Permeability | | | | Conductance (pS) | |
|---|---|---|---|---|---|
| | $P_{Na^+}/P_{Na^+}$ | $P_{Mg^{2+}}/P_{Na^+}$ | $P_{Ca^{2+}}/P_{Na^+}$ | $\gamma_{Na^+}$ | $\gamma_{Ca^{2+}}$ |
| Basal | 0.97 ± 0.04 | 7.8 ± 0.8 | 7.1 ± 0.7 | 149 ± 22 | 47.0 ± 9.2 |
| Tx | 0.93 ± 0.04 | 2.3 ± 1.1 | 3.4 ± 0.5 | 298 ± 56 | 34.0 ± 7.0 |
| AITC | 0.97 ± 0.02 | 9.6 ± 0.5 | 9.1 ± 0.7 | 313 ± 59 | 39.0 ± 8.3 |

***Figure 2.10 Biophysical properties of WaTx-evoked currents***

**(A)** TRPA1 tail currents **(B)**, tail-current derived G-V relationships; and **(C)** normalized, scaled, and averaged tail-currents from experiments shown in Figure 1D. Treatments: WaTx (1μM), WaTx + inhibitor (10mM A 967079), AITC (100μM). Data were normalized within-groups to the amplitude at 70 mV, then fit by non-linear regression to the Boltzmann equation to derive the $V_{50}$ (inset). One-way ANOVA with *post-hoc* Holm-Sidak correction for multiple comparisons; *n* = 8-22 HEK cells/treatment.

**(D)** WaTx and AITC each increase TRPA1 open-probability (P(o)) in inside-out patches. Treatments: WaTx (100 nM), and AITC (10 μM) . One-Way ANOVA with *post-hoc* Holm Sidak correction for multiple comparisons; *n* = 4-8 HEK cell patches/treatment.

**(E)** Protocol and representative example traces of latency to first opening experiments. Treatments: basal, WaTx (100 nM), and AITC (10 μM) application. Scale bar: x, 40 msec.; y, 5pA; *n* = 13-14 inside-out HEK cell patches/treatment.

**(F)** Liquid-junction potential corrected reversal potential ($E_{rev}$) changes in TRPA1-expressing inside-out patches in the presence of $Ca^{2+}$ in the bath solution under basal, WaTx (100 nM), and AITC (10 μM) conditions. We determined the conductance for each ion by the slope conductance method, fitting by linear regression ($r^2 = 1$). Scale bar, 50 msec.; data represent *n* = 3-7 inside-out HEK cell patches/treatment.

**(G)** Summary of permeability ratios and conductances shown in Figure 4F. Conductance values for $Ca^{2+}$ were determined under bi-ionic conditions with $Na^+$ in the pipette solution and $Ca^{2+}$ in the bath, to avoid $Ca^{2+}$-mediated channel desensitization.

**(H, I)** Inside-out HEK cell patch recordings ($V_h$ = -40 mV) of spontaneous, WaTx (100 nM) or AITC (10 μM)-evoked mouse TRPA1 openings, quantified with respect to **(B),** dwell time (*n* = 4 - 5 patches/treatment). One-Way ANOVA with *post-hoc* Holm-Sidak correction for multiple comparisons.

**(J)** Murine TRPA1 ionic selectivity and conductance for spontaneous, WaTx (100 nM)- or AITC (50 μM)-evoked openings (*n* = 5 HEK cell patches/condition). Two-way ANOVA with *post-hoc* Holm-Sidak correction.

All summary data, mean ± SEM.

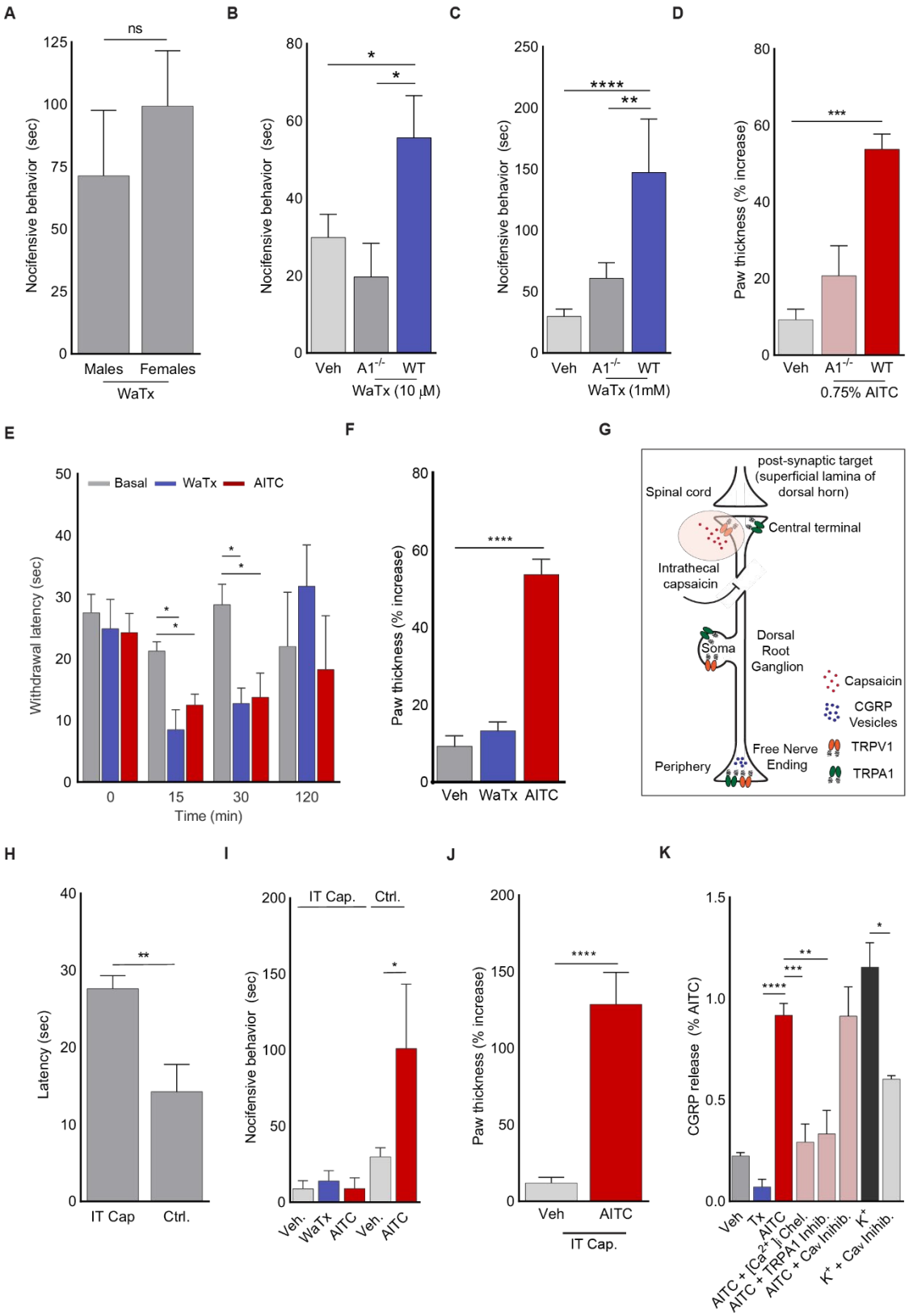


***Figure 2.11 Behavioral parameters of WaTx administration***

**(A)** No detectable difference between nocifensive response to WaTx administration (100 μM) in male and female mice. Unpaired, two-tailed Student's *t*-test; *n* = 5-7 mice/group.

**(B, C)** Dose-dependence of nocifensive response to WaTx administration. One-Way ANOVA with *post-hoc* Holm-Sidak correction for multiple comparisons; *n*= 4-20 mice/group.

**(D)** TRPA1-dependence of local edema in response to AITC administration. One-Way ANOVA with *post-hoc* Holm-Sidak correction for multiple comparisons; *n* = 4 mice/group.

**(E)** Measurements of thermal hypersensitivity after WaTx (100 μM), or AITC (0.75% v/v) administration. One-Way ANOVA with *post-hoc* Holm-Sidak correction for multiple comparisons; *n* = 4 mice/treatment.

**(F)** Quantification of paw edema in mice after WaTx (100nM) or AITC (0.75% v/v in mineral oil) injection. One-way ANOVA with *post-hoc* Holm-Sidak correction for multiple comparisons; *n* = 4 mice/treatment.

**(G)** Schematic of ablation of central terminals of c-fiber nociceptors by intrathecal capsaicin injection

**(H)** Hotplate test confirming absences of nocifensive response to noxious heat in IT Capsaicin-ablated vs. un-ablated mice. Unpaired, two-tailed Student's *t*-test*; n* = 8 mice/group.

**(I)** Absence of nocifensive behavior in IT Capsaicin-ablated mice compared to controls. Treatments: intraplantar injection of vehicle, WaTx (100 μM), or AITC (0.75% v/v). One-Way ANOVA with *post-hoc* Holm-Sidak correction for multiple comparisons; *n* = 3-20 mice/group.

**(J)** Persistence of local edema after AITC (0.75% v/v) administration in IT Capsaicin-ablated mice. Unpaired, two-tailed Student's *t*-test*; n* = 8 mice/group.

**(K)** ELISA measurements of CGRP from cultured neonatal rat trigeminal ganglia. Treatments: WaTx (10μM) AITC (100μM)), intracellular $Ca^{2+}$ chelator (1 mM, EGTA-AM), TRPA1-inhibitor (10 μM, A 967079), $Ca_v$ inhibitor cocktail (Mibefradil, 10 μM; Nifedipine, 10 μM; ω-conotoxin GVIA, 100 nM), or $K^+$ (150 mM). One-Way ANOVA with *post-hoc* Holm-Sidak correction for multiple comparisons (left panel); *n* = 6-18 treatments/condition.

All summary data, mean ± SEM.

**Table 2.1** Summary of WaTx fragment ions detected in ion trap collision-induced dissociation (CID) or beam-type Higher-energy C-trap dissociation (HCD) spectra of partially cysteine carbamidomethylated ($C^{AM}$) m/z 1007.9457 ($4^+$) and assigned in the manual de novo sequencing process. We measured all masses in the Orbitrap.

| method | b | $b^{+2}$ | detected | | detected | y | $y^{+2}$ | method |
|---|---|---|---|---|---|---|---|---|
| | --- | --- | | **A** | | --- | --- | |
| HCD | 159.0764 | --- | 159.9769 | **S** | | 3957.7121 | 1979.3597 | |
| HCD | 256.1292 | --- | 256.1298 | **P** | 1290.9012(3+);968.4276(4+) | 3870.6801 | 1935.8437 | CID |
| HCD | 384.1878 | --- | 384.1890 | **Q** | | 3773.6274 | 1887.3173 | |
| | 512.2463 | --- | 512.2478 | **Q** | | 3645.5688 | 1823.2880 | |
| | 583.2835 | --- | 583.2851 | **A** | 1173.1779(3+) | 3517.5102 | 1759.2587 | CID |
| both | 711.3784 | 356.1928 | 711.3808 | **K** | | 3446.4731 | 1723.7402 | |
| HCD | 874.4417 | 437.7245 | 874.4445 | **Y** | | 3318.3781 | 1659.6927 | |
| | 1034.4724 | 517.7398 | | **$C^{AM}$** | 1578.6184[1] | 3155.3148 | 1578.1610 | |
| both | 1197.5357 | 599.2715 | 1197.5382 | **Y** | | 2995.2841 | 1498.1457 | |
| both | 1326.5783 | 663.7928 | 1326.5819; 663.7944 | **E** | | 2832.2208 | 1416.6140 | |
| both | 1454.6369 | 727.8221 | 1454.6404; 727.8242 | **Q** | 1352.0967; 901.7330(3+) | 2703.1782 | 1352.0927 | CID |
| both | 1614.6675 | 807.8374 | 807.8394 | **$C^{AM}$** | 1288.0667 | 2575.1196 | 1288.0635 | both |
| CID | 1728.7105 | 864.8589 | 864.8613 | **N** | | 2415.0890 | 1208.0481 | |
| both | 1827.7789 | 914.3931 | 914.3953 | **V** | 1151.0287 | 2301.0461 | 1151.0267 | CID |
| both | 1941.8218 | 971.4145 | 971.4173 | **N** | 1101.4950 | 2201.9777 | 1101.4925 | both |
| both | 2069.9168 | 1035.4620 | 1035.4635 | **K** | 1044.4753 | 2087.9347 | 1044.4710 | both |
| both | 2168.9852 | 1084.9962 | 1984.9987 | **V** | | 1959.8398 | 980.4235 | |
| | 2266.0379 | 1133.5226 | | **P** | 1860.7755; 930.8919 | 1860.7714 | 930.8893 | both |
| both | 2413.1064 | 1207.0568 | 1207.0595 | **F** | | 1763.7186 | 882.3629 | |
| both | 2528.1333 | 1264.5703 | 1264.5737 | **D** | 1616.6542; 808.8302 | 1616.6502 | 808.8287 | CID |
| both | 2656.1919 | 1328.5996 | 1328.6040 | **Q** | 751.3171 | 1501.6232 | 751.3153 | both |
| both | 2816.2225 | 1408.6149 | 1408.6191 | **$C^{AM}$** | 1373.5683; 687.2877 | 1373.5647 | 687.2860 | both |
| CID | 2979.2859 | 1490.1466 | 1490.1507 | **Y** | 1213.5372; 607.2721 | 1213.5340 | 607.2706 | half each |
| CID | 3107.3444 | 1554.1759 | 1554.1780 | **Q** | 1050.4731; 525.7402 | 1050.4707 | 525.7390 | both |
| CID | 3238.3849 | 1619.6961 | 1080.1356(3+) | **M** | 944.4146 | 922.4121 | 461.7097 | both |
| CID | 3341.3941 | 1671.2007 | 1114.4717(3+) | **C** | 791.3736 | 791.3716 | 396.1894 | both |
| CID | 3428.4261 | 1714.7167 | 1714.7219 | **S** | 688.3641 | 688.3624 | 344.6849 | both |
| CID | 3525.4789 | 1763.2431 | 1175.8357(3+) | **P** | 601.3318 | 601.3304 | 301.1688 | both |
| CID | 3638.5630 | 1819.7851 | 1213.5343(3+) | **L** | 504.2792 | 504.2776 | 252.6425 | both |
| CID | 3767.6056 | 1884.3064 | 1256.5428(3+) | **E** | 391.1947 | 391.1936 | 196.1004 | both |
| CID | 3923.7067 | 1962.3570 | 981.684(4+) | **R** | 262.1518 | 262.1510 | 131.5791 | HCD |
| | --- | --- | | **S** | | 106.0499 | --- | |

[1]Single isotope

***Table 2.2*** **NMR data collection and refinement statistics for WaTx.**

| **Resonance assignments**[1] | |
|---|---|
| *[$^1$H,$^1$H] NOESY (10% $D_2O$)* | |
| Backbone | 29/30 (97%) |
| Side chain | 134/138 (97%) |
| *[$^1$H,$^1$H] NOESY (100% $D_2O$)* | |
| Backbone | 0/30 (0%) |
| Side chain | 121/138 (88%) |
| *[$^1$H, $^{13}$C ] HSQC (100% $D_2O$)* | |
| Backbone | 27/33 (82%) |
| Side chain | 72/90 (80%) |
| **Restraints**[2] | |
| Total NOE constraints | 538 |
| Intraresidue (i=j) | 275 |
| Sequential (\|i=j\|=1) | 125 |
| Medium range (1<\|i=j\|<5) | 91 |
| Long range (1<\|i=j\|≥5) | 47 |
| Dihedral | 58 |
| Disulfide | 2 |
| **Residual restraint violations**[2] **(Mean ± SD)** | |
| *Avg. distance violation / structure (*Å) | 0.10 ± 0.30 |
| *Avg. dihedral violation / structure (°)* | 0.53 ± 1.9 |
| **Model quality** | |
| RMSD all atoms[1] (Å) | 0.332 |
| RMSD bond lengths[2] (Å) | 0.005 |
| RMSD bond angles[2] (°) | 0.7 |
| Number of close contacts[3] | 0 |
| **Ramachandran statistics**[2] **(%)** | |
| Most favored | 84 |
| Additionally allowed | 12 |
| Generously allowed | 4 |
| Disallowed | 0 |
| **Model contents** | |
| Total no. of residues | 33 |
| Total no. models calculated | 200 |
| Total no. models deposited | 50 |
| PDB/BMRB code | 6OFA/30597 |

[1]Determined with CCPN Analysis

[2]Calculated with PSVS; average distance violations were calculated using sum over $r^2$

[3]Defined as being within 1.6Å for Hydrogen atoms

**Acknowledgements**

We thank all members of the Julius lab for provocative discussions, especially N. Bellono for guidance and advice with patch-clamp electrophysiology and D. Leitch for guidance with interpretation of transcriptomic data. We also recognize J. Poblete and J. Braz for expert technical assistance with mouse experiments. Finally, we are grateful to L.Y. Jan, R.A. Nicoll, D. Cohn, and W.J. Tang for their critical reading of the manuscript. This work was supported by an NSF Graduate Research Fellowship (No. 1650113 to J.V.L.K), a UCSF Chuan-Lyu Discovery Fellowship (J.V.L.K), and grants from the NIH (R37 NS065071 and R35 NS105038 to D.J; and T32 GM007449 to J.V.L.K).

**References**

Andersson, D.A., Gentry, C., Moss, S., and Bevan, S. (2008). Transient receptor potential A1 is a sensory receptor for multiple products of oxidative stress. The Journal of neuroscience : the official journal of the Society for Neuroscience *28*, 2485-2494.

Bahia, P.K., Parks, T.A., Stanford, K.R., Mitchell, D.A., Varma, S., Stevens, S.M., Jr., and Taylor-Clark, T.E. (2016). The exceptionally high reactivity of Cys 621 is critical for electrophilic activation of the sensory nerve ion channel TRPA1. The Journal of general physiology *147*, 451-465.

Baker, N.A., Sept, D., Joseph, S., Holst, M.J., and McCammon, J.A. (2001). Electrostatics of nanosystems: application to microtubules and the ribosome. Proceedings of the National Academy of Sciences of the United States of America *98*, 10037-10041.

Bandell, M., Story, G.M., Hwang, S.W., Viswanath, V., Eid, S.R., Petrus, M.J., Earley, T.J., and Patapoutian, A. (2004). Noxious cold ion channel TRPA1 is activated by pungent compounds and bradykinin. Neuron *41*, 849-857.

Banzawa, N., Saito, S., Imagawa, T., Kashio, M., Takahashi, K., Tominaga, M., and Ohta, T. (2014). Molecular Basis Determining Inhibition/Activation of Nociceptive Receptor TRPA1 Protein: A Single Amino Acid Dictates Species-specific actions of the most potent mammalian TRPA1 Antagonist. Journal of Biological Chemistry *289*, 31927-31939.

Basbaum, A.I., Bautista, D.M., Scherrer, G., and Julius, D. (2009). Cellular and molecular mechanisms of pain. Cell *139*, 267-284.

Bautista, D.M., Jordt, S.E., Nikai, T., Tsuruda, P.R., Read, A.J., Poblete, J., Yamoah, E.N., Basbaum, A.I., and Julius, D. (2006). TRPA1 mediates the inflammatory actions of environmental irritants and proalgesic agents. Cell *124*, 1269-1282.

Bautista, D.M., Pellegrino, M., and Tsunozaki, M. (2013). TRPA1: A gatekeeper for inflammation. Annual review of physiology *75*, 181-200.

Bechara, C., and Sagan, S. (2013). Cell-penetrating peptides: 20 years later, where do we stand? FEBS letters *587*, 1693-1702.

Bhattacharya, A., Tejero, R., and Montelione, G.T. (2007). Evaluating protein structures determined by structural genomics consortia. Proteins *66*, 778-795.

Bobkov, Y.V., Corey, E.A., and Ache, B.W. (2011). The pore properties of human nociceptor channel TRPA1 evaluated in single channel recordings. Biochimica et biophysica acta *1808*, 1120-1128.

Bohlen, C.J., Chesler, A.T., Sharif-Naeini, R., Medzihradszky, K.F., Zhou, S., King, D., Sanchez, E.E., Burlingame, A.L., Basbaum, A.I., and Julius, D. (2011). A heteromeric Texas coral snake toxin targets acid-sensing ion channels to produce pain. Nature *479*, 410-414.

Bohlen, C.J., and Julius, D. (2012). Receptor-targeting mechanisms of pain-causing toxins: How ow? Toxicon : official journal of the International Society on Toxinology *60*, 254-264.

Bohlen, C.J., Priel, A., Zhou, S., King, D., Siemens, J., and Julius, D. (2010). A bivalent tarantula toxin activates the capsaicin receptor, TRPV1, by targeting the outer pore domain. Cell *141*, 834-845.

Bosmans, F., and Tytgat, J. (2007). Voltage-gated sodium channel modulation by scorpion alpha-toxins. Toxicon : official journal of the International Society on Toxinology *49*, 142-158.

Bradford, M.M. (1976). A rapid and sensitive method for the quantitation of microgram quantities of protein utilizing the principle of protein-dye binding. Analytical biochemistry *72*, 248-254.

Cao, E., Liao, M., Cheng, Y., and Julius, D. (2013). TRPV1 structures in distinct conformations reveal activation mechanisms. Nature *504*, 113-118.

Caterina, M.J., Leffler, A., Malmberg, A.B., Martin, W.J., Trafton, J., Petersen-Zeitz, K.R., Koltzenburg, M., Basbaum, A.I., and Julius, D. (2000). Impaired Nociception and Pain Sensation in Mice Lacking the Capsaicin Receptor. Science *288*, 306.

Caterina, M.J., Schumacher, M.A., Tominaga, M., Rosen, T.A., Levine, J.D., and Julius, D. (1997). The capsaicin receptor: a heat-activated ion channel in the pain pathway. Nature *389*, 816-824.

Cavanaugh, D.J., Lee, H., Lo, L., Shields, S.D., Zylka, M.J., Basbaum, A.I., and Anderson, D.J. (2009). Distinct subsets of unmyelinated primary sensory fibers mediate behavioral responses to noxious thermal and mechanical stimuli. Proceedings of the National Academy of Sciences of the United States of America *106*, 9075-9080.

Chaplan, S.R., Bach, F.W., Pogrel, J.W., Chung, J.M., and Yaksh, T.L. (1994). Quantitative assessment of tactile allodynia in the rat paw. Journal of Neuroscience Methods *53*, 55-63.

Chen, J., Joshi, S.K., DiDomenico, S., Perner, R.J., Mikusa, J.P., Gauvin, D.M., Segreti, J.A., Han, P., Zhang, X.F., Niforatos, W.*, et al.* (2011). Selective blockade of TRPA1 channel attenuates

pathological pain without altering noxious cold sensation or body temperature regulation. Pain *152*, 1165-1172.

Cheung, M.S., Maguire, M.L., Stevens, T.J., and Broadhurst, R.W. (2010). DANGLE: A Bayesian inferential method for predicting protein backbone dihedral angles and secondary structure. Journal of magnetic resonance. *202*, 223-233.

Chung, M.K., Guler, A.D., and Caterina, M.J. (2008). TRPV1 shows dynamic ionic selectivity during agonist stimulation. Nature neuroscience *11*, 555-564.

Clapham, D.E. (2003). TRP channels as cellular sensors. Nature *426*, 517-524.

Cordero-Morales, J.F., Gracheva, E.O., and Julius, D. (2011). Cytoplasmic ankyrin repeats of transient receptor potential A1 (TRPA1) dictate sensitivity to thermal and chemical stimuli. Proceedings of the National Academy of Sciences of the United States of America *108*, E1184-E1191.

Derossi, D., Joliot, A.H., Chassaing, G., and Prochiantz, A. (1994). The third helix of the Antennapedia homeodomain translocates through biological membranes. The Journal of biological chemistry *269*, 10444-10450.

Emrick, J.J., Mathur, A., Wei, J., Gracheva, E.O., Gronert, K., Rosenblum, M.D., and Julius, D. (2018). Tissue-specific contributions of *Tmem79* to atopic dermatitis and mast cell-mediated histaminergic itch. Proceedings of the National Academy of Sciences *115*, E12091.

Felder, C.E., Prilusky, J., Silman, I., and Sussman, J.L. (2007). A server and database for dipole moments of proteins. Nucleic acids research *35*, W512-W521.

Frankel, A.D., and Pabo, C.O. (1988). Cellular uptake of the tat protein from human immunodeficiency virus. Cell *55*, 1189-1193.

Gao, Y., Cao, E., Julius, D., and Cheng, Y. (2016). TRPV1 structures in nanodiscs reveal mechanisms of ligand and lipid action. Nature *534*, 347-351.

Gracheva, E.O., Cordero-Morales, J.F., González-Carcacía, J.A., Ingolia, N.T., Manno, C., Aranguren, C.I., Weissman, J.S., and Julius, D. (2011). Ganglion-specific splicing of TRPV1 underlies infrared sensation in vampire bats. Nature *476*, 88.

Gracheva, E.O., Ingolia, N.T., Kelly, Y.M., Cordero-Morales, J.F., Hollopeter, G., Chesler, A.T., Sanchez, E.E., Perez, J.C., Weissman, J.S., and Julius, D. (2010). Molecular basis of infrared detection by snakes. Nature *464*, 1006-1011.

Guidotti, G., Brambilla, L., and Rossi, D. (2017). Cell-Penetrating Peptides: From Basic Research to Clinics. Trends in Pharmacological Sciences *38*, 406-424.

Heitz, F., Morris, M.C., and Divita, G. (2009). Twenty years of cell-penetrating peptides: from molecular mechanisms to therapeutics. Br J Pharmacol *157*, 195-206.

Hille, B. (2001). Ion channels of excitable membranes (Sinauer).

Hinman, A., Chuang, H.H., Bautista, D.M., and Julius, D. (2006). TRP channel activation by reversible covalent modification. Proceedings of the National Academy of Sciences of the United States of America *103*, 19564-19568.

Horn, R. (1991). Diffusion of nystatin in plasma membrane is inhibited by a glass-membrane seal. Biophysical journal *60*, 329-333.

Joliot, A., Pernelle, C., Deagostini-Bazin, H., and Prochiantz, A. (1991). Antennapedia homeobox peptide regulates neural morphogenesis. Proceedings of the National Academy of Sciences of the United States of America *88*, 1864-1868.

Joliot, A., and Prochiantz, A. (2004). Transduction peptides: from technology to physiology. Nat Cell Biol *6*, 189-196.

Jordt, S.E., Bautista, D.M., Chuang, H.H., McKemy, D.D., Zygmunt, P.M., Hogestatt, E.D., Meng, I.D., and Julius, D. (2004). Mustard oils and cannabinoids excite sensory nerve fibres through the TRP channel ANKTM1. Nature *427*, 260-265.

Julius, D. (2013). TRP channels and pain. Annual review of cell and developmental biology *29*, 355-384.

Jung, H.J., Lee, J.Y., Kim, S.H., Eu, Y.-J., Shin, S.Y., Milescu, M., Swartz, K.J., and Kim, J.I. (2005). Solution Structure and Lipid Membrane Partitioning of VSTx1, an Inhibitor of the KvAP Potassium Channel. Biochemistry *44*, 6015-6023.

Kalia, J., Milescu, M., Salvatierra, J., Wagner, J., Klint, J.K., King, G.F., Olivera, B.M., and Bosmans, F. (2015). From foe to friend: using animal toxins to investigate ion channel function. Journal of molecular biology *427*, 158-175.

Kang, K., Pulver, S.R., Panzano, V.C., Chang, E.C., Griffith, L.C., Theobald, D.L., and Garrity, P.A. (2010). Analysis of Drosophila TRPA1 reveals an ancient origin for human chemical nociception. Nature *464*, 597-600.

Karashima, Y., Damann, N., Prenen, J., Talavera, K., Segal, A., Voets, T., and Nilius, B. (2007). Bimodal Action of Menthol on the Transient Receptor Potential Channel TRPA1. The Journal of Neuroscience *27*, 9874.

Karashima, Y., Prenen, J., Talavera, K., Janssens, A., Voets, T., and Nilius, B. (2010). Agonist-induced changes in Ca(2+) permeation through the nociceptor cation channel TRPA1. Biophysical journal *98*, 773-783.

Kauffman, W.B., Fuselier, T., He, J., and Wimley, W.C. (2015). Mechanism Matters: A Taxonomy of Cell Penetrating Peptides. Trends in biochemical sciences *40*, 749-764.

Kindt, K.S., Viswanath, V., Macpherson, L., Quast, K., Hu, H., Patapoutian, A., and Schafer, W.R. (2007). Caenorhabditis elegans TRPA-1 functions in mechanosensation. Nature neuroscience *10*, 568-577.

King, G.F., Gentz, M.C., Escoubas, P., and Nicholson, G.M. (2008). A rational nomenclature for naming peptide toxins from spiders and other venomous animals. Toxicon : official journal of the International Society on Toxinology *52*, 264-276.

King, G.F., and Hardy, M.C. (2013). Spider-venom peptides: structure, pharmacology, and potential for control of insect pests. Annual review of entomology *58*, 475-496.

Latorre, R., Zaelzer, C., and Brauchi, S. (2009). Structure-functional intimacies of transient receptor potential channels. Quarterly reviews of biophysics *42*, 201-246.

Lee, S.Y., and MacKinnon, R. (2004). A membrane-access mechanism of ion channel inhibition by voltage sensor toxins from spider venom. Nature *430*, 232-235.

Liao, M., Cao, E., Julius, D., and Cheng, Y. (2013). Structure of the TRPV1 ion channel determined by electron cryo-microscopy. Nature *504*, 107-112.

Lipscombe, D., Kongsamut, S., and Tsien, R.W. (1989). Alpha-adrenergic inhibition of sympathetic neurotransmitter release mediated by modulation of N-type calcium-channel gating. Nature *340*, 639-642.

Macpherson, L.J., Dubin, A.E., Evans, M.J., Marr, F., Schultz, P.G., Cravatt, B.F., and Patapoutian, A. (2007). Noxious compounds activate TRPA1 ion channels through covalent modification of cysteines. Nature *445*, 541-545.

Maricq, A.V., Peterson, A.S., Brake, A.J., Myers, R.M., and Julius, D. (1991). Primary structure and functional expression of the 5HT3 receptor, a serotonin-gated ion channel. Science *254*, 432-437.

McKemy, D.D., Neuhausser, W.M., and Julius, D. (2002). Identification of a cold receptor reveals a general role for TRP channels in thermosensation. Nature *416*, 52-58.

McNamara, C.R., Mandel-Brehm, J., Bautista, D.M., Siemens, J., Deranian, K.L., Zhao, M., Hayward, N.J., Chong, J.A., Julius, D., Moran, M.M*., et al.* (2007). TRPA1 mediates formalin-induced pain. Proceedings of the National Academy of Sciences of the United States of America *104*, 13525-13530.

Mihailescu, M., Krepkiy, D., Milescu, M., Gawrisch, K., Swartz, K.J., and White, S. (2014). Structural interactions of a voltage sensor toxin with lipid membranes. Proceedings of the National Academy of Sciences *111*, E5463.

Miles, A.J., and Wallace, B.A. (2018). CDtoolX, a downloadable software package for processing and analyses of circular dichroism spectroscopic data. Protein Science *27*, 1717-1722.

Moran, M.M. (2018). TRP Channels as Potential Drug Targets. Annual Review of Pharmacology and Toxicology *58*, 309-330.

Nagata, K., Duggan, A., Kumar, G., and Garcia-Anoveros, J. (2005). Nociceptor and hair cell transducer properties of TRPA1, a channel for pain and hearing. J Neurosci *25*, 4052-4061.

Nicoll, R.A., Eccles, J.C., Oshima, T., and Rubia, F. (1975). Prolongation of hippocampal inhibitory postsynaptic potentials by barbiturates. Nature *258*, 625.

Nilius, B., Prenen, J., and Owsianik, G. (2011). Irritating channels: the case of TRPA1. The Journal of physiology *589*, 1543-1549.

Osteen, J.D., Herzig, V., Gilchrist, J., Emrick, J.J., Zhang, C., Wang, X., Castro, J., Garcia-Caraballo, S., Grundy, L., Rychkov, G.Y.*, et al.* (2016). Selective spider toxins reveal a role for the Nav1.1 channel in mechanical pain. Nature *534*, 494-499.

Palovcak, E., Delemotte, L., Klein, M.L., and Carnevale, V. (2015). Comparative sequence analysis suggests a conserved gating mechanism for TRP channels. The Journal of general physiology *146*, 37-50.

Paulsen, C.E., Armache, J.P., Gao, Y., Cheng, Y., and Julius, D. (2015). Structure of the TRPA1 ion channel suggests regulatory mechanisms. Nature *520*, 511-517.

Peier, A.M., Moqrich, A., Hergarden, A.C., Reeve, A.J., Andersson, D.A., Story, G.M., Earley, T.J., Dragoni, I., McIntyre, P., Bevan, S.*, et al.* (2002). A TRP channel that senses cold stimuli and menthol. Cell *108*, 705-715.

Prober, D.A., Zimmerman, S., Myers, B.R., McDermott, B.M., Kim, S.-H., Caron, S., Rihel, J., Solnica-Krezel, L., Julius, D., Hudspeth, A.J.*, et al.* (2008). Zebrafish TRPA1 Channels Are Required for Chemosensation But Not for Thermosensation or Mechanosensory Hair Cell Function. The Journal of Neuroscience *28*, 10102.

Quintero-Hernandez, V., Jimenez-Vargas, J.M., Gurrola, G.B., Valdivia, H.H., and Possani, L.D. (2013). Scorpion venom components that affect ion-channels function. Toxicon : official journal of the International Society on Toxinology *76*, 328-342.

Rieping, W., Habeck, M., Bardiaux, B., Bernard, A., Malliavin, T.E., and Nilges, M. (2007). ARIA2: automated NOE assignment and data integration in NMR structure calculation. Bioinformatics (Oxford, England) *23*, 381-382.

Sakmann, B., and Neher, E. (2009). Single-channel recording (Springer).

Shi, G., Kleinklaus, A.K., Marrion, N.V., and Trimmer, J.S. (1994). Properties of Kv2.1 K+ channels expressed in transfected mammalian cells. The Journal of biological chemistry *269*, 23204-23211.

Siemens, J., Zhou, S., Piskorowski, R., Nikai, T., Lumpkin, E.A., Basbaum, A.I., King, D., and Julius, D. (2006). Spider toxins activate the capsaicin receptor to produce inflammatory pain. Nature *444*, 208-212.

Silva, P.I., Jr., Daffre, S., and Bulet, P. (2000). Isolation and characterization of gomesin, an 18-residue cysteine-rich defense peptide from the spider Acanthoscurria gomesiana hemocytes with sequence similarities to horseshoe crab antimicrobial peptides of the tachyplesin family. The Journal of biological chemistry *275*, 33464-33470.

Srinivasan, K.N., Sivaraja, V., Huys, I., Sasaki, T., Cheng, B., Kumar, T.K., Sato, K., Tytgat, J., Yu, C., San, B.C.*, et al.* (2002). kappa-Hefutoxin1, a novel toxin from the scorpion Heterometrus fulvipes with unique structure and function. Importance of the functional diad in potassium channel selectivity. The Journal of biological chemistry *277*, 30040-30047.

Story, G.M., Peier, A.M., Reeve, A.J., Eid, S.R., Mosbacher, J., Hricik, T.R., Earley, T.J., Hergarden, A.C., Andersson, D.A., Hwang, S.W.*, et al.* (2003). ANKTM1, a TRP-like Channel Expressed in Nociceptive Neurons, Is Activated by Cold Temperatures. Cell *112*, 819-829.

Sunagar, K., Undheim, E.A.B., Chan, A.H.C., Koludarov, I., Muñoz-Gómez, S.A., Antunes, A., and Fry, B.G. (2013). Evolution stings: the origin and diversification of scorpion toxin peptide scaffolds. Toxins *5*, 2456-2487.

Thorell, T. (1876). On the classification of scorpions. The annals and magazine of natural history; zoology, botany, and geology *4*, 1-15.

Tominaga, M., Caterina, M.J., Malmberg, A.B., Rosen, T.A., Gilbert, H., Skinner, K., Raumann, B.E., Basbaum, A.I., and Julius, D. (1998). The cloned capsaicin receptor integrates multiple pain-producing stimuli. Neuron *21*, 531-543.

Twyman, R.E., Rogers, C.J., and Macdonald, R.L. (1989). Differential regulation of γ-aminobutyric acid receptor channels by diazepam and phenobarbital. Annals of Neurology *25*, 213-220.

Tytgat, J., Chandy, K.G., Garcia, M.L., Gutman, G.A., Martin-Eauclaire, M.-F., van der Walt, J.J., and Possani, L.D. (1999). A unified nomenclature for short-chain peptides isolated from scorpion venoms: α-KTx molecular subfamilies. Trends in Pharmacological Sciences *20*, 444-447.

Venkatachalam, K., and Montell, C. (2007). TRP Channels. Annual Review of Biochemistry *76*, 387-417.

Vives, E., Brodin, P., and Lebleu, B. (1997). A truncated HIV-1 Tat protein basic domain rapidly translocates through the plasma membrane and accumulates in the cell nucleus. The Journal of biological chemistry *272*, 16010-16017.

Vranken, W.F., Boucher, W., Stevens, T.J., Fogh, R.H., Pajon, A., Llinas, M., Ulrich, E.L., Markley, J.L., Ionides, J., and Laue, E.D. (2005). The CCPN data model for NMR spectroscopy: development of a software pipeline. Proteins *59*, 687-696.

Wang, Y.Y., Chang, R.B., Waters, H.N., McKemy, D.D., and Liman, E.R. (2008). The nociceptor ion channel TRPA1 is potentiated and inactivated by permeating calcium ions. The Journal of biological chemistry *283*, 32691-32703.

Waterhouse, A.M., Martin, D.M.A., Barton, G.J., Procter, J.B., and Clamp, M. (2009). Jalview Version 2—a multiple sequence alignment editor and analysis workbench. Bioinformatics (Oxford, England) *25*, 1189-1191.

Zhang, C., Medzihradszky, K.F., Sánchez, E.E., Basbaum, A.I., and Julius, D. (2017). Lys49 myotoxin from the Brazilian lancehead pit viper elicits pain through regulated ATP release. Proceedings of the National Academy of Sciences of the United States of America *114*, E2524-E2532.

# Chapter 3

## Irritant-evoked activation and calcium modulation of the TRPA1 receptor

**Summary**

The TRPA1 ion channel is expressed by primary afferent nerve fibers, where it functions as a low threshold sensor for structurally diverse electrophilic irritants ranging from small volatile environmental toxicants to endogenous algogenic lipids (Bautista et al., 2013). TRPA1 is also a 'receptor-operated' channel whose activation downstream of metabotropic receptors elicits inflammatory pain or itch, making it an attractive target for novel analgesic therapies (Chen and Hackos, 2015). However, we lack mechanistic insight into how TRPA1 recognizes and responds to electrophiles or cytoplasmic second messengers. Here, we show that electrophiles act through a two-step process in which modification of a highly reactive cysteine (C621) promotes reorientation of a cytoplasmic loop to enhance nucleophilicity and modification of a nearby cysteine (C665), thereby stabilizing the loop in an activating configuration. These actions modulate two restrictions controlling ion permeation, including widening of the selectivity filter to enhance calcium permeability and opening of a canonical gate at the cytoplasmic end of the pore. We propose a model to explain functional coupling between electrophile action and these control points. We also characterize a calcium binding pocket that is remarkably conserved across TRP channel subtypes and accounts for all aspects of calcium-dependent TRPA1 regulation, including potentiation, desensitization, and activation by metabotropic receptors. These findings provide a structural framework for understanding how a broad-spectrum irritant receptor is controlled by endogenous and exogenous agents that elicit or exacerbate pain and itch.

## Introduction

Electrophiles activate TRPA1 through covalent modification of cysteine residues within the channel's cytoplasmic amino terminus (Bahia et al., 2016; Hinman et al., 2006; Paulsen et al., 2014). We have previously shown that three critical cysteines (C621, C641 and C665 in human TRPA1) reside within an intricately folded region situated just below the transmembrane core of the channel (Paulsen et al., 2014). This and a more recent structural study (Suo et al., 2020). suggest that the local chemical environment within this 'allosteric nexus' endows C621 with extraordinary nucleophilic character that likely accounts for the channel's low threshold sensitivity (Bahia et al., 2016). But how this clamshell-shaped region accommodates small and large electrophiles and translates local conformational changes into gating movements remains vague (Suo et al., 2020). TRPA1 is also activated by G protein-coupled or growth factor receptors that stimulate phospholipase C (PLC) signaling pathways (Bandell et al., 2004; Dai et al., 2007; Jordt et al., 2004; Wilson et al., 2013). but the contribution of relevant second messengers, such as cytoplasmic calcium or phosphoinositide lipids, and their sites of action remain controversial (Talavera et al., 2020). Moreover, TRPA1 exhibits bimodal modulation by calcium, which first potentiates then desensitizes electrophile-evoked responses (Jordt et al., 2004; Wang et al., 2008), and for which several mechanisms have been proposed (Hasan et al., 2017; Sura et al., 2012; Wang et al., 2008; Zimova et al., 2018; Zurborg et al., 2007). Here we clarify these important questions from a structural perspective.

## Results

### *Dynamic equilibrium between two states*

TRPA1 exhibits 'flickery' behavior characterized by rapid transitions between open and closed states (Figure 3.1a 3.5a), but a pharmacologically validated open state has not yet been visualized (Paulsen et al., 2014; Suo et al. 2020). Two technical insights enabled us to overcome this limitation. First, extraction with CYMAL-5 NG detergent yielded a stable distribution of two main conformations (Figure 3.1a,b, 3.6, Table 3.1). We then used pharmacological agents to validate these as open and closed states. One conformation bound the antagonist A-96, showed a narrow pore profile (see below), and resembles previously published structures; we designate this conformation as closed. Second, we found that treating TRPA1-expressing cells with an irreversible electrophilic agonist (iodoacetamide, IA) *prior* to detergent extraction biased the equilibrium towards the other main conformation, which showed IA modification of C621 and a wider pore profile (see below), pharmacologically validating it as an activated, open state.

Comparison of these two states revealed significant conformational differences within the transmembrane core and membrane-proximal allosteric nexus (Figure 3.1c-f). In the activated state, the entire transmembrane region rotates by ~15º relative to the stationary cytoplasmic ankyrin repeat domain (Figure 3.1c). Moreover, the voltage sensor-like domain undergoes a near rigid body rotation (Figure 3.1d), which is accompanied by rotation and upward translation of the pore loop and pore helices (Figure 3.1e). These transitions are linked by movements in the S5 and S6 helices: the π-helix in S6 shifts up by one helical turn and, in concert with S5, causes an upward shift of pore helices P1 and P2 (Figure 3.1e); the S4-S5 linker and S5 transmembrane α-helix straighten into a single α-helix (Figure 3.1f), which coordinates movement of the pore helices and S6 to couple the upper and lower gates. Taken together, these transitions are reminiscent of those

seen between closed and desensitised states for the cool/menthol receptor TRPM8, but dissimilar to the more local conformational changes that accompany gating of the heat/capsaicin receptor TRPV1 (Cao et al., 2013; Diver et al., 2019).

***Coupling between upper and lower gates***

Profiles of the ion permeation pathway revealed substantial changes at both upper and lower restrictions (Figure 3.2a,b). We see marked widening of the lower gate formed by residues I957 and V961, dilating the pore diameter from 5.3 to 7.8Å (Figure 3.2c) and increasing its hydrated radius from 0.9 to 2.1Å (Figure 3.2b). These changes are nearly identical to those seen in TRPV1 when comparing apo and capsaicin-activated states, indicative of transition from closed to open, as expected for a true gate that controls ion flux (Cao et al., 2013). Local resolution analysis of the activated TRPA1 map shows that the lower gate has slightly diminished resolution compared to surrounding regions (3.6e), suggesting a dynamic profile that is consistent with the channel's ability to pass cations of different sizes (Bobkov et al, 2011; Karashima et al., 2010);).

At the upper restriction, movement of pore helices P1 and P2 results in an upward shift and dilation of the selectivity filter formed by residues G914 and D915 (Figure 3.2a,b). This alters the overall profile of the outer pore wall from a V- to U-shaped funnel, which increases the restriction diameter from 8.5 to 9.7Å (Figure 3.2d). Remarkably, widening of both upper and lower restrictions is elicited by electrophile attachment to the allosteric nexus, below the transmembrane core, arguing for allosteric coupling between this nexus and both gates. Regarding communication between the gates, we notice that S5 contains a small bend that straightens upon transition to the open state (Figure 3.1f), consequently lifting and rotating the pore helices backward to alter configuration of the selectivity filter (Figure 3.2a). Consistent with these proposed coupling movements, the A-96 antagonist wedges into a pocket near the S5 bend and just beneath the pore

helices (Figures 3.5e and 3.13a-c), as previously described (Paulsen et al., 2014). Thus, A-96 likely prevents opening of the lower gate by locking S5 in its closed (bent) conformation and inhibiting movement of the S5-S6 pore module (Figure 3.13d,g).

What might be the physiologic relevance of such movements in the outer pore region, which alter diameter less dramatically compared to TRPV1? Interestingly, this transition involves upward and outward rotation of D915 (Figure 3.2b,d), a residue that influences calcium selectivity of activated TRPA1 channels (Christensen et al., 2016; Wang et al., 2008). Increased negative electrostatic surface potential in the outer pore region (Figure 3.2d) is consistent with enhanced calcium preference of the activated state (Bobkov et al., 2011; Karashima et al., 2010; Lin King et al., 2019; Wang et al., 2008). Indeed, neither D915A nor D915N mutants have preference for calcium (Wang et al., 2008) and models of these mutants show reduced negative electrostatic surface potential in the activated state (Figure 3.7). Taken together, these observations support the notion that conformational transitions at the level of the selectivity filter account for dynamic ion selectivity of TRPA1 (Bobkov et al., 2011; Karashima et al., 2010; Lin King et al., 2019; Wang et al., 2008).

***Two-step mechanism of electrophile action***

Our activated TRPA1 structure was obtained using IA, which functions as an irreversible agonist by forming stable covalent adducts with cysteines (Figure 3.1a, 3.5a) (Hinman et al., 2006; Macpherson et al., 2007). We observed clear attachment of IA at just one position, C621 (Figure 3.8a), consistent with the exceptional nucleophilic character of this residue (Paulsen et al., 2014; Suo et al., 2020). Strikingly, this modification also stabilized an 'activation loop' (A-loop) in an upward configuration, exposing a pocket containing the modified residue (Figure 3.3a, b, and 3.8a, d), consistent with recently reported structures of the electrophile-modified channel (Suo et al., 2020).

To better visualize agonist attachment, we used a bulky version of IA (BODIPY-IA, BIA) (Figure 3.5e) and solubilized ligand-free and BIA-modified channels with the detergent LMNG, which resulted in higher overall resolutions of 3.1 and 2.6Å, respectively (Figure 3.3 and 3.8c, Table 3.1). While these channels were both trapped in a closed pore state, covalent modification and distinct A-loop conformations could be more clearly observed (Figure 3.3a,b). The downward (ligand-free) A-loop, which was not previously visualized (Suo et al., 2020), occludes the reactive pocket containing C621 and C665 (Figure 3.3a, 3.8d), whereas the upward (electrophile-modified) conformation exposes this pocket. Furthermore, the larger density of BIA confirmed C621 as the primary modification site (Figure 3.3b, 3.8b). Other cysteines within this region (most notably C665) are also modified, but at substantially reduced rates compared to C621 (Bahia et al., 2016). Indeed, in the presence of IA we observed a weaker density associated with C665, which may reflect partial modification at this site (Figure 3.8a), as also observed with benzyl isothiocyanate (BITC) (Suo et al., 2020).

A role for C665 in TRPA1 activation has been unclear (Bahia et al., 2016; Suo et al., 2020). Interestingly, we see that C665 rotates into the pocket containing modified C621 when the A-loop is stabilized in the upward configuration (Figure 3.3a,b). This reorientation of C665 is predicted to lower its $pK_a$ (from 11.2 to 8.8) and enhance nucleophilicity (Figure 3.9h), suggesting that modification at this site also occurs during channel activation. The necessity for modification at one or both cysteines may depend on the size or charge of electrophile modification and whether it sufficiently alters configuration of the reactive pocket. To test this idea, we mutated cysteines (C621, C641, and/or C665) within the vicinity of the reactive pocket and used patch clamp recording to assess their sensitivity to IA and its bulkier cousin, BODIPY-IA. All double mutant combinations were IA insensitive (Figure 3.9b-d), demonstrating that C621 is alone insufficient to

support channel activation by this small electrophile (even though C621 was fully labeled by BODIPY-IA in C641S/C665S double mutants (Figure 3.9g). We next examined single cysteine substitutions and found that C641S behaved similarly to wild type channels (Figure 3.3e, 3.9f), whereas C621S was IA insensitive (Figure 3.3e, 3.9e) and C665S retained ~30% sensitivity (Figure 3.3c,e). This is consistent with a two-step model whereby C621 is the primary site of electrophile modification, priming A-loop reorientation and modification of C665 to elicit full channel activation. Suo et. al. concluded that C665 modification is not required for channel activation (Suo et al., 2020), perhaps because they used relatively bulky electrophiles (BITC and JT010) that stabilize the open pocket by modifying C621 alone.

Further evidence for this model comes from measurement of channel closure times, which reflect coupling efficiency between agonist binding and channel gating. To assess this parameter, we examined tail currents following activation of channels by membrane depolarization in the absence or presence of irreversible agonists. For wild type TRPA1 channels, the rate of channel closure was slowed ~3-fold by IA (Figure 3.10), as expected if electrophile modification enhances coupling efficiency of A-loop reorientation to channel gating. For C665S mutant, which retains appreciable sensitivity to IA, the rate of channel closure was similar to that determined without agonist (Figure 3.10a,b), suggesting that modification at C665 is important for stabilizing and coupling A-loop reorientation to gating. BODIPY-IA attaches to only one site, suggesting that bulky electrophiles stabilize active A-loop conformation by modifying C621 alone. Remarkably, the single C665S mutant showed full sensitivity to BIA with regard to response magnitude and tail current decay time (Figure 3.10a,c), confirming this notion.

How might upward A-loop stabilization couple to channel gating? In this loop configuration, K671 is stabilized and becomes resolved through its interaction with backbone carbonyls at the C-

terminus of the TRP domain (Figure 3.3a,b, 11), a conserved α-helical motif that lies parallel to the inner membrane leaflet and is implicated in gating of numerous TRP channel subtypes (Hilton et al., 2019). The positively charged side chain of K671 enhances the dipole moment of the TRP helix (Figure 3.11a,b), strengthening the positive electrostatic surface potential at its N-terminus (Figure 3.11c,d). We speculate that this promotes repulsion between TRP domains from neighboring subunits, thereby biasing conformational equilibrium of the channel towards the open state by driving expansion of overlying S6 domains that constitute the lower gate (Figure 3.11e).

K671 is conserved across vertebrate TRPA1 channels (Figure 3.11f). Mutation to the cognate residue in the fly orthologue (K671A) rendered hTRPA1 insensitive to IA or to concentrations of AITC around its $EC_{50}$ (~30 μM), as expected if K671 is critical for propagating local conformational changes in the modified A-loop to the channel gate. We have previously shown that TRPA1 lacking critical cysteines retains sensitivity to high concentrations of AITC (~10X $EC_{50}$) and that this is mediated through modification of another lysine residue (K710) proceeding the S1 helix[3]. Indeed, we found that K671A channels are activated by 1 mM AITC, demonstrating that this mutant is functional, and that modification of K710 activates the channel through a mechanism distinct from what we propose for cysteine modification. Interestingly, K710 is also in proximity to the TRP domain and modification at this site may induce movement in this critical helix independent of A-loop engagement.

***Structurally conserved calcium control site***

When TRPA1 was solubilized in LMNG, a robust density was seen at the bottom of each S2-S3 α-helices facing the cytoplasm (Figure 3.4a, 3.12a), where it is surrounded by residues E788, Q791, Y799, N805, and E808, typical of calcium coordination sites (Wang et al., 2009). Indeed,

this configuration is strikingly similar to a calcium binding site seen in TRPM2, 4 and 8, with all relevant residues conserved (Figure 3.4a,b) (Autzen et al., 2018; Diver et al., 2019; Huang et al., 2018; Zhang et al., 2018). Because channel purification was carried out in nominally calcium-free buffers, this density likely represents cellular calcium bound to a high affinity site. Interestingly, the proximal S2-S3 loop is better resolved compared with PMAL-C8 structures, where calcium is likely lost during prolonged detergent-amphipol exchange.

Permeating calcium has two sequential effects on TRPA1, first enhancing currents and then promoting desensitization (Jordt et al., 2004; Wang et al., 2008) A TRPA1 E788S mutant lacked calcium-mediated potentiation but retained desensitization (Figure 3.4c,d), consistent with previous observations (Zimova et al., 2018), whereas a triple mutant (E788S, Q791S, and N805S) lacked both. The ability of TRPA1 to function as a receptor-operated channel is likely mediated through consequent release of calcium from intracellular stores (although metabolism of phosphoinositide lipids has also been implicated) (Talavera et al., 2020) . To ask if this action converges on the same calcium site identified here, we co-expressed the M1 muscarinic receptor and TRPA1 in transfected cells and recorded carbachol (an M1 agonist)-evoked TRPA1 responses in the absence of extracellular calcium. As previously shown (Jordt et al., 2004), carbachol elicited robust currents that were blocked by A-96 and absent when intracellular calcium was depleted by thapsigargin pre-treatment or rapidly chelated by EGTA and BAPTA (Figure 3.4e,g, 3.12b,c), reaffirming calcium as the critical second messenger. Most interestingly, the E788S mutant showed no response to carbachol (Figure 3.4f,g), demonstrating that major regulatory actions of calcium converge on this single site.

**Discussion**

Detectors of noxious stimuli function as early warning systems that recognize potentially injurious events before they elicit wholesale tissue damage. To accomplish this, they must balance low threshold sensitivity with high fidelity. The two-step mechanism we propose for electrophile-mediated TRPA1 activation satisfies this requirement and may be especially important for detecting small volatile environmental toxicants (Figure 3.13e). For larger endogenous algogens that drive inflammatory pain, signal-to-noise considerations are perhaps less relevant since rapid recognition and escape are not germane, and thus single modification by these bulkier electrophiles may suffice (Figure 3.13f).

TRP channels contain two highly dynamic constrictions along their ion permeation pathway (one corresponding to a canonical lower gate and another at the level of the selectivity filter) that must functionally couple to control activation by diverse stimuli. Our findings suggest that the upper restriction has evolved to serve a range of physiologic functions in this ion channel superfamily: in voltage-gated potassium channels and some TRP channels (*i.e.,* TRPM2) this region is devoted largely to ion selection (Doyle et al., 1998; Huang et al., 2018) , whereas in TRPV1 it serves as a regulated gate (Cao et al., 2013). In the case of TRPA1, our results suggest an intermediate function controlling dynamic ion selectivity, which likely underlies the differential ability of activators to elicit pain with or without neurogenic inflammation (Lin King et al., 2019).

The calcium binding site we identify in TRPA1 supports an emerging picture of a conserved structural motif for detecting elevated intracellular calcium over a range of concentrations resulting from channel activation and/or store release. In TRPM8 this conserved calcium binding pocket is adjacent to a ligand binding site, and calcium is required for channel activation by the synthetic super-cooling agent, icilin (Chuang et al., 2004; Diver et al., 2019; Yin et al., 2019). Whether

calcium similarly regulates TRPA1 in concert with as-yet undiscovered ligands or post-translational modification (Meents et al., 2017), or how calcium binding effects gating movements, remain intriguing questions for future studies.

## Methods

### *Protein expression and purification*

Human TRPA1 was expressed and purified as described previously with slight modifications (Paulsen et al., 2014) . Briefly, N-terminal-tagged MBP-TRPA1 under the control of a CMV promoter was expressed in HEK293F cells using the BacMam system (Thermo Fisher). Cells were purchased from ATCC, where they were validated and certified free of mycoplasma contamination. Protein expression was induced at cell density 1.5-2.5 × $10^6$ cells $ml^{-1}$ with media supplemented with 5 mM sodium butyrate and 5 μM ruthenium red. After 16 hr. at 37 °C, cells were harvested by centrifugation at 1,000 × *g* for 10 mins. Cells were resuspended in lysis buffer (50 mM HEPES, pH 8.0, 150 mM NaCl, 1 mM $IP_6$, 1 mM DTT, 1 mM EDTA, protease inhibitors) and lysed by sonication. Cell membranes were isolated by ultracentrifugation at ~180,000 × *g* for 45 mins and the pellet was resuspended in lysis buffer before multiple passes through a glass homogenizer. Cell membranes were solubilized by addition of LMNG or CYMAL-5 NG (Anatrace) to a final concentration of 0.5 % (w/v) and rocking at 4°C for 1 hr. Insoluble debris was removed by centrifugation at ~35,000 × *g* for 20 mins. and the supernatant passed over amylose beads by gravity flow at 4°C. The beads were washed with wash buffer (50 mM HEPES, pH 8.0, 150 mM NaCl, 1 mM $IP_6$, 1 mM DTT, 0.005% LMNG/CYMAL-5 NG) and eluted with wash buffer supplemented with 10 mM maltose.

For exchange into amphipol, PMAL-C8 was added to the detergent-solubilized sample in a 3:1 PMAL:protein ratio. The solution was mixed by rocking at 4°C for 1 hr. before addition of 100 μl bio-beads (Biorad) $ml^{-1}$ of protein sample. The sample with bio-beads was mixed by rocking at 4°C overnight. The bio-beads were spun down in a tabletop centrifuge at 100 × *g* and the

supernatant analyzed by size exclusion chromatography in detergent-free buffer (50 mM HEPES, pH 8.0, 150 mM NaCl, 1 mM $IP_6$, 1 mM DTT). Peak fractions corresponding to TRPA1 were pooled and concentrated 0.5 - 2 mg $ml^{-1}$ in a 100K MWCO centrifuge concentrator.

***Agonists and antagonists***

To acquire samples of activated TRPA1 for structural studies, cell membranes containing TRPA1 was incubated with 100 μM iodoacetamide (IA) or BODIPY-IA (Millipore Sigma) for 10 min. prior to protein purification. Samples of antagonist-bound TRPA1 were acquired by incubating the purified channel with 10 μM A-967079 (A-96) (Tocris) for 10 mins. prior to cryo-EM grid preparation.

***Rationale and interpretation of solubilization conditions***

TRPA1 protein was imaged in PMAL-C8 amphipol or LMNG detergent. When apo TRPA1 was solubilized CYMAL-5 NG and exchanged into PMAL-C8, we observed two conformational states (closed and open) within the same sample (Figure 1a), both of which lacked ions in the calcium binding site. However, the A-loop could not be modelled, consistent with the dynamic nature of the loop and the ability of the channel to adopt different states (Figure 3.6e). Treatment with IA stabilized the A-loop in the 'up' conformation in conjunction with an open pore, which we therefore designated an activated state of the channel. Addition of agonist before detergent extraction from membranes was crucial for isolating the channel in the activated state, presumably because solubilization in detergent or amphipol prevents dynamic exchange between different channel conformations. Consistent with this notion, when A-96 was added after channel solubilization in PMAL-C8, the antagonist recognized, but did not shift the equilibrium towards the closed conformation. In LMNG, which produced structures of higher resolutions, the transmembrane core

of the channel adopted a closed conformation under both apo and BIA conditions, possibly due to locking of the transmembrane domain by LMNG and/or desensitization of the channel by bound ions in the calcium binding site. This configuration resembles that previously described by us or Suo et. al.. Consistent with a strongly biased closed state, the A-loop was clearly observed in the 'down' (closed) conformation of the apo channel. However, modification of TRPA1 by BIA stabilized the A-loop in the 'up' (activated) conformation in conjunction with a closed pore, which likely represents an intermediate state of the channel following electrophile modification.

***Cryo-EM data collection and processing***

Samples for cryo-EM were prepared by applying 4 µl of purified TRPA1 to 1.2/1.3 holey carbon grids (Quantifoil) and blotting for 8-12 sec. in a Vitrobot Mark IV (Thermo Fisher) prior to plunge freezing in liquid ethane. For multi-shot imaging, samples were prepared on 2/2 holey carbon grids (Quantifoil) and blotted for 6-8 s. Cryo-EM samples were imaged on Polara and Titan Krios microscopes (Thermo Fisher, see Table 3.1 for details) equipped with the K2 Summit camera (Gatan). Movies were drift-corrected using *MotionCor2* (Zheng et al., 2017) and CTF parameters estimated with *gctf* (Zivanov et al., 2018). Particle images were selected from micrographs using *gautomatch* (MRC-LMB, https://www.mrc-lmb.cam.ac.uk/kzhang/) and extracted in *Relion* (Zivanov et al., 2018). 2- and 3-D classification of particle images was performed in *cryoSPARC* (Punjani et al., 2017) and 3D maps refined in *cryoSPARC* and *cisTEM* (Grant et al., 2018). Conversion of data from *cryoSPARC* to *Relion* and generation of orientation distribution plots were performed using *pyem* (Asarnow et al., 2019). Directional Fourier shell correlations of cryo-EM maps were performed as previously described (Dang et al, 2017).

***Model building and analysis***

Cryo-EM maps were visualized with UCSF Chimera (Pettersen et al., 2004). Atomic models were built into the cryo-EM maps with Coot (Emsley et al., 2010) using the previously published structure of TRPA1 as a starting model (PDB-ID: 3J9P). The models were refined over multiple rounds using PHENIX Real Space Refinement (Afonine et al., 2018). Ligands were built using Coot and their geometric restraints calculated with Phenix eLBOW (Moriarty et al., 2009). Cysteine $pK_a$s were calculated in H++ (Anandakrishnan et al., 2012) and the resultant values used to solve the Henderson-Hasselbalch equation (Henderson, 1908; Hasselbalch, 1917) to determine the percentage free sulfhydryl (Figure 3.9h). Electrostatic surface potentials for the Apo-LMNG and BODIPY-IA-LMNG structures were calculated in APBS (Baker et al., 2001) using an AMBER forcefield and are displayed at ± 10 $kT/e^-$ (Figure 3.2d; 3.7 and 3.11).

***Agonist-binding assay***

800 mL cultures of HEK293F cells (1.0 million cells/ml) were transfected with wild-type or mutant TRPA1 DNA using FectoPro (Polyplus Transfection) reagent. Cultures were supplemented with sodium butyrate immediately after transfection and grown for 2 days at 37°C, 8 % CO2, and with shaking at 135 RPM. Cells were harvested by centrifugation at 1000 × *g* for 10 mins and then resuspended in 20 ml of lysis buffer (see above in "Protein expression and purification"). The cells were incubated with 100 μM BODIPY-IA (Millipore Sigma) for 10 mins prior to TRPA1 purification (described above in "Protein expression and purification"). The fluorescence of the purified/modified protein was quantified using a plate reader (excitation/emission: 455/520 nm), normalized for protein concentration measured by TRP fluorescence (excitation/emission: 280/337 nm).

### *Molecular Biology and Cell Culture*

Full-length wild-type human TRPA1 in the mammalian/oocyte expression vector pMO and full-length wild-type human M1 muscarinic acetylcholine receptor in the mammalian expression vector pcDNA3.1 served as templates for all physiology experiments (Cordero-Morales et al., 2011; Gracheva et al., 2010; Paulsen et al., 2014). Constructs generated from these templates were produced by Gibson assembly (New England Biolabs) and verified by sequencing. HEK293T (ATCC) cells were cultured at 37 °C, 5% $CO_2$ in DMEM Complete (DMEM-C; Dulbecco's modified Eagle's medium containing 10% (v/v) heat-inactivated calf serum, 100 U $ml^{-1}$ Penicillin G and 0.1 mg $ml^{-1}$ Streptomycin). These cells were purchased from ATCC, where they were validated and certified free of mycoplasma contamination. For heterologous expression, HEK293T cells were transfected with 1 μg of TRPA1 and/or M1 with 100 ng of eGFP in pcDNA3.1, which were combined with 3x (w/w) Lipofectamine 2000 (Thermo-Fisher) for 8 hrs. in Opti-MEM (Thermo Fisher). Cells were then plated onto coverslips coated with 0.01% poly-L-Lysine (MW 70-150,000, MilliporeSigma) and adhered to these coverslips for at least 12 hr. before use in calcium-imaging or electrophysiology experiments.

### *Calcium imaging*

Ratiometric $Ca^{2+}$-imaging was carried out on transfected HEK293T cells prepared as above. Adherent cells were loaded for 30 min. in the dark at room temperature (RT) in Ringer's solution containing 0.1 mg $ml^{-1}$ Fura-2 AM dye and 0.02% (w/v) Pluronic F-127. Data were generated by exciting the cells with 340 then 380 nm light using a Lambda DG-4 Illuminator (Sutter), imaged with a Grasshopper3 camera (FLIR), then analyzed in MetaFluor (Molecular Devices). Data were quantified as the ratio of 340 to 380 nm fluorescence after background subtraction.

***Electrophysiology***

Capillary pipettes from borosilicate glass with filament (O.D × I.D, 1.10 × 0.86 mm, Sutter Instruments) were fashioned and fire-polished to a resistance of 0 – 5 mΩ for whole-cell recordings and 5 – 10 mΩ for excised patch recordings. Electrophysiological data were collected at RT using an Axopatch 200B amplifier (Axon Instruments) and digitized with a Digidata 1550B (Axon Instruments). Voltage protocols were delivered and resulting currents monitored on-line with pClamp10 (Molecular Devices), then analyzed off-line in pClamp or Prism (GraphPad). All electrophysiological recordings and pharmacological manipulations were carried out under laminar flow using a pressure-driven micro-perfusion system (SmartSquirt, Automate Scientific).

For whole-cell recordings, the bath solution consisted of $Ca^{2+}$-free Ringer's solution (140 mM NaCl, 10 mM HEPES, 5 mM KCl, 2 mM $MgCl_2$, and 10 mM Glucose; pH 7.4 with NaOH; 290-300 mOsm $kg^{-1}$data), data were digitized at 10 kHz and filtered at 1 kHz. The internal solution contained 140 mM $CsMeSO_4$; 10 mM HEPES; 1 mM $MgCl_2$; and, as indicated, 0 or 1 mM EGTA. The pH was set to 7.2 with CsOH and osmolarity to 300-310 mOsm $kg^{-1}$ with sucrose. Unless otherwise stated in the figure legends, analysis of IA- and BIA-evoked TRPA1 currents in whole-cell patch clamp mode was carried out at $V_{hold}$ = -80 mV. Current-voltage relationships were then measured at steady state in response to voltage steps (500 msec.) from -80 to 80 mV in 10 mV increments using on-line leak subtraction (P/4). Tail-currents were then evoked by a brief (250 msec.) test pulse of -120 mV. The decay-time constant $\tau$ for each tail-current was determined by fitting a one-phase exponential decay function in pClamp to the tail-current obtained following the 80 mV step (Sakmann & Neher, 2009). For analysis of $Ca^{2+}$-modulation, TRPA1 currents were continuously monitored over a 500 msec voltage ramp from -80 to 80 mV. Inside-out excised-patch recordings were carried out in symmetrical solutions of 150 mM NaCl, 10 mM HEPES, 2

mM EGTA, 1 mM $MgCl_2$, and 1 mM $IP_6$; pH 7.3 with NaOH; 300-310 mOsm $kg^{-1}$ at a constant holding voltage of -40 mV; sampled at 20 kHz; and filtered at 2 kHz.

***Statistics and Experimental Design***

Electrophysiological data are presented as mean ± S.E.M. unless otherwise noted. We carried out statistical testing in Prism (GraphPad). Where appropriate, we used parametric significance tests assuming equal variance and a normal distribution of data. Where either of these assumptions were violated, we used non-parametric tests, as indicated in the figure legends. Choice of tests were justified given the experimental design; they are standard tests for similar experiments. For all tests, *a priori*, we set $\alpha = 0.05$ and represent statistical significance with the *p* value, as indicated in the figure legends. We selected sample sizes for all experiments based on our laboratory and others' experience with similar assays, and in consideration of reagent availability and technical feasibility. We made no predetermination of sample size and thus carried out the minimum number of biological replicates required for strong inference and reproducibility, as indicated in the figure legends.

***Data Availability and Code Availability***

Cryo-EM maps have been deposited in the Electron Microscopy Data Bank under EMD-21127, EMD-21128, EMD-21129, EMD-21130, EMD-21131, EMD-21537, and EMD-21538. Atomic models have been deposited in the Protein Data Bank under 6V9V, 6V9W, 6V9X, and 6V9Y.

## Figures

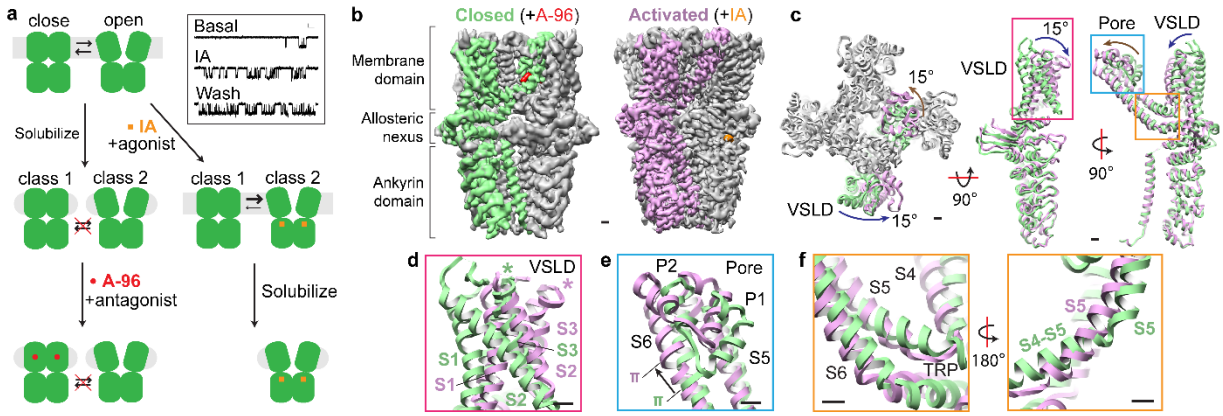


***Figure 3.1 Dynamic equilibrium between closed and activated conformations***

**(A)** Closed and open states of TRPA1 were captured by incubation with an irreversible electrophilic agonist (Iodoacetamide, IA) or an antagonist (A-967079, A-96) before or after membrane solubilization, respectively. Representative inside-out patch recordings show spontaneous (basal) and IA (100 μM)-evoked (persistent) TRPA1 channel openings ($V_{hold}$ = -40 mV; scale bars: x = 10 msec., y = 2 pA, n = 9 independent experiments.

**(B)** Cryo-EM density maps of TRPA1 bound to A-96 or IA in closed or activated state, respectively. A-96 binds to the membrane domain while iodoacetamide binds to the allosteric nexus.

**(C)** Comparison between subunits in closed and activated conformations showing ~15° rotation of voltage sensor-like domain (VSLD) and twisting and translation of pore domain. Ankyrin repeat domain remains stationary.

**(D)** VSLD rotates around the cytoplasmic base of transmembrane α-helices S1 and S2 in a near-rigid-body movement.

**(E)** Pore domain twists and translates upward towards the extracellular milieu, concomitant with a shift in the S6 π-helix by one helical turn.

**(F)** Conformational changes in the upper pore region are coupled to widening of the lower gate through straightening of the S5 α-helix, enabling movement of S6 to facilitate gating. Scale bars: 10Å.

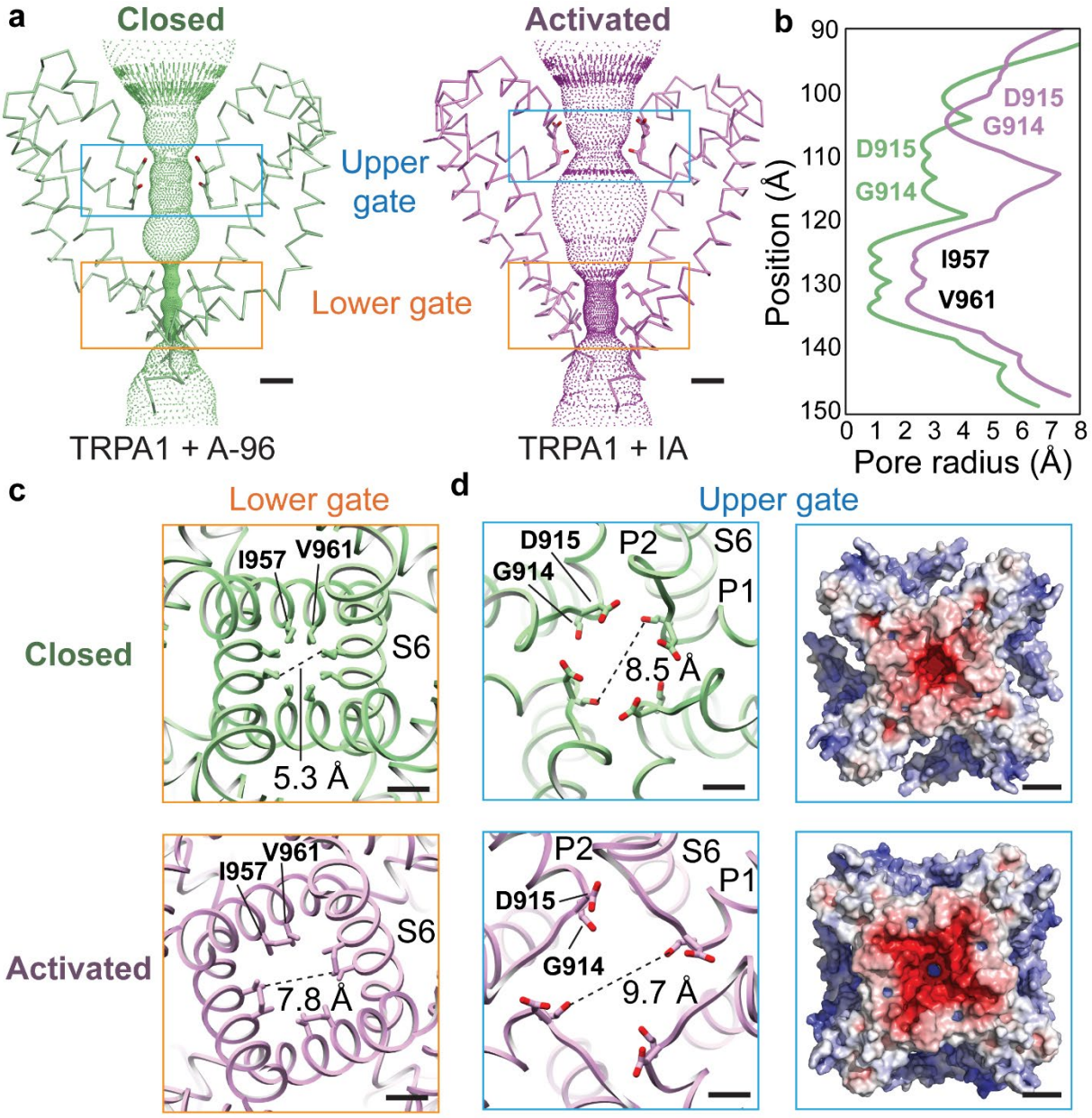


***Figure 3.2 Coupled dilation of upper pore region and lower gate***

**(A)** Activation of TRPA1 involves concerted dilation of both upper and lower gates with upward shift of the selectivity filter.

**(B)** Lower gate is formed by residues I957 and V961, while upper gate is formed by D915 and backbone carbonyl of G914.

**(C)** Pore widening is associated with counter-clockwise rotation of transmembrane α-helices (viewed from extracellular face to cytoplasmic side).

**(D)** Acidic residues lining the upper pore create a highly negatively charged surface, especially in the activated conformation, likely facilitating calcium selectivity. Scale bars: 5Å. Electrostatic

surface charge distribution of TRPA1's cytoplasmic face in apo- and activated states were calculated in APBS (Baker et al., 2001) and displayed at ±10 kT/$e^-$. Scale bars: 25Å.

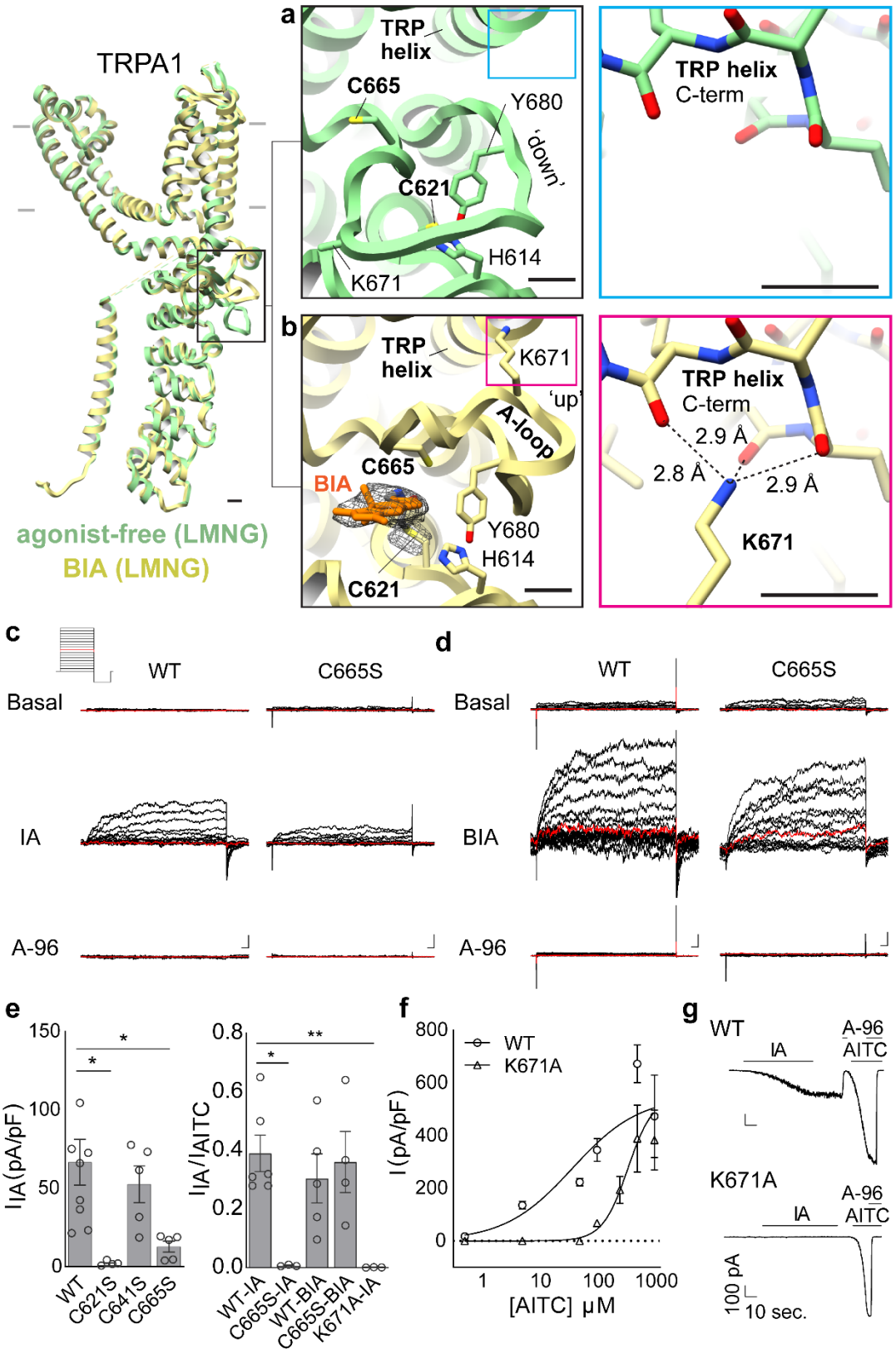
TRPA1
agonist-free (LMNG)
BIA (LMNG)
a
TRP helix
C665
Y680
'down'
C621
H614
K671
TRP helix
C-term
b
TRP helix
K671
'up'
A-loop
C665
BIA
Y680
H614
C621
TRP helix
C-term
2.9 Å
2.8 Å
2.9 Å
K671
c
WT
C665S
Basal
IA
A-96
d
WT
C665S
Basal
BIA
A-96
e
$I_{IA}$ (pA/pF)
$I_{IA}/I_{AITC}$
WT
C621S
C641S
C665S
WT-IA
C665S-IA
WT-BIA
C665S-BIA
K671A-IA
f
I (pA/pF)
WT
K671A
[AITC] µM
g
WT
IA
A-96
AITC
K671A
IA
A-96
AITC
100 pA
10 sec.

***Figure 3.3 Activation by electrophiles occurs through two-step mechanism***

**(A)** A dynamic activation loop (A-loop) adopts a 'down' conformation in the agonist-free channel, partially occluding a reactive pocket containing C621.

**(B)** Following attachment of BODIPY-iodoacetamide (BIA) to C621, the A-loop transitions to an 'up' conformation, bringing C665 into the reactive pocket and repositioning K671 to coordinate backbone carbonyl oxygens at the TRP domain C-terminus. Scale bars: 5Å.

**(C)** IA (100 μM)-evoked currents for WT and C665S mutant TRPA1 channels (n = 9 and 5 independent experiments, respectively), followed by inhibition with A-96 (10 μM).

**(D)** Same for BIA (100 μM)-evoked currents (n = 5 for WT and C665S mutant). 500 msec. voltage steps from -80 to 80 mV, 0 mV colored red. Scale bars: x = 25 msec., y = 100 pA.

**(E)** (left) Quantification of IA-evoked currents for WT or mutant TRPA1 channels at 80 mV (n = 9 and 5 independent experiments/construct, respectively). (right) Normalized IA-evoked currents (TRPA1 WT, n = 6; C665S, n = 3; K671A, n = 3) and BIA-evoked currents (TRPA1 WT n = 5; C665S, n =4). *, $p = 0.05$; ** $p = 0.007$, Kruskal-Wallis test with post-hoc Dunn's correction for multiple comparisons. Data displayed as ± S.E.M.

**(F)** AITC dose-response curves for WT ($EC_{50}$ = 37; 95% CI: 30 – 46 nM) and K671A ($EC_{50}$ = 344; 95% CI: 313 – 381 nM) TRPA1 channels. $EC_{50}$ values determined by nonlinear Poisson regression and statistically significant difference confirmed with extra sum-of-squares F test ($p < 0.0001$). n = 3 cells/dose/construct except K671A 50 mM (n = 6) and 100 mM (n = 4). Data are displayed as mean ± S.E.M.

**(G)** IA (100 μM) and AITC (1 mM)-evoked whole cell currents for WT and K671A channels ($V_{hold}$ = -80 mV) blocked by A-96 (10 μM). n = 3 independent experiments/construct.

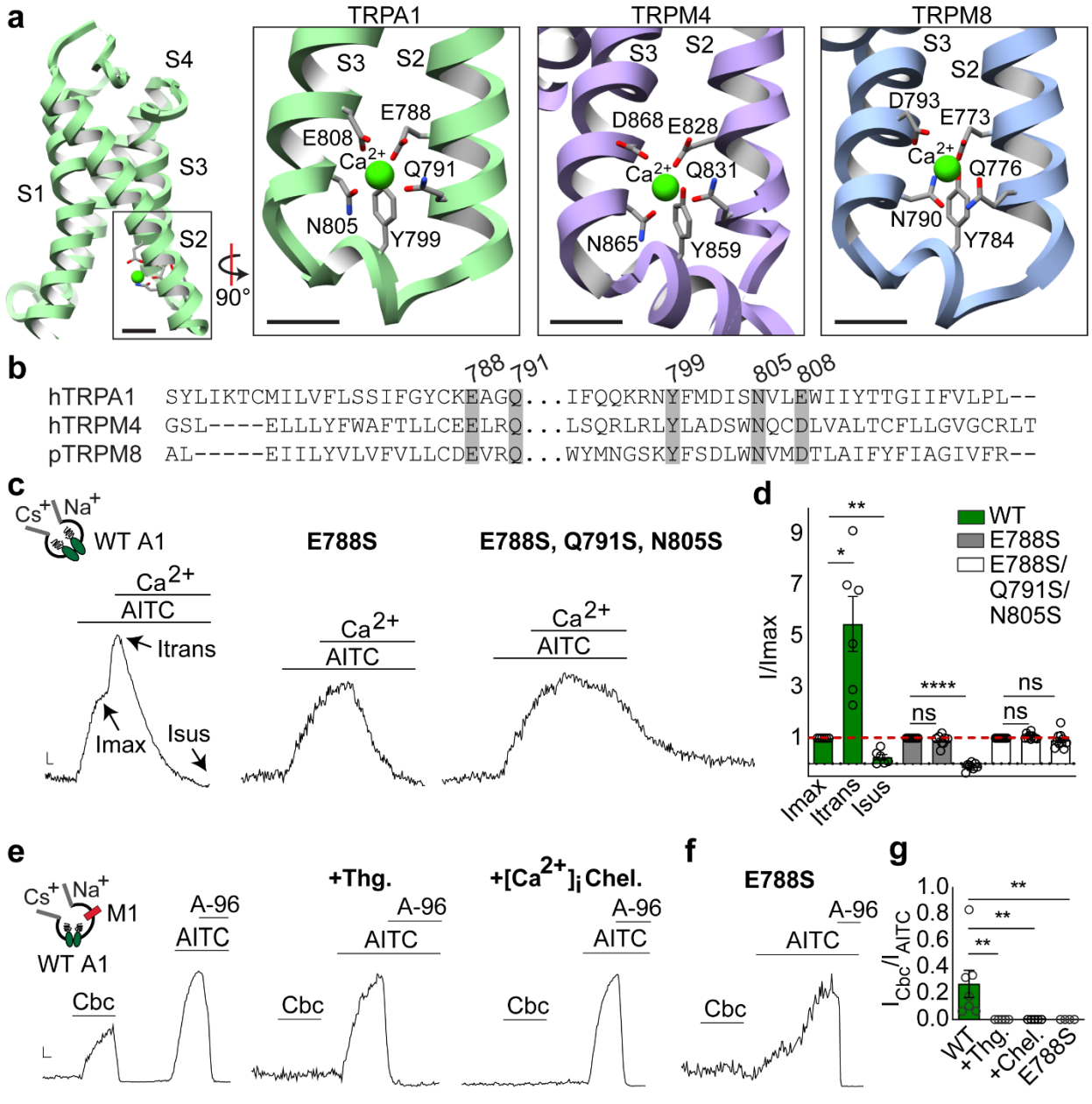


***Figure 3.4 One site subserves three distinct modes of calcium regulation***

**(A)** A calcium ion binds at the cytoplasmic end of S2-S3 helices in the VSD, as seen in TRPM4 and TRPM8. Scale bars = 5Å.

**(B)** Sequence alignment reveals conservation of calcium-coordinating residues in TRPA1, TRPM4 and TRPM8.

**(C)** Normalized whole-cell currents from TRPA1 WT (n = 6 independent experiments), E788S (n = 8), and E788S, Q791S, N80S triple mutant (n = 10) following bath application of AITC (50 μM) and $Ca^{2+}$ (2 mM). Data were extracted from 500 msec. voltage ramps (-80 to 80 mV). Scale bars: x = 1 sec, y = arbitrary units.

**(D)** Quantification of $Ca^{2+}$ potentiation (I-transient, $I_{trans}$, measured 5 secs post-$Ca^{2+}$ application) and desensitization (I-sustained, $I_{sus}$, measured 60 sec post-$Ca^{2+}$ application). WT, n = 6 independent experiments; E788S, n = 8; E788S, Q791S, N805S triple mutant, n = 10. *, $p = 0.04$; **, $p = 0.005$; ****, $p < 0.0001$ one-way mixed-effects analysis ANOVA with post-hoc Holm-Sidak correction for multiple comparisons; Data displayed as mean ± S.E.M.

**(E, F)** Normalized whole cell recordings for TRPA1 channels co-expressed with M1 muscarinic acetylcholine receptor in response to bath applied carbachol (Cbc, 100 μM; data represent n = 7 independent experiments for WT and n = 4 for E788S mutant), with or without Thapsigargin (Thg, 1 μM; n = 5) pre-treatment or inclusion of rapid intracellular $Ca^{2+}$ chelators EGTA and BAPTA (1 mM each; n = 5). AITC, 50 μM and A-96,10 μM. Scale bars: x = 1 sec, y = arbitrary units.

**(G)** Quantification of responses in **e-f**. ** $p = 0.002$ for WT vs. +Thg and +Chel; $p = 0.004$ for WT vs E788S; Kruskal-Wallis test with post-hoc Dunn's correction for multiple comparisons. Data displayed as mean ± S.E.M.

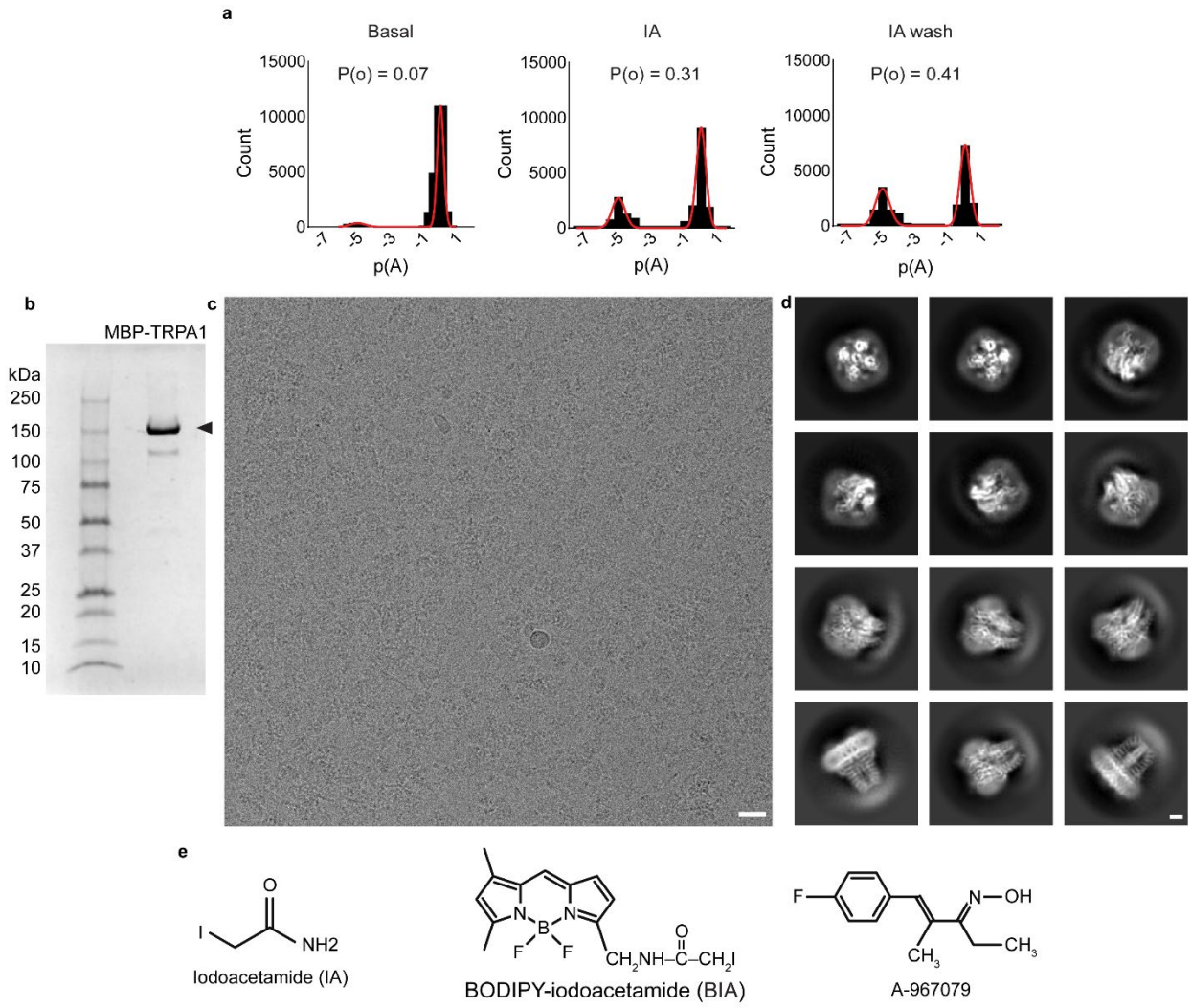


***Figure 3.5 Pharmacology and cryo-EM data collection and processing for TRPA1.***

**(A)** All points histograms depicting the change in open probability (P(o)) in a single TRPA1 channel in response to IA-application. Data represent n = 9 independent excised inside-out patches. $V_{hold}$ = -40 mV.

**(B)** SDS-PAGE showing MBP-TRPA1 (arrowhead) after pull-down and elution from amylose beads.

**(C)** Cryo-EM image of MBP-TRPA1. Scale bar: 20 nm.

**(D)** 2D classification of cryo-EM particle images showing TRPA1 in different orientations. Scale bar: 25 Å.

**(E)** Pharmacological agents used in this study.

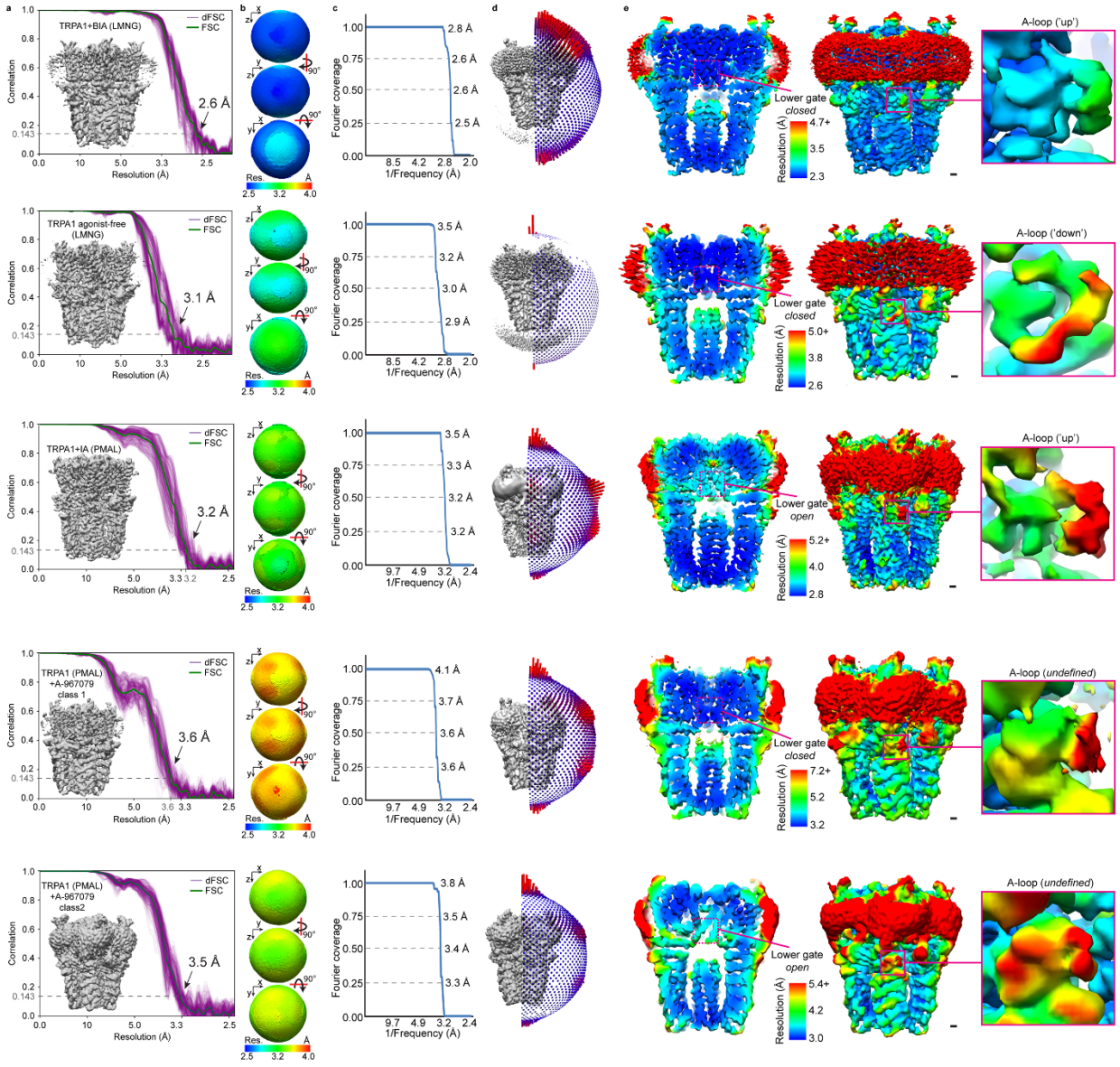


***Figure 3.6 Fourier shell correlation of cryo-EM maps, orientation distribution of particle image views, and local resolution of TRPA1 cryo-EM maps.***

**(A)** Fourier shell correlation and 1D directional Fourier shell correlation plots. TRPA1 (PMAL) + A-967079 class 2 denotes the structure derived from 3D classification of antagonist-treated samples in PMAL and represents the open state channel without antagonist bound.

**(B)** 3D representations of the directional Fourier shell correlation.

**(C)** Fourier space covered, based on dFSC at 0.143.

**(D)** Orientation distribution of particle image refinement angles.

**(E)** The A-loop is lower resolution compared to surrounding map regions, indicating its dynamic nature. In the activated (TRPA1+iodoacetamide) and open state (TRPA1 + A967079 PMAL-C8 class 2) conformations, the bottom of S6 is lower resolution compared to surrounding regions, indicating structural flexibility at the level of the lower gate. Scale bars: 5Å.

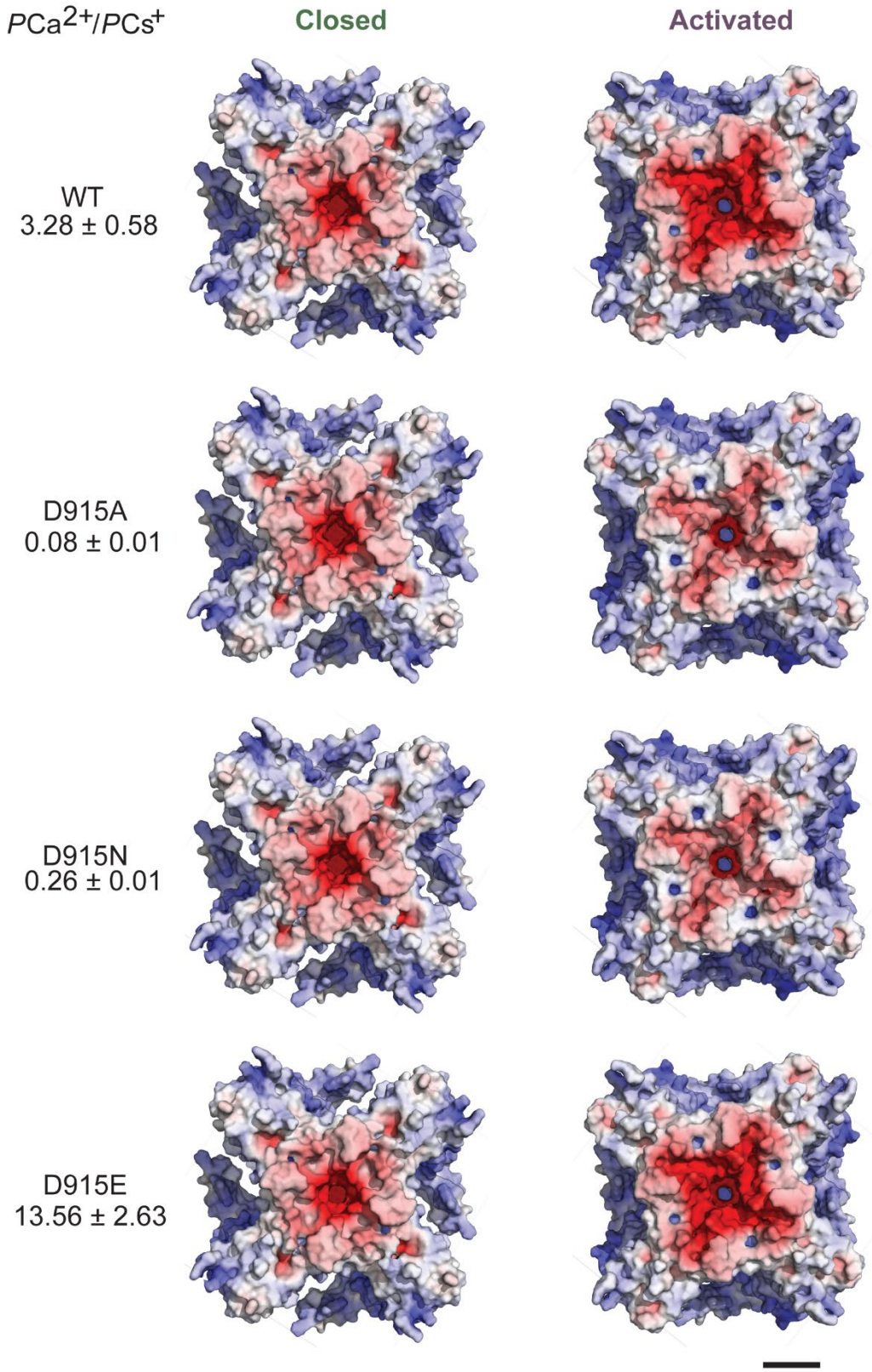
$P_{Ca^{2+}}/P_{Cs^+}$
Closed
Activated
WT
3.28 ± 0.58
D915A
0.08 ± 0.01
D915N
0.26 ± 0.01
D915E
13.56 ± 2.63

***Figure 3.7 Surface charge distribution of TRPA1's extracellular face.***

Electrostatic potential maps were calculated in APBS and are displayed at ± 10 kT/$e^-$. *In silico* mutations of D915 were modeled and experimentally determined relative permeability ratios for these mutations sourced from Wang *et al*. Scale bar: 30Å.

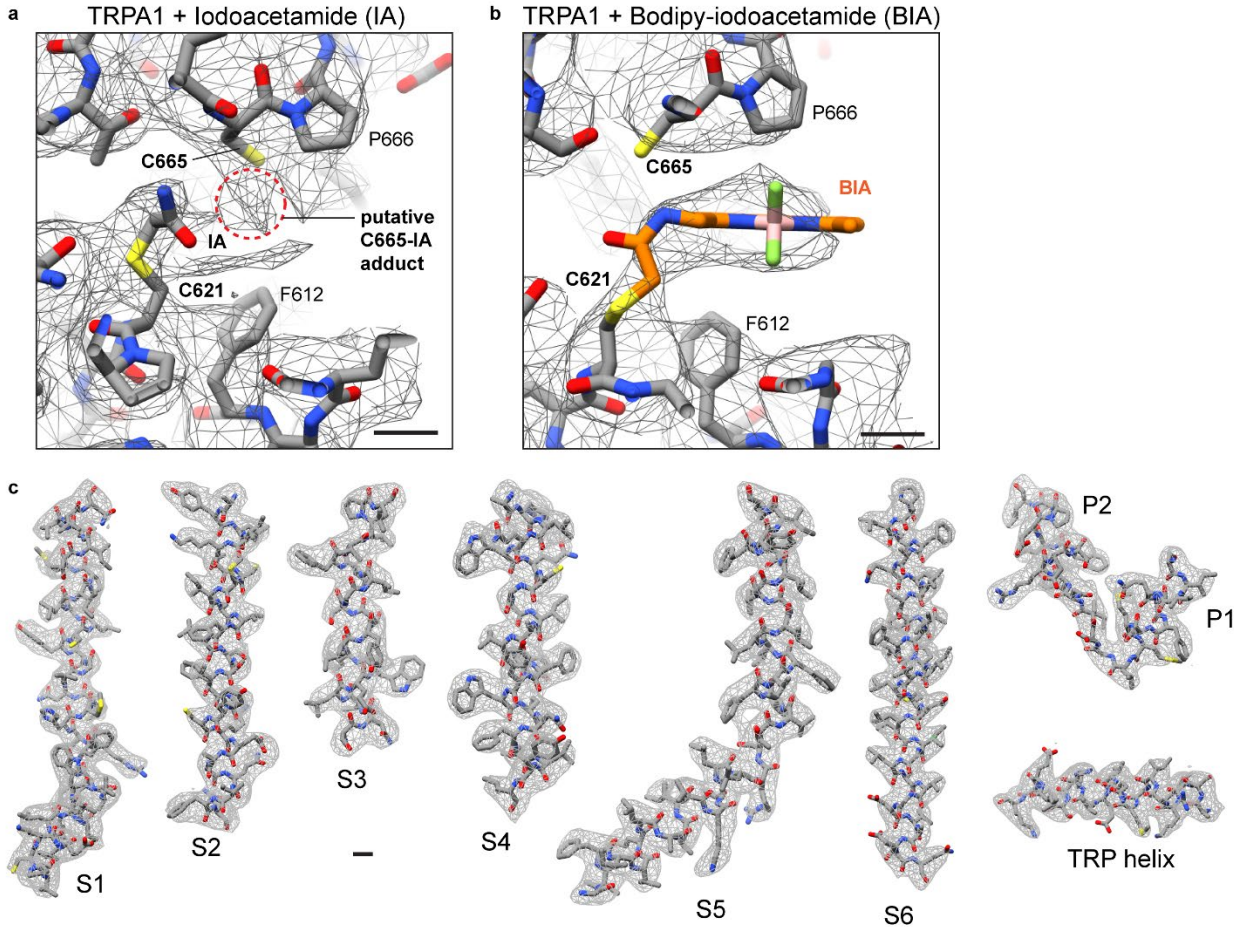
a
TRPA1 + Iodoacetamide (IA)
P666
C665
putative
C665-IA
adduct
IA
C621
F612
b
TRPA1 + Bodipy-iodoacetamide (BIA)
P666
C665
BIA
C621
F612
c
S1
S2
S3
S4
S5
S6
P2
P1
TRP helix
d
TRPA1+A-96 (PMAL-C8)
TRPA1 agonist-free (LMNG)
TRPA1+BIA (LMNG)
σ = 4
σ = 6
A-loop
BIA

***Figure 3.8 Map densities of agonists and transmembrane α-helices.***

**(A)** Strong density is observed for iodoacetamide bound to C621. Weaker density is observed next to C665, which indicate that some of the channels may be modified by agonist at this site. Map threshold: σ = 4.

**(B)** Clear density for BODIPY-iodoacetamide (BIA) is observed bound to C621. No additional density is observed next to C665 in this case. Map threshold: σ = 6.

**(C)** Segmented map densities and atomic models for TRPA1 + BIA (LMNG). Scale bars: 3Å.

**(D)** Map density of the A-loop in different states: undefined (TRPA1+A-96, PMAL-C8), 'down' (TRPA1 agonist-free, LMNG), and 'up' (TRPA1+BIA, LMNG). Densities are shown at two different thresholds (σ = 4 and 6). Scale bars: 5Å.

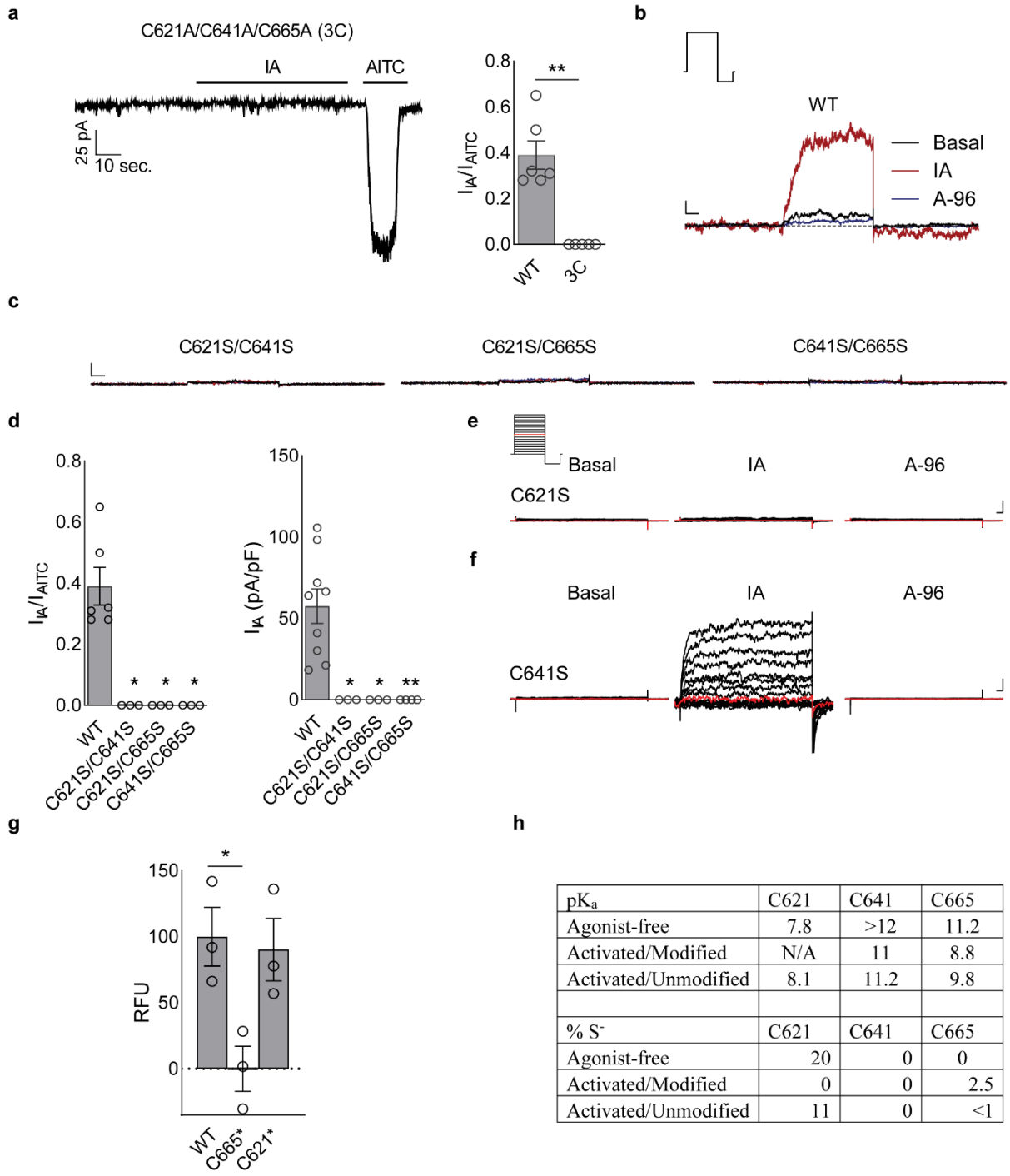


| $pK_a$ | C621 | C641 | C665 |
|---|---|---|---|
| Agonist-free | 7.8 | >12 | 11.2 |
| Activated/Modified | N/A | 11 | 8.8 |
| Activated/Unmodified | 8.1 | 11.2 | 9.8 |
| | | | |
| % $S^-$ | C621 | C641 | C665 |
| Agonist-free | 20 | 0 | 0 |
| Activated/Modified | 0 | 0 | 2.5 |
| Activated/Unmodified | 11 | 0 | <1 |

***Figure 3.9 Characterization of TRPA1 activation by IA and BIA.***

**(A)** IA (100 μM) activates TRPA1 through covalent modification of cysteines; AITC (250 or 1000 μM). Data represent n = 6 (WT) or 5 (3C) independent experiments. Statistical significance is reported as the result of an unpaired two-tailed Mann-Whitney test; **, $p = 0.002$; $V_{hold}$ = -80 mV.

**(B, C)** No single cysteine is sufficient for TRPA1 activation by IA. WT, data represent n = 9 independent experiments ; C621S/C641S n = 3; C621S/C665S, n = 3; and C641S/C665S, n = 4. Data were acquired in whole-cell patch clamp mode and reflect the results of 500 msec. test pulse (80 mV). $V_{hold}$ = -80 mV. Doses: IA, 100 μM; A-96,10 μM; AITC, 250 or 1000 μM. Scale bars: x, 50 msec.; y, 100 pA. I = 0, dashed line**.**

**(D)** Quantification of double cysteine mutant data. (left) WT, n = 6 independent experiments; C621S/C641S n = 3; C621S/C665S, n = 3; and C641S/C665S, n = 3. $V_{hold}$ = -80 mV. (right) WT, data represent n = 9 independent experiments; C621S/C641S n = 3; C621S/C665S, n = 3; and C641S/C665S, n = 4. Doses: IA, 100 μM; A-96,10 μM; AITC, 250 or 1000 μM. Statistical significance is reported as the result of a Kruskal-Wallis test with post-hoc Dunn's test to correct for multiple comparisons; *, $p = 0.02$; **, $p = 0.007$.

**(E, F)** C621S display complete loss of IA sensitivity while C641S retains full sensitivity. Data represent n = 5 independent experiments/construct. Data were acquired in whole-cell patch clamp mode and reflect the results of 500 msec. test pulses from -80 to 80 mV. $V_{hold}$ = -80 mV. Doses: IA, 100 μM; A-96, 10 μM. Scale bars: x, 25 msec.; y, 100 pA.

**(G)** Binding of BIA to TRPA1 C641S/C665S double mutant (C621*) is similar to wildtype. Statistical significance is represented as the results of one-way ANOVA with post-hoc Holm-Sidak correction for multiple comparisons; *, $p = 0.03$; n = 3 independent experiments/construct.

**(H)** TRPA1 cysteine $pK_a$ values and deduced proportion of thiolate in the agonist-free state (PDB-ID: 6V9W), and IA-bound ('Activated,' PDB-ID: 6V9V) state in the presence or absence of covalent modification at C621. All summary data are displayed as the mean ± S.E.M.

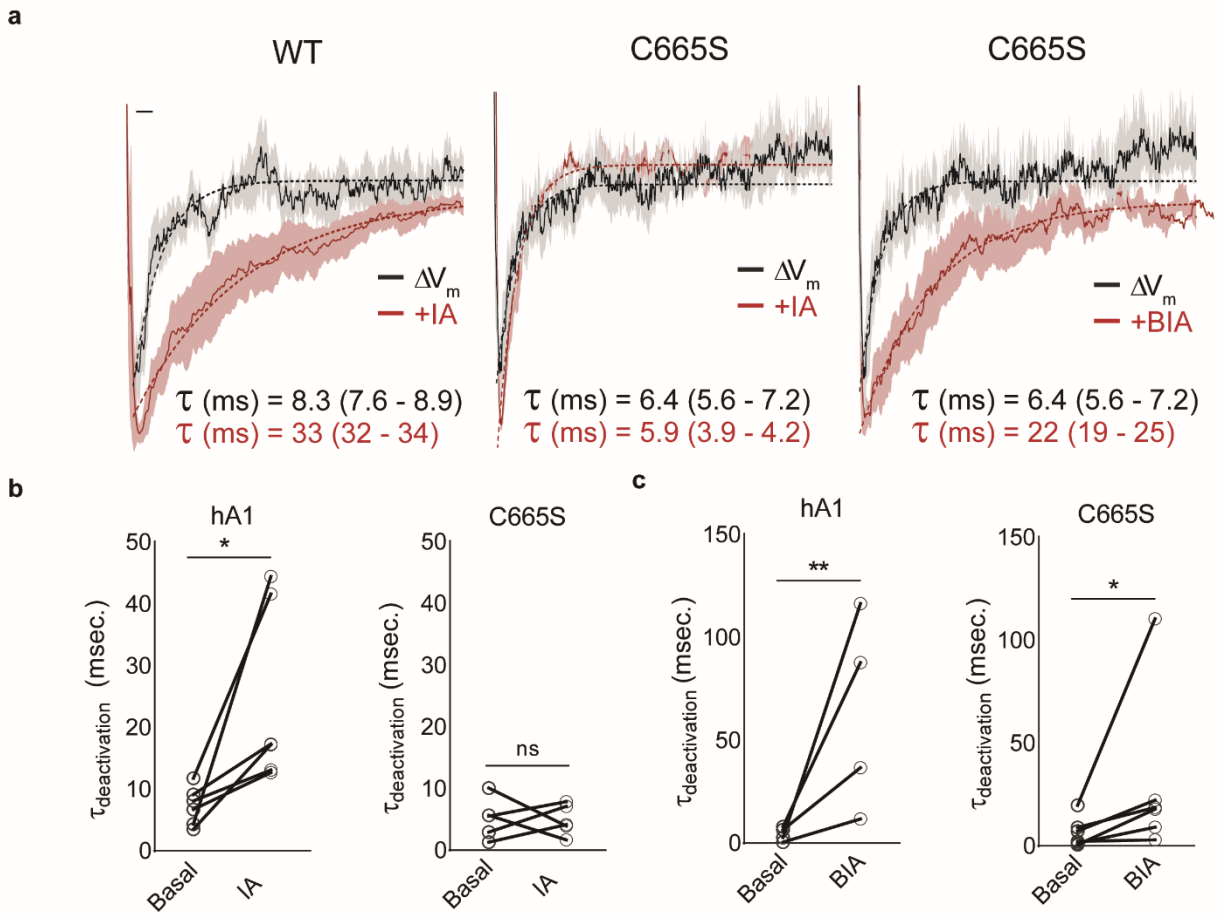


***Figure 3.10 Analysis of TRPA1 tail currents.***

**(A)** Scaled averaged basal (WT, n = 10 independent experiments; C665S, n = 6), IA (100 μM; WT, n = 5; C665S, n = 5), or BIA (100 μM; C665S, n = 6)-evoked tail currents for TRPA1 WT and C665S mutant channels. Mean deactivation time constants (τ) are shown with 95% CI in parentheses. Scale bar: x = 5 msec., y = arbitrary units. Data were acquired in whole-cell patch clamp mode after a 500 msec. pre-pulses (-80 to 80 mV in 10 mV increments) followed by a 250 msec test pulse (-120 mV). $V_{hold}$ = -80 mV.

**(B)** Quantification of changes in IA- and **c**, BIA-evoked TRPA1 tail-current decay time constants in WT and C665S TRPA1. Statistical significance is represented as the results of a ratio paired two-tailed student's t-test; (panel b**)** *, $p = 0.01$; (panel c) *, $p = 0.02$, **, $p = 0.009$.

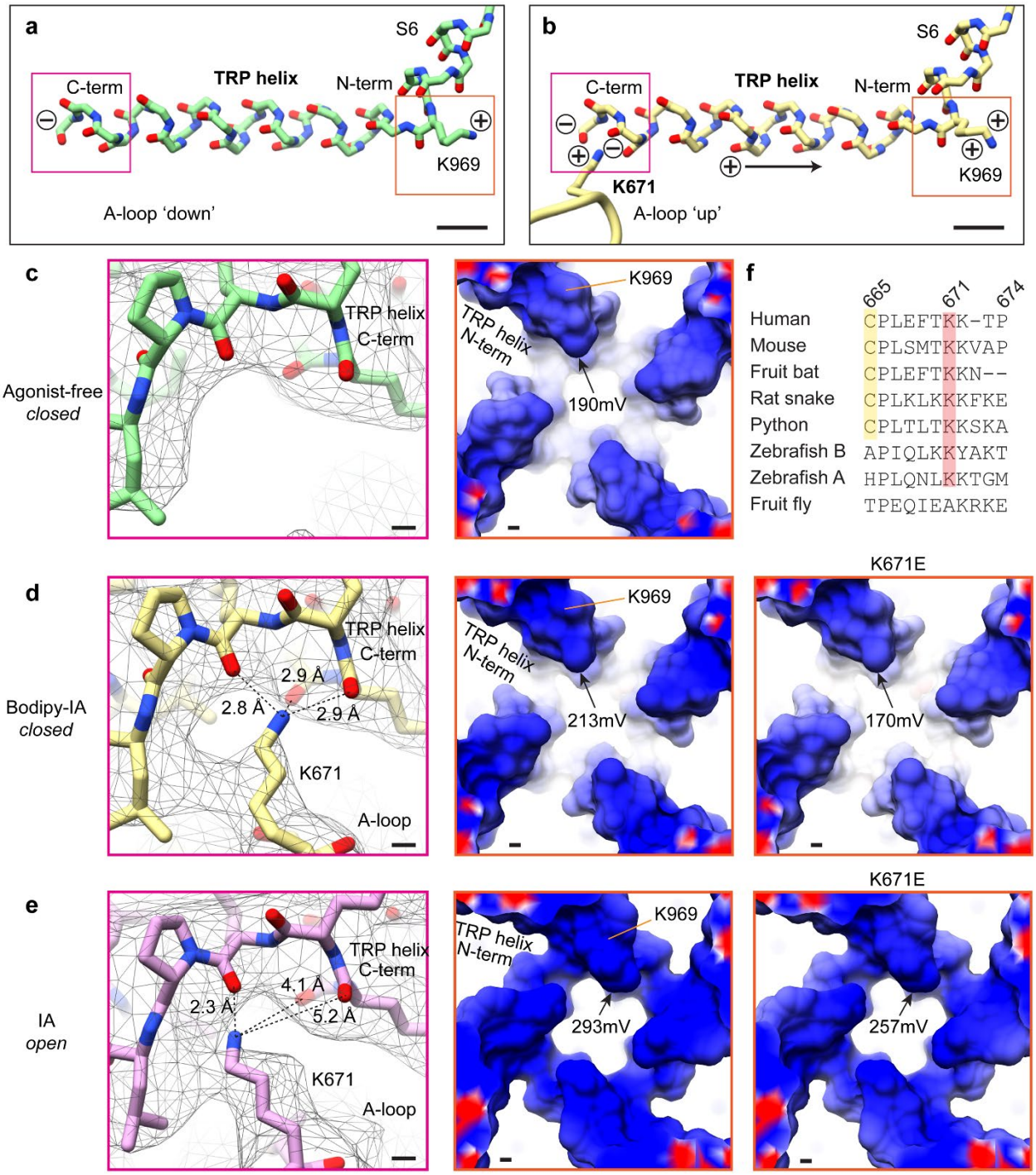


***Figure 3.11 Positive electrostatic potential below the lower gate.***

**(A)** The TRP helix forms an electric dipole with electro-positive K969 at the N terminus and electro-negative carbonyl oxygens at the C terminus.

**(B)** When the A-loop is oriented in the 'up' position, K671 is coordinated by the carbonyl oxygens at the C terminus of the TRP helix and increases its dipole moment to enhance the positive electrostatic potential at the N terminus.

**(C)** The C-terminal carbonyl oxygens of the TRP helix form a pocket that is unoccupied in the agonist-free channel.

**(D)** Coordination of K671 with the carbonyl oxygens at the TRP helix C terminus increases the positive electrostatic potential at the TRP helix N terminus. *In silico* substitution of K671 with glutamate decreases the electrostatic potential of the TRP helix.

**(E)** Conformational changes associated with pore dilation further increase the positive electrostatic potential of the TRP domain.

**(F)** Multiple sequence alignment of TRPA1 orthologs.

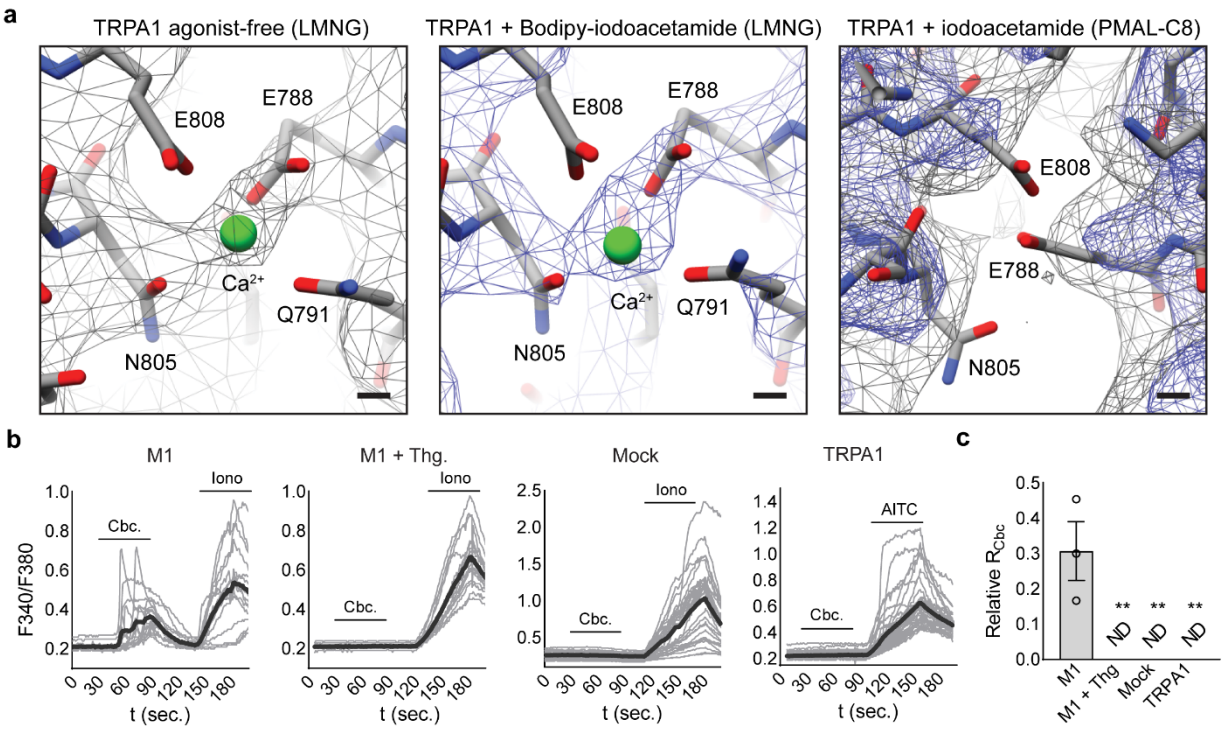


***Figure 3.12 Calcium map densities and calcium-imaging of $Ca^{2+}$ modulation.***

**(A)** Calcium is bound in both agonist-free (σ = 4) and agonist-treated (σ = 8) samples in LMNG detergent, with E788 and N805 displaying the most robust densities coordinating calcium. No density for calcium is observed for the channel in amphipol (gray, σ = 4; blue, σ = 8).

**(B)** Carbachol (Cbc., 100 μM) evokes intracellular $Ca^{2+}$-release through activation of the M1 muscarinic acetylcholine receptor. Cbc. was applied in $Ca^{2+}$-free Ringer's solution with 1 mM EGTA to isolate intracellular responses. n = 16 (M1), 18 (M1 + Thg.), 33 (Mock), or 44 (TRPA1) cells. Each graph represent n = 3 (M1, M1 + Thg.), 4 (Mock), or 5 (TRPA1) independent experiments. Iono., Ionomycin, 1 μM; Thg., Thapsigargin, 1 μM; AITC, 50 μM. Gray traces represent individual cells and black traces the average of all cells in a given experiment.

**(C)** Quantification of $Ca^{2+}$-imaging experiments. The ratio evoked by Cbc. was normalized to the Iono.- or, in TRPA1-transfected cells, AITC-evoked response. *, $p < 0.01$, Kruskal-Wallis test with post-hoc Dunn's test to correct for multiple comparisons; n = 3 (M1, M1 + Thg.), 4 (Mock), or 5 (TRPA1) independent experiments. ND = response not detected. Data represent the mean ± S.E.M.

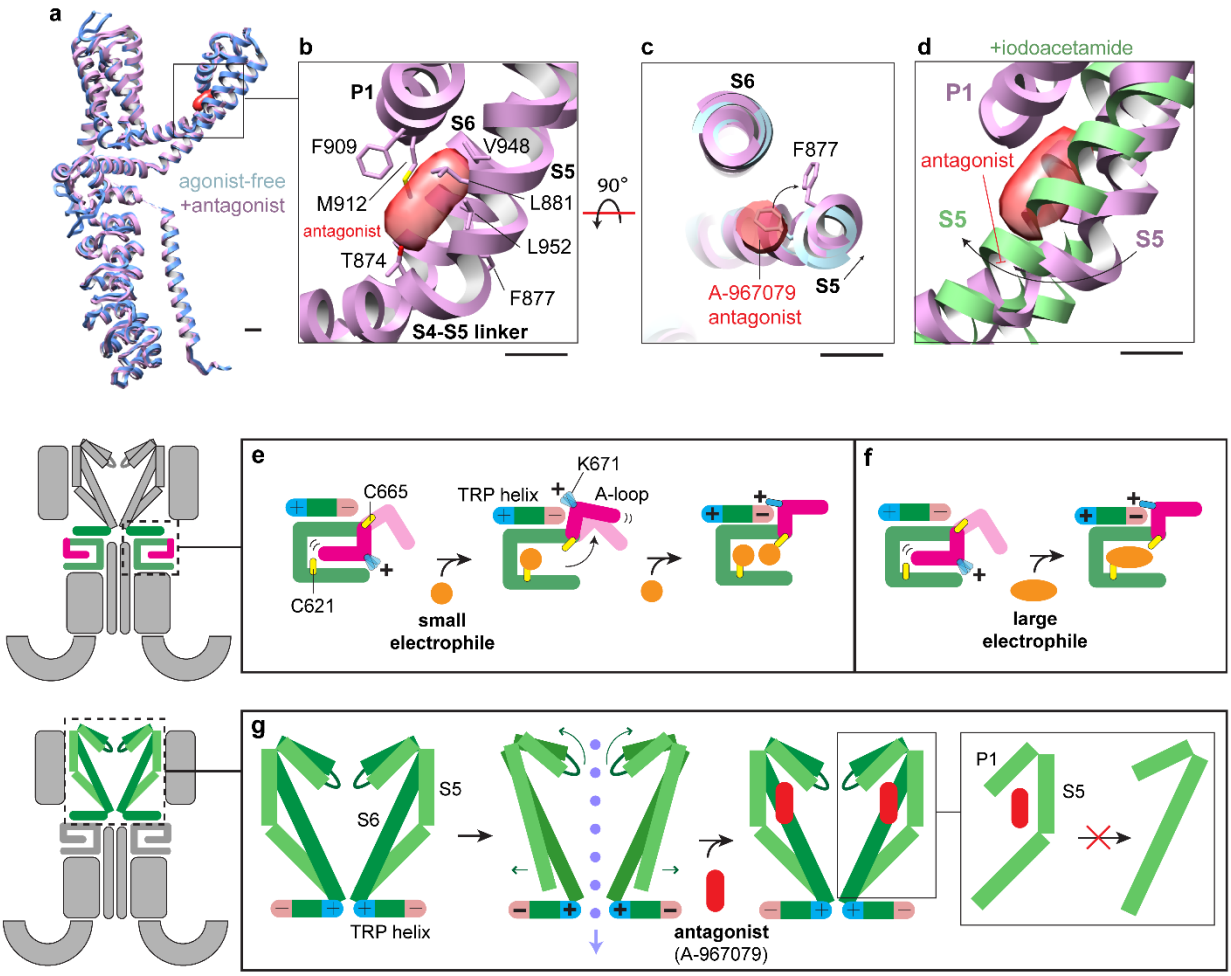


***Figure 3.13 Binding of A-967079 to TRPA1 and 2-step model of electrophile action.***

**(A)** The overall architecture of agonist-free and antagonist-bound TRPA1 is similar, representing a closed state.

**(B)** A-967079 binds at the elbow of S5, sandwiched between S6 and P1.

**(C)** Binding of A-967079 results in a slight shift in S5 and repositioning of F877.

**(D)** The antagonist is in an ideal position to block the straightening of the S5 elbow and inhibit channel gating.

**(E)** 2-step model of electrophile action on TRPA1. Attachment of a small electrophile to C621 results in A-loop rearrangement to the 'up' position, bringing C665 into the reactive pocket. Modification of C665 by a second small electrophile stabilizes the A-loop in the 'up' conformation and positions K671 at the C-terminus of the TRP helix, enhancing the electric dipole of this region.

**(F)** Attachment of a large electrophile to C621 is sufficient to stabilize the A-loop in the 'up' conformation and activate the channel.

**(G)** Increased positive electrostatic potential and charge repulsion at N-termini of adjacent TRP helices initiates conformational changes associated with dilation of the lower gate. These

movements are coupled to widening of the upper gate and selectivity filter through straightening of the S5 helix. The antagonist A-967079 binds to the bent elbow region of S5, inhibiting straightening of the α-helix required for channel gating.

**Table 3.1** Cryo-EM data collection, refinement and validation statistics.

| | TRPA1+BIA (LMNG) (EMD-21127) (PDB 6V9V) | TRPA1 agonist-free (LMNG) (EMD-21128) (PDB 6V9W) | TRPA1+IA (PMAL-C8) (EMD-21129) (PDB 6V9X) | TRPA1+A-96 (PMAL-C8) Class 1 (EMD-21130) (PDB 6V9Y) | TRPA1+A-96 (PMAL-C8) Class 2 (EMD-21131) |
|---|---|---|---|---|---|
| **Data collection and processing** | | | | | |
| Magnification | 22,500 | 75,000 | 31,000 | 31,000 | 31,000 |
| Voltage (kV) | 300 | 300 | 300 | 300 | 300 |
| Electron exposure (e–/Å$^2$) | 25 | 30 | 40 | 40 | 40 |
| Defocus range (μm) | 0.8-2.0 | 0.8-2.0 | 1.3-2.5 | 1.3-2.5 | 1.3-2.5 |
| Pixel size (Å) | 1.05 | 1.06 | 1.22 | 1.22 | 1.22 |
| Symmetry imposed | C4 | C4 | C4 | C4 | C4 |
| Initial particle images (no.) | 374,863 | 242,399 | 456,208 | 296,991 | 296,991 |
| Final particle images (no.) | 212,751 | 130,595 | 190,112 | 30,321 | 78,959 |
| Map resolution (Å) | 2.6 | 3.1 | 3.3 | 3.6 | 3.5 |
| FSC threshold | 0.143 | 0.143 | 0.143 | 0.143 | 0.143 |
| Map resolution range (Å) | 2.3-4.1 | 2.6-5.2 | 2.8-5.6 | 3.2-8.5 | 3.1-6.5 |
| | | | | | |
| **Refinement** | | | | | |
| Initial model used (PDB code) | 3J9P | 3J9P | 3J9P | 3J9P | |
| Model resolution (Å) | 2.8 | 3.4 | 3.4 | 3.8 | |
| FSC threshold | 0.5 | 0.5 | 0.5 | 0.5 | |
| Model resolution range (Å) | 357-2.8 | 360-3.4 | 311-3.4 | 311-3.8 | |
| Map sharpening *B* factor (Å$^2$) | -25 | -25 | -100 | -100 | |
| Model composition | | | | | |
| Non-hydrogen atoms | 18,976 | 18,812 | 18,084 | 17,716 | |
| Protein residues | 2,384 | 2,388 | 2,280 | 2,248 | |
| Ligands | 8 | 4 | 4 | 0 | |
| *B* factors (Å$^2$) | | | | | |
| Protein | 89 | 165 | 55 | 112 | |
| Ligand | 112 | 216 | 57 | 0 | |
| R.m.s. deviations | | | | | |
| Bond lengths (Å) | 0.008 | 0.008 | 0.004 | 0.009 | |
| Bond angles (°) | 0.904 | 0.965 | 0.880 | 1.179 | |
| Validation | | | | | |
| MolProbity score | 1.57 | 1.62 | 1.48 | 1.99 | |
| Clashscore | 3.47 | 4.53 | 3.52 | 6.53 | |
| Poor rotamers (%) | 1.2 | 1.21 | 1.24 | 2.13 | |
| Ramachandran plot | | | | | |
| Favored (%) | 94.6 | 95.26 | 96.07 | 94.38 | |
| Allowed (%) | 5.4 | 4.74 | 3.93 | 5.62 | |
| Disallowed (%) | 0.0 | 0.0 | 0.0 | 0.0 | |

| | TRPA1 class 1 (PMAL-C8) (EMD-21537) | TRPA1 class 2 (PMAL-C8) (EMD-21538) |
|---|---|---|
| **Data collection and processing** | | |
| Magnification | 31,000 | 31,000 |
| Voltage (kV) | 300 | 300 |
| Electron exposure (e–/Å$^2$) | 40 | 40 |
| Defocus range (μm) | 0.5-4.5 | 0.5-4.5 |
| Pixel size (Å) | 1.22 | 1.22 |
| Symmetry imposed | C4 | C4 |
| Initial particle images (no.) | 53,301 | 53,301 |
| Final particle images (no.) | 15,557 | 28,558 |
| Map resolution (Å) | 5.9 | 4.3 |
| FSC threshold | 0.143 | 0.143 |
| Map resolution range (Å) | 4.8-8.7 | 3.8-6.7 |

**Acknowledgements**

Some data for this study were collected at the Toronto High-Resolution High-Throughput cryo-EM facility, supported by the Canada Foundation for Innovation and Ontario Research Fund. This work was supported by an American Heart Association Postdoctoral Fellowship (J.Z.), a Banting Postdoctoral Fellowship from the Canadian Institutes of Health Research (J.Z.), an NSF Graduate Research Fellowship (No. 1650113 to J.V.L.K), a UCSF Chuan-Lyu Discovery Fellowship (J.V.L.K), a Helen Hay Whitney Foundation Postdoctoral Fellowship (C.E.P.) and grants from the NIH (R35 NS105038 to D.J; R01 GM098672, S10 OD021741, and S10 OD020054 to Y.C.; T32 HL007731 to C.E.P.; and T32 GM007449 to J.V.L.K). Y.C. is an Investigator of the Howard Hughes Medical Institute.

**References**

Afonine, P. V. *et al.* Real-space refinement in PHENIX for cryo-EM and crystallography. *Acta Crystallographica Section D* **74**, 531-544 (2018).

Anandakrishnan, R., Aguilar, B. & Onufriev, A. V. H++ 3.0: automating pK prediction and the preparation of biomolecular structures for atomistic molecular modeling and simulations. *Nucleic acids research* **40**, W537-W541 (2012).

Asarnow, D., Palovcak, E., and Cheng, Y. UCSF pyem v0.5. doi:10.5281/zenodo.3576630 (2019).

Autzen, H. E. *et al.* Structure of the human TRPM4 ion channel in a lipid nanodisc. *Science* **359**, 228-232 (2018).

Bahia, P. K. *et al.* The exceptionally high reactivity of Cys 621 is critical for electrophilic activation of the sensory nerve ion channel TRPA1. *J Gen Physiol* **147**, 451-465 (2016).

Baker, N. A., Sept, D., Joseph, S., Holst, M. J. & McCammon, J. A. Electrostatics of nanosystems: application to microtubules and the ribosome. *Proc Natl Acad Sci U S A* **98**, 10037-10041 (2001).

Bandell, M. *et al.* Noxious cold ion channel TRPA1 is activated by pungent compounds and bradykinin. *Neuron* **41**, 849-857 (2004).

Bautista, D. M., Pellegrino, M. & Tsunozaki, M. TRPA1: A gatekeeper for inflammation. *Annu Rev Physiol* **75**, 181-200 (2013).

Bobkov, Y. V., Corey, E. A. & Ache, B. W. The pore properties of human nociceptor channel TRPA1 evaluated in single channel recordings. *Biochim Biophys Acta* **1808**, 1120-1128 (2011).

Cao, E., Liao, M., Cheng, Y. & Julius, D. TRPV1 structures in distinct conformations reveal activation mechanisms. *Nature* **504**, 113-118 (2013).

Chen, J. & Hackos, D. H. TRPA1 as a drug target--promise and challenges. *Naunyn Schmiedebergs Arch Pharmacol* **388**, 451-463, doi:10.1007/s00210-015-1088-3 (2015).

Christensen, A. P., Akyuz, N. & Corey, D. P. The Outer Pore and Selectivity Filter of TRPA1. *PLoS One* **11**, e0166167 (2016).

Chuang, H.-h., Neuhausser, W. M. & Julius, D. The Super-Cooling Agent Icilin Reveals a Mechanism of Coincidence Detection by a Temperature-Sensitive TRP Channel. *Neuron* **43**, 859-869 (2004)

Cordero-Morales, J. F., Gracheva, E. O. & Julius, D. Cytoplasmic ankyrin repeats of transient receptor potential A1 (TRPA1) dictate sensitivity to thermal and chemical stimuli. *Proceedings of the National Academy of Sciences of the United States of America* **108**, E1184-E1191 (2011).

Dai, Y. *et al.* Sensitization of TRPA1 by PAR2 contributes to the sensation of inflammatory pain. *J Clin Invest* **117**, 1979-1987 (2007).

Dang, S. *et al.* Cryo-EM structures of the TMEM16A calcium-activated chloride channel. *Nature* **552**, 426-429 (2017).

Diver, M. M., Cheng, Y. & Julius, D. Structural insights into TRPM8 inhibition and desensitization. *Science* **365**, 1434-1440 (2019).

Doyle, D. A. *et al.* The structure of the potassium channel: molecular basis of K+ conduction and selectivity. *Science* **280**, 69-77 (1998).

Emsley, P., Lohkamp, B., Scott, W. G. & Cowtan, K. Features and development of Coot. *Acta Crystallographica Section D* **66**, 486-501 (2010).

Gracheva, E. O. *et al.* Molecular basis of infrared detection by snakes. *Nature* **464**, 1006-1011 (2010).

Grant, T., Rohou, A. & Grigorieff, N. cisTEM, user-friendly software for single-particle image processing. *eLife* **7**, e35383 (2018).

Hasan, R., Leeson-Payne, A. T. S., Jaggar, J. H. & Zhang, X. Calmodulin is responsible for Ca2+-dependent regulation of TRPA1 Channels. *Scientific Reports* **7**, 45098 (2017).

Hasselbalch, K. A. Die Berechnung der Wasserstoffzahl des Blutes aus der freien und gebundenen Kohlensäure desselben, und die Sauerstoffbindung des Blutes als Funktion der Wasserstoffzahl. *Biochemische Zeitschrift* **78**, 112-114 (1917).

Henderson, L. J. Concerning the relationship between the strength of acids and their capacity to preserve neutrality. *Am. J. Physiol.* **21**, 173-179 (1908).

Hilton, J. K., Kim, M. & Van Horn, W. D. Structural and Evolutionary Insights Point to Allosteric Regulation of TRP Ion Channels. *Acc Chem Res* **52**, 1643-1652, doi:10.1021/acs.accounts.9b00075 (2019).

Hinman, A., Chuang, H. H., Bautista, D. M. & Julius, D. TRP channel activation by reversible covalent modification. *Proc Natl Acad Sci U S A* **103**, 19564-19568 (2006).

Huang, Y., Winkler, P. A., Sun, W., Lü, W. & Du, J. Architecture of the TRPM2 channel and its activation mechanism by ADP-ribose and calcium. *Nature* **562**, 145-149 (2018).

Karashima, Y. *et al.* Agonist-induced changes in Ca(2+) permeation through the nociceptor cation channel TRPA1. *Biophys J* **98**, 773-783 (2010).

Lin King, J. V. *et al.* A Cell-Penetrating Scorpion Toxin Enables Mode-Specific Modulation of TRPA1 and Pain. *Cell* **178**, 1362-1374.e1316 (2019).

Macpherson, L. J. *et al.* Noxious compounds activate TRPA1 ion channels through covalent modification of cysteines. *Nature* **445**, 541-545 (2007).

Meents, J. E., Fischer, M. J. M. & McNaughton, P. A. Sensitization of TRPA1 by Protein Kinase A. *PLOS ONE* **12**, e0170097 (2017).

Moriarty, N. W., Grosse-Kunstleve, R. W. & Adams, P. D. electronic Ligand Builder and Optimization Workbench (eLBOW): a tool for ligand coordinate and restraint generation. *Acta Crystallographica Section D* **65**, 1074-1080 (2009).

Jordt, S. E. *et al.* Mustard oils and cannabinoids excite sensory nerve fibres through the TRP channel ANKTM1. *Nature* **427**, 260-265 (2004).

Paulsen, C. E., Armache, J. P., Gao, Y., Cheng, Y. & Julius, D. Structure of the TRPA1 ion channel suggests regulatory mechanisms. *Nature* **520**, 511-517 (2015).

Pettersen, E. F. *et al.* UCSF Chimera—A visualization system for exploratory research and analysis. *Journal of Computational Chemistry* **25**, 1605-1612 (2004).

Punjani, A., Rubinstein, J. L., Fleet, D. J. & Brubaker, M. A. cryoSPARC: algorithms for rapid unsupervised cryo-EM structure determination. *Nature Methods* **14**, 290-296 (2017).

Sakmann, B. & Neher, E. *Single-channel recording*. (Springer, 2009).

Sura, L. *et al.* C-terminal acidic cluster is involved in Ca2+-induced regulation of human transient receptor potential ankyrin 1 channel. *J Biol Chem* **287**, 18067-18077 (2012).

Suo, Y. *et al.* Structural Insights into Electrophile Irritant Sensing by the Human TRPA1 Channel. *Neuron* **105**, 882-894.e885 (2020).

Talavera, K. *et al.* Mammalian Transient Receptor Potential TRPA1 Channels: From Structure to Disease. *Physiol Rev* **100**, 725-803 (2020).

Wang, Y. Y., Chang, R. B., Waters, H. N., McKemy, D. D. & Liman, E. R. The nociceptor ion channel TRPA1 is potentiated and inactivated by permeating calcium ions. *J Biol Chem* **283**, 32691-32703 (2008).

Wilson, S. R. *et al.* The epithelial cell-derived atopic dermatitis cytokine TSLP activates neurons to induce itch. *Cell* **155**, 285-295 (2013).

Wang, X., Kirberger, M., Qiu, F., Chen, G. & Yang, J. J. Towards predicting Ca2+-binding sites with different coordination numbers in proteins with atomic resolution. *Proteins* **75**, 787-798 (2009).

Yin, Y. *et al.* Structural basis of cooling agent and lipid sensing by the cold-activated TRPM8 channel. *Science* **363**, doi:10.1126/science.aav9334 (2019).

Zimova, L. *et al.* Intracellular cavity of sensor domain controls allosteric gating of TRPA1 channel. *Sci Signal* **11** (2018).

Zurborg, S., Yurgionas, B., Jira, J. A., Caspani, O. & Heppenstall, P. A. Direct activation of the ion channel TRPA1 by Ca2+. *Nat Neurosci* **10**, 277-279 (2007).

Zhang, K. Gctf: Real-time CTF determination and correction. *Journal of Structural Biology* **193**, 1-12 (2016).

Zhang, Z., Tóth, B., Szollosi, A., Chen, J. & Csanády, L. Structure of a TRPM2 channel in complex with Ca2+ explains unique gating regulation. *eLife* **7**, e36409 (2018).

Zheng, S. Q. *et al.* MotionCor2: anisotropic correction of beam-induced motion for improved cryo-electron microscopy. *Nature Methods* **14**, 331-332 (2017).

Zivanov, J. *et al.* New tools for automated high-resolution cryo-EM structure determination in RELION-3. *eLife* **7**, e42166 (2018)

**Publishing Agreement**

It is the policy of the University to encourage open access and broad distribution of all theses, dissertations, and manuscripts. The Graduate Division will facilitate the distribution of UCSF theses, dissertations, and manuscripts to the UCSF Library for open access and distribution. UCSF will make such theses, dissertations, and manuscripts accessible to the public and will take reasonable steps to preserve these works in perpetuity.

I hereby grant the non-exclusive, perpetual right to The Regents of the University of California to reproduce, publicly display, distribute, preserve, and publish copies of my thesis, dissertation, or manuscript in any form or media, now existing or later derived, including access online for teaching, research, and public service purposes.

DocuSigned by:
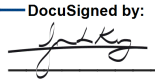
462BB3B36FCB411...

Author Signature

8/19/2020

Date